Electron dynamics in the spin-split surface states of semiconductors with strong spin-orbit interaction

Dissertation

zur Erlangung des Grades eines Doktors der Naturwissenschaften

am Fachbereich Physik der Freien Universität Berlin

vorgelegt von
Anna Sophia Ketterl

Berlin 2019

Abstract

This thesis investigates the excitation and dynamics of charge carriers in two narrow-gap semiconductors featuring spin-polarized surface states, which are promising candidates for spintronic applications. On the topological insulator Bi_2Se_3, we investigated the origin of helicity-dependent photocurrents by two-photon photoemission. On BiTeI, we studied the electron- and hole-dynamics in the surface state and the conduction band minimum (CBM), which both feature a giant Rashba-splitting, with time- and angle-resolved photoemission spectroscopy.

In the case of Bi_2Se_3, circular polarized pulses of $1.7\,eV$ photon energy are used to excite electrons resonantly from the occupied topological surface state (TSS) to the unoccupied TSS. The excited electrons are photoemitted with s-polarized pulses of $4.7\,eV$, conserving the momentum distribution. The dichroic contrast created during the excitation is identified to be predominantly governed by the interaction of the light with the initial state, as corroborated by off-resonantly excited spectra, model calculations performed by our collaboration partners, and time-resolved data. Anti-symmetric patterns, as expected from the commonly assumed coupling of the photon angular momentum to the parallel component of the electron spin, can only be observed for electrons stemming from the CBM, but not from the TSS. The TSS, in contrast, shows clear three-fold symmetric patterns. Residual asymmetries, probably originating from experimental inaccuracies, are large enough to explain the helicity-dependent photocurrents observed in previous transport measurements.

On BiTeI, the electronic system is probed with $6.2\,eV$ photon energy, giving access to the carriers around the Fermi level E_F. We confirm the reported electronic structure of the Te-terminated surface and find only minor influences on the electronic structure by the dopants manganese and vanadium. We observe a complex interplay of surface and bulk dynamics after photoexcitation with pulses of $1.5\,eV$ photon energy. Electron-electron scattering is found to be effective across all subsystems. The dynamics above E_F are governed by bulk interactions. Heat is dissipated from the hot electron gas by electron-phonon coupling. The long thermalization times between electrons and lattice suggest a phonon bottleneck, created by long lifetimes of optical phonons. The dynamics below E_F at binding energies up to $50\,meV$ are sped up by drift currents induced by the positively charged surface. Within the Rashba-split surface state (RSS), we find a temperature-dependent coupling of the photoholes to the surface plasmon. Furthermore, we refute previous reports of ballistic spin-dependent transport upon excitation with circular polarized pump pulses.

Deutsche Kurzfassung

Diese Arbeit beschäftigt sich mit der elektronischen Anregung und deren Dynamik in zwei Halbleitern mit schmaler Bandlücke. Beide Systeme weisen spinaufgespaltene Oberflächenzustände auf und gelten deswegen als vielversprechende Materialien in der Spintronik. Der Ursprung von Photoströmen im topologischen Isolator Bi_2Se_3, die von der Helizität des anregenden Lichts abhängen, wird mit Zwei-Photonen-Photoemission ergründet. Ferner wird die Elektronen- und Lochdynamik des Rashba-aufgespaltenen Oberflächenzustands (RSS) und Leitungsbandminimums (CBM) von BiTeI mit zeit- und winkelaufgelöster Photoelektronenspektroskopie untersucht.

Zur resoananten Anregung des besetzten topologischen Oberflächenzustands (TSS) in den unbesetzten TSS von Bi_2Se_3 werden zirkular polarisierte Laserpulse mit 1.7 eV Photonenenergie verwendet. Die angeregten Elektronen werden mit s-polarisiertem Licht mit 4.7 eV Photonenenergie photoemittiert, wobei die Winkelverteilung unverändert bleibt. Der Zirkulardichroismus, der durch die Anregung erzeugt wird, kann auf die Wechselwirkung zwischen dem anregenden Licht und dem Anfangszustand zurückgeführt werden, wie durch nicht-resonante und zeitaufgelöste Messungen sowie Modellrechnungen unserer Kollaborationspartner bestätigt wird. Anti-symmetrische Anregungsmuster, wie sie die üblicherweise angenommene Kopplung zwischen Drehimpuls des Lichts und parallelem Elektronenspin erzeugen würde, können nur am CBM beobachtet werden. Der TSS weist hingegen dreifach rotationssymmetrische Anregungsmuster auf. Asymmetrische Komponenten der Spektren, die auf geringe experimentelle Fehler zurückgeführt werden, sind groß genug um die in anderen Gruppen beobachteten Photoströme zu erklären.

Die elektronische Struktur von BiTeI wird mit direkter Photoemission mit 6.2 eV Photonenenergie untersucht. Die Ergebnisse zur elektronischen Struktur bestätigen die Beobachtungen anderer Arbeitsgruppen. Dotierung der Kristallstruktur mit Mangan und Vanadium beeinflusst die elektronische Struktur nur marginal. Die Elektronendynamik, angeregt mit 1.5 eV Photonenenergie, zeigt ein komplexes Zusammenspiel von Oberflächen- und Volumenrelaxationsprozessen, die durch Elektron-Elektron-Streuung miteinander verknüpft werden. Über dem Fermi-Niveau wird die Dynamik durch die Elektron-Phonon-Streuung in den Volumenbändern bestimmt. Das langsame Abkühlen der heißen Elektronen lässt auf hohe Lebensdauern der involvierten optischen Phononen schließen. Die Dynamik unterhalb des Ferminiveaus bis zu einer Bindungsenergie von 50 meV wird durch Driftströme beschleunigt, die durch die partielle positive Ladung der Oberfläche erzeugt werden. Bei höheren Bindungsenergien wird die Dynamik von der temperaturabhängigen Kopplung des RSS an das Oberflächenplasmon bestimmt. Außerdem konnten frühere Berichte von spinabhängigen Transportphänomenen nicht bestätigt werden.

Contents

Chapter 1

Introduction

Ever since their invention, computers have continuously become smaller and have improved their performance. So much so, as to inspire considerations like Moore's law from 1965, which states that the number of transistors on a computer chip doubles roughly every two years [116]. A similar, but less popular observation is Koomey's law: Since the 1950s, the power dissipated per computation halves in less than two years [94].
Even though it seems implausible to sustain such an exponential growth over a significant amount of time, both laws have held up well until recently. However, Moore and Koomey themselves predicted a breakdown to this development in the early 2010s [32, 93].

So far, the incessant increase in computer performance and the proceeding miniaturization of electronics has been driven by continuous development of materials, concepts and techniques. The invention of the integrated circuit, flash memory, metal-oxide-semiconductor field-effect transistors (MOSFETs) and excimer laser lithography are just a few examples.

And even though we seem to be at a threshold, where the progress comes to a halt, lots of different ideas to further improve the performance of computers have been proposed. Some aim at the improvement of miniaturization, durability, and/or speed of magnetic memory, as *e.g.* the ideas of heat-assisted magnetic recording [57], race-track memory [67], and all-optical switching [146]. The field of quantum computing, meanwhile, tries to revolutionize the computing step itself by exploiting entanglement and superposition of quantum states [120].

Another idea for the improvement of data storage and transfer are the so-called spintronics. The basic concept here is to harness the spin degree of freedom of the electron. Spintronics can be divided into two general branches: One is related to spin-dependent transport in mostly magnetic metals, inspired by observations like the discovery of the giant magnetoresistance [9, 20]. The other focuses on semiconductors and was mainly inspired by the proposal of the spin field-effect transistor (spin-FET) [36].
The spin-FET exploits spin-orbit interactions (SOIs) to manipulate the spin of electrons passing through a quasi-2D electronic system in a semiconductor heterostructure. The idea for this concept stems from the description of the Rashba effect [28].

In general, the description of the effects of SOIs on the band structure (BS) of solids has started with Elliot and Dresselhaus in 1954 [38, 45]. Dresselhaus' description of the

spin-orbit splitting (SOS) in semiconductors with zincblende crystal structure is now known as Dresselhaus effect [19]. Rashba later described the effect in semiconductors with wurtzite structure [150].
Both zincblende and wurtzite structures distinguish themselves from many other crystal structures because they are not inversion-symmetric. In fact, this is a necessary requirement for spin-splitting induced by SOI if time-reversal symmetry is conserved.

In the following years, Rashba and others continued exploring the influence of SOI on the crystal structure [147] in theoretical works. However, experimental verification of these ideas came sparsely and significantly later [148].
It was not until the 1980s, that the field gained a new boost with the observation of spin-splitting in quasi-2D systems [171, 172], which were analogously described to the bulk of inversion-asymmetric semiconductors [28, 29].

While the bulk spin-splitting of inversion-asymmetric semiconductors is an intrinsic property, the spin-splitting in quasi-2D systems can be manipulated by applying external electric fields [19]. This is the underlying working principle of the already mentioned spin-FET [36].

The field of SOI in 2D electron gases gained new impulses, when in the 1990s, Rashba splitting was observed in the surface states of noble metals. While the bulk crystal structure of most noble metals is inversion-symmetric, this symmetry is always broken at the surface, allowing for a spin-splitting by SOI of states with surface character. As spin-orbit coupling (SOC) scales with the atomic mass, noble metals are likely candidates to feature this effect. The first Rashba type spin-splitting observed by angle-resolved photoemission spectroscopy (ARPES) was in the Shockley surface state on Au(111) [105]. Since then, Rashba splitting has been observed on many noble metal surfaces and also different 2D electronic systems like metal-semiconductor heterostructures [19].

In the early 2010s, the interest shifted back to inversion-asymmetric semiconductors with the discovery of the family BiTeX, where X is a halogen [48]. These materials are layered crystals without inversion symmetry, with a stacking sequence Te-Bi-X. All of these compounds exhibit strong spin-orbit interaction and a narrow band gap where valence band (VB) and conduction band (CB) have the same symmetry character. This leads to extremely large bulk Rashba splitting, which made it for the first time resolvable in ARPES and spin-resolved ARPES [78].
In addition to the spin-split bulk bands, the BiTeX family possesses spin-split surface states that derive either from the CB or VB and respectively live on the Te- or X-terminated surface.
In 2014, Ogawa *et al.* claimed, that they were able to excite spin-polarized currents in these materials via the excitation of BiTeBr by circularly polarized light [130], which would open a new pathway to exploit Rashba materials for spintronics.

In parallel to the latter developments on Rashba materials, a second field emerged, which is concerned with a different kind of semiconductor that feature spin-split surface states: so-called topological insulators (TIs) [13, 64]. These materials feature strong

SOI that leads to an inversion of the bands around the primary band gap. This makes the BS of TIs distinctively different from "trivial" insulators. A topologically trivial insulator is an insulator or semiconductor with a BS, that can be smoothly transformed into the limit of an atomic insulator. The topologically non-trivial phase can be found both on 2D and 3D materials. Interfacing a trivial with a non-trivial insulator will lead to the emergence of topological surface states (TSSs) in the form of surface or edge states, depending on the dimensionality of the TI.

The TSS of a TI distinguishes itself by being both spin-polarized and often having a linear or quasi-linear dispersion. This makes it especially interesting for spintronics, as it therefore does not only carry spin-polarized currents, it also features ballistic transport with highly suppressed backscattering. For this reason, TIs have been discussed as possible materials for spintronics ever since their discovery. However, the excitation of currents purely in the TSSs on 3D TIs is challenging, as they are typically so strongly intrinsically doped, that the Fermi level is shifted into either the VB or CB, just like in BiTeI [74, 78].

One of the most prominent representatives of 3D TIs is Bi_2Se_3. Bi_2Se_3 belongs to the so-called second generation 3D TIs, which have been discovered shortly after the first 3D TI, Bi_xSb_{1-x}. The second generation 3D TIs are easily the most studied 3D TIs, Bi_2Se_3 in particular. This should not come as a surprise, as Bi_2Se_3 lends itself to studies, especially with photoemission spectroscopy (PES): It possesses a comparably large band gap of $0.3\,eV$, featuring a single TSS with linear dispersion (therefore also referred to as Dirac cone (DC)), weak hexagonal warping and the Dirac point (DP) laying within the gap at the $\bar{\Gamma}$ point. Furthermore, it is intrinsically n-doped, with a Fermi level shifted into the conduction band minimum (CBM). Therefore, the TSS is occupied. In addition, Bi_2Se_3 possesses a second, unoccupied TSS [125, 126].
Ever since currents excited by circularly polarized light on Bi_2Se_3 have been reported for the first time [112], the origin of these currents has been disputed [25, 80, 83, 132, 133, 139–141]. The most popular explanation is a coupling of the photon's angular momentum to the electron spin, predominantly exciting one branch of the DC. This would indeed mean, that the photocurrent is — at least initially — carried by the electrons from the occupied TSS and should therefore be spin-polarized. This, however, was so far not proven with absolute certainty.

Recently, the fields of direct spin-orbit effects and topological matter have been connected by the discovery of spin-polarized surface states with linear dispersion on W(110) [103, 114, 115]. While tungsten is not a TI, not even a semiconductor, it features surface states influenced by SOI, that are strongly reminiscent of the DCs of TIs.

In this thesis, I want to provide further insight into whether spin-polarized photocurrents can be excited on Bi_2Se_3 or BiTeI. For this aim, we[1] study both materials with two-

---

[1]my master students, supervisors, collaboration partners, namely B. Andres, M. Bastian, J. Braun, H. Ebert, Th. Fauster, C. Gahl, K. A. Kokh, J. Minár, S. Otto, M. Polverigiani, A. Shikin, O. E. Thereshchenko, V. Voroshnin, M. Weinelt, and I

photon photoemission (2PPE) and time- and angle-resolved photoemission spectroscopy (tr-ARPES) respectively. These methods, which are closely related, allow for the study of the dynamics of the electrons in the BS before, during and after photoexcitation.

In the case of Bi_2Se_3, we are mainly interested in the distribution of excited carriers during and after photoexcitation with circularly polarized light, in order to provide insight towards the origin of the photocurrents observed in transport measurements [83, 112, 133]. In the case of BiTeI, we limit ourselves to the study of the electron-like Rashba-split surface state (RSS) and the CBM on the Te-terminated surface. We excite the sample with near-infrared (nIR) laser pulses and study the relaxation of the carriers.

In Chapter 2, I will give a more detailed introduction to SOI and its effect on the BS of solids. I will introduce both the considerations behind the Rashba effect and the concept of TIs in more detail as well as how they emerge from SOI.

In Chapter 3, I will introduce the concept of 2PPE and tr-ARPES. This chapter outlines both the underlying physical principles as well as introduces the experimental setup used for the measurements presented in this thesis. Furthermore, I will outline the process of sample preparation and give a short insight to the theoretical considerations related to the analysis of our data.

In Chapter 4, our results on Bi_2Se_3 are presented. We excited the sample with circularly polarized light in the visible and nIR range and studied the distribution of the excited electrons in the second TSS by 2PPE. We made sure that the probing step and the final states do not influence those patterns, so that we can actually observe the excitation process. This requires the right polarization and energy of the probe pulses. The influence of different polarizations and excitation geometries is presented.
We find, that the observed excitation patterns are indeed dominated by the coupling of the incident photons to the initial states and hardly depend on the intermediate state. This is supported by altering the excitation energy, by comparison of our data to direct photoemission calculations, and by time-resolved measurements.
However, the asymmetric excitation patterns expected from the generally assumed coupling mechanism only emerge very close to the Fermi level, but not in the band gap of Bi_2Se_3. The generally assumed coupling of the light's angular momentum to the electron spin must therefore be rejected. We observe residual asymmetries in our data, possibly stemming from experimental inaccuracies or, alternatively, a so far not understood process taking place only at the Fermi level. This effect is large enough to account for the photocurrents observed in transport measurements [112].

In Chapter 5, I present our results on BiTeI. We studied the dynamics of the electronic states close to the Fermi level on the Te-terminated surface with tr-ARPES. In line with previous reports, we observe that aging of the sample under relatively high pressures of $3 - 4 \cdot 10^{-9}$mbar mainly affects the I-terminated surface [34, 50]. Furthermore, we find considerable asymmetries between the dynamics of electrons and holes on the surface.

From the fluence and temperature dependence of the dynamics, we can discern the origins of this asymmetry: The electron dynamics is mostly governed by electron-phonon interactions, while the hole dynamics is influenced by the surface band bending and the coupling to a surface plasmon at low temperatures.

Furthermore, we study the influence of the dopants manganese and vanadium on the electronic structure and electron dynamics. We find, that both lead to a clearer discernability of the RSS in the photoemission spectra while only slightly influencing the dispersions of the bands. Furthermore, Mn does only slightly influence the electron dynamics, mainly by increasing the electron lifetimes close to the Fermi level. V effectively suppresses the thermalization of the excited carriers, possibly by constantly redistributing energy via defect-scattering. Furthermore, we see a persistence of the surface plasmon even at room temperature.

In Chapter 6 I will provide a short summary and conclusion of our results.

Chapter 2

Spin-orbit Interaction, Rashba States and Dirac Cones

The focus of this thesis is to investigate the electron dynamics in the surface states of two different layered crystals, Bi_2Se_3 and BiTeI. Both materials feature spin-polarized surface states, which are both of fundamental interest and possibly interesting for application in spintronics [36, 64, 173]. To be more precise, BiTeI features Rashba-split surface states (RSSs), while Bi_2Se_3 possesses topological surface states (TSSs) or Dirac cones (DCs). These surface states arise partially directly, partially indirectly from spin-orbit interaction (SOI).

This chapter will introduce the basic concepts that lead to the emergence of the aforementioned surface states: First, we will briefly discuss the theory behind spin-orbit coupling (SOC) in general (Sec. 2.1), before turning to the Rashba effect (Sec. 2.2), which is a direct consequence of SOI in a solid, and then to topological insulators (Sec. 2.3), a phase of matter which is more indirectly related to SOI.

2.1 Fundamentals of Spin-Orbit Coupling

When a charged particle moves in an electric field, this field takes the shape of a magnetic field in the rest frame of the charged particle.
This is particularly true for an electron moving in an atomic potential. In this case, the electron's spin will interact with the magnetic field perceived from the angular momentum. This is called spin-orbit coupling. While SOC can be manually introduced into the Hamiltonian describing a bound electron, it will naturally emerge from the relativistic Dirac description. In the following, I will in turn introduce both considerations.

2.1.1 SOC from a Semi-Classical Approach

Classically, we know that a particle with charge q moving with a speed $\mathbf{v}$ in a magnetic field $\mathbf{B}$ will experience a force, the Lorentz force, $\mathbf{F}_{Lor}$ that can be written as an effective electric field $\mathbf{E}_{\mathrm{Eff}}$:

$$\mathbf{F}_{\mathrm{Lor}} = q\,(\mathbf{v} \times \mathbf{B}) = q\mathbf{E}_{\mathrm{Eff}} \ . \tag{2.1}$$

Vice versa, a charge moving in an electric field will generate an effective magnetic field [68]:

$$\mathbf{B}_{Eff} = \frac{1}{c^2} \left(\mathbf{v} \times \mathbf{E} \right) \ , \tag{2.2}$$

c being the speed of light.

As we have already established, this is also true for an electron, moving in the central potential $V(r)$ of an atomic core. Its magnetic moment $\mu_{\mathbf{s}}$ will then couple to this effective magnetic field, yielding the following Hamiltonian for SOC, $\hat{H}_{SO}$:

$$\hat{H}_{\mathrm{SO}} = -\mu_{\mathbf{s}} \cdot \hat{\mathbf{B}}_{\mathrm{Eff}} \ . \tag{2.3}$$

We will now try to formulate this Hamiltonian in terms of the electron's quantum numbers s and l, or, more precisely, in terms of the corresponding operators.
First, we reformulate the electric field in terms of the atomic potential:

$$\mathbf{E} = \frac{1}{\varepsilon_0} \frac{\mathrm{d}V(r)}{\mathrm{d}r} \frac{\mathbf{r}}{r} \ . \tag{2.4}$$

If we insert this into Eq. 2.2, identify $\mathbf{v} \times \mathbf{r} = -\frac{1}{m_e}\mathbf{L}$ and write in terms of quantummechanical operators, we get

$$\hat{\mathbf{B}}_{\mathrm{Eff}} = -\frac{1}{c^2 \varepsilon_0 m_e} \frac{\mathrm{d}V(r)}{\mathrm{d}r} \frac{1}{r} \hat{\mathbf{L}} \ . \tag{2.5}$$

Furthermore, the magnetic moment created by the spin is given by

$$\mu_{\mathbf{s}} = \frac{g_s \varepsilon_0}{2m_e} \hat{\mathbf{S}} \ . \tag{2.6}$$

If we insert Eq. 2.5 and Eq. 2.6 into Eq. 2.3, approximate $g_s \cong 2$ and assume a hydrogen-like potential $V(r) = -Ze/r$, Z being the charge of the nucleus, we arrive at the Hamiltonian for SOC:

$$\hat{H}_{\mathrm{SO}} = \frac{Ze^2}{2m^2 c^2 r^3} \left(\hat{\mathbf{S}} \cdot \hat{\mathbf{L}} \right) \ . \tag{2.7}$$

Notice, that we introduced an additional factor $\frac{1}{2}$, the so called Thomas-Factor, which emerges in the back-transformation to the core's rest-frame. Phenomenologically, it arises from the precession of the electron spin. We will see in the next section, that it arises naturally from a relativistic treatment of the problem.

The introduction of $\hat{H}_{SO}$ into the total Hamiltonian of a bound electron influences the energy of the electronic states, *i.e.* it will introduce a spin-orbit splitting (SOS) of degenerate states depending on their respective coupling between $\mathbf{l}$ and $\mathbf{s}$, which are the orbital and spin moments of an individual electron. It also means, the z-components of $\mathbf{l}$ and $\mathbf{s}$ are no longer conserved, *i.e.* no longer good quantum numbers. Instead, we have to introduce a total angluar momentum $\mathbf{j}$:

$$\mathbf{j} = \mathbf{l} + \mathbf{s} \ . \tag{2.8}$$

The quantum numbers j, s, m_j replace l, m_l, m_s as good quantum numbers.

Depending on the strength of SOI in the material, the total angular momentum of an atom is either formed by first adding up the spin $\mathbf{S} = \sum_i \mathbf{s}_i$ and angular momenta $\mathbf{L} = \sum_i \mathbf{l}_i$ of the individual electrons before coupling them to a total angular momentum

$$\mathbf{J} = \mathbf{L} + \mathbf{S} \ , \tag{2.9}$$

which is referred to as LS coupling. Or, for strong SOI in the atom, generally for atoms with $Z > 30$, we get so called jj coupling:

$$\mathbf{J} = \sum_i \mathbf{j}_i = \sum_i \left(\mathbf{l}_i + \mathbf{s}_i \right) \ , \tag{2.10}$$

where $\mathbf{l}$ and $\mathbf{s}$ of each electron are first coupled to each other and then added to a total angular momentum. The crystals studied in this thesis are comprised entirely out of elements which show jj coupling.

2.1.2 SOC from Relativistic Quantum Mechanics

A more direct but less intuitive way to derive the term in 2.7, is from relativistic quantum mechanics. As we will see in this section, SOC can be directly derived from the Dirac Hamiltonian of a particle with charge e and mass m moving in an electric field. The full derivation can be found, *e.g.*, in the fourth volume of the *Course in Theoretical Physics* by Landau and Lifshits [12, Ch. 3 and 4], which served as a guideline for this section.

In the Dirac formalism, the classical quantummechanical vectors are replaced by corresponding 4-vectors. In case of fermions with spin $\frac{1}{2}$, these vectors are expressed in terms of two-component spinors, the components corresponding to the eigenvalues of the spin's z-component.

The Dirac equation corresponding to a charged particle moving in an electric field, analogously to classic quantum mechanics, is written as

$$\left[\gamma \left(p - eA \right) - m \right] \psi = 0 \ , \tag{2.11}$$

where γ^μ are the so-called Dirac matrices, p is the 4-momentum, $A = (\Phi, \mathbf{A})$ is the relativistic 4-potential, consisting of the classical scalar and vector potential, respectively Φ and $\mathbf{A}$, and ψ is a bispinor.

It is possible to transform this equation into the shape of the time-dependent Schrödinger equation with a Hamiltonian

$$\hat{H}_A = \boldsymbol{\alpha} \cdot (\mathbf{p} - e\mathbf{A}) + \beta m + e\Phi \ , \tag{2.12}$$

where $\boldsymbol{\alpha} = \gamma^0 \boldsymbol{\gamma}$ and $\beta = \gamma^0$. Or, in terms of the Pauli matrices σ:

$$\boldsymbol{\alpha} = \begin{pmatrix} 0 & \boldsymbol{\sigma} \\ \boldsymbol{\sigma} & 0 \end{pmatrix} \ , \quad \beta = \begin{pmatrix} 1 & 0 \\ 0 & -1 \end{pmatrix} \tag{2.13}$$

in the standard representation, *i.e.* when ψ is expressed as the linear combinations ϕ and χ of the original spinors ξ and η:

$$\phi = \frac{1}{\sqrt{2}}(\xi + \eta), \quad \chi = \frac{1}{\sqrt{2}}(\xi - \eta) \ . \tag{2.14}$$

This representation has the advantage, that in the non-relativistic limit, χ vanishes.

For small velocities, we can obtain an approximate Schrödinger equation involving only ϕ, via the expansion of the wave function in powers of $1/c$ [12, §33]. The first order expansion yields the following equation:

$$i\hbar\frac{\partial\phi}{\partial t} = H\phi = \left[\frac{1}{2m}\left(\mathbf{p} - \frac{e}{c}\mathbf{A}\right)^2 + e\Phi - \frac{e}{2mc}\boldsymbol{\sigma}\cdot\mathbf{H}\right] \ , \tag{2.15}$$

where $\mathbf{H}$ is the curl of $\mathbf{A}$, in other words the magnetic field. This last term is also the only difference to the non-relativistic Schrödinger equation and has the form of a magnetic dipole - the spin - in a magnetic field.

Including the second order, $1/c^2$, and regarding only an electric field $E = \nabla\Phi$ ($\mathbf{A} = 0$) yields a Hamiltonian naturally containing SOC:

$$\hat{H} = \frac{\mathbf{p}^2}{2m} + e\Phi - \frac{\mathbf{p}^4}{8m^3c^2} - \frac{e\hbar}{4m^2c^2}\boldsymbol{\sigma}\cdot(\mathbf{E}\times\mathbf{p}) - \frac{e\hbar^2}{8m^2c^2}\nabla\cdot\mathbf{E} \ . \tag{2.16}$$

Here, the third term stems from the relativistic dependence of the kinetic energy on the momentum, the fourth corresponds to SOC, while the last term is the so called Darwin term, that is only non-zero at points with charges creating the electric field.

Now, if we regard an electric field generated by a hydrogen-like potential $\Phi = -\frac{Ze}{r}$, *i.e.*

$$\mathbf{E} = -\frac{\mathbf{r}}{r}\frac{\partial\Phi}{\partial r} = \frac{Ze}{r^3}\mathbf{r} \ , \tag{2.17}$$

and again identify $\mathbf{r}\times\mathbf{p} = \mathbf{l}$ and $\boldsymbol{\sigma} = 2\mathbf{s}$, the third term in Eq. 2.16 takes the same form as Eq. 2.7

2.2 Spin-Orbit Interaction in Solids

Before we can understand the effect of SOI on electrons in a solid, we first need to understand, how the quantummechanical description of electrons in a solid differs from electrons in an atom. I will therefore give a short introduction to Bloch theory [21] before turning to specific effects.
Only after this, I will turn to the Dresselhaus and Rashba effects, the most prominent direct consequences of SOI in solids.

2.2.1 Detour: Band Structure

This introduction to Bloch theory shall serve as a reminder, not a full derivation. For the reader unfamiliar with this fundamental theory of solid state physics, I suggest an introductory course, *e.g.* by Ibach and Lüth [76] or Kittel [89].

In a solid, the valence electrons of an atom will interact with the electrons and cores of neighboring atoms, forming bonds between the atoms. This bonding, depending on the character of the bond, will lead to different magnitudes of delocalization of the valence electrons in the solid. Especially in metals and semi-conductors, the valence electrons will be highly delocalized, demanding for a different description than in the atomic model.

Bloch was the first to exploit the periodicity of the atomic lattice and therefore the potential experienced by the valence electrons. He introduced so called Bloch wave functions, which are eigenstates of the Hamiltonian of an electron in a periodic potential:

$$\psi(\mathbf{r}) = e^{i\mathbf{k}\cdot\mathbf{r}} u_k(\mathbf{r}) \ , \tag{2.18}$$

where $\mathbf{k}$ is a vector of real numbers and $u_k(\mathbf{r})$ is a function with the same periodicity as the crystal lattice. In other words, a Bloch wave is a plane wave multiplied with a periodic function.

The vector $\mathbf{k}$ describes the electron's momentum. However, due to the translational symmetry of the crystal lattice, $\mathbf{k}$ is only uniquely defined in the first Brillouin zone (BZ) of the crystal. This means, adding any reciprocal lattice vector $\mathbf{G}$ (the Fourier transforms of the real space lattice vectors $\mathbf{R}$) to $\mathbf{k}$ cannot change the corresponding eigenvalue $E(\mathbf{k})$. However, also $u_k(\mathbf{r})$ is not uniquely defined, leading to a plethora of eigenvalues $E_m(\mathbf{k})$, the so called band structure (BS). These states are then filled with the valence electrons of the solid, up to a maximal energy called Fermi level E_{F}.

The relationship between E and $\mathbf{k}$, *i.e.* the shape of the energy bands, especially around the Fermi level E_{F} determines the electronic properties of a solid. These bands, as they are typically derived from the original atomic valence orbitals, will retain some of the symmetry properties of the atomic levels, while being also highly influenced by the periodic crystal field.

One of the most important differences is, whether there is a gap in the BS around the Fermi level. If not, electrons can be easily moved by an external electric field. The material is then a metal. If there is a gap, however, this is not possible. The material is then a semi-conductor or an insulator. The difference between the latter is merely the size of the band gap. Dopants, *i.e.* defects in the crystal lattice, be they intrinsic or by introducing small fractions of atoms of a different element into the crystal structure, can shift the Fermi level of a semi-conductor, in rare cases up to the point where it will intersect with one of the bands again. This is the case in both Bi_2Se_3 and BiTeI, making them so-called degenerate semi-conductors, with properties similar to semi-metals.

2.2.2 The Dresselhaus Effect

We now want to discuss the effects of SOI on the electrons in a BS. It stands to reason, that the SOS of the binding energy of the electronic eigenstates in the atom will translate in one way or another to the electronic eigenstates in the solid. In fact, the SOS will become **k**-dependent and can split bands with different symmetries in combination with the crystal field, especially away from the high-symmetry points of the BS. A minute explanation of this is *e.g.* given in [39].

This splitting, generally, will depend on j and not lead to a spin-polarization of the bands. In order to achieve spin-polarized bands, further requirements have to be met. Time-reversal symmetry, present in all systems without external magnetic fields or ferromagnetic coupling, imposes Kramers degeneracy theorem:

$$E\left(\mathbf{k},\uparrow\right) = E\left(-\mathbf{k},\downarrow\right) \ . \tag{2.19}$$

If inversion symmetry is additionally present, which in turn imposes

$$u_{-\mathbf{k}}\left(\mathbf{r}\right) = u_{\mathbf{k}}\left(-\mathbf{r}\right) \tag{2.20}$$

on the Bloch wave functions, no lifting of the spin-degeneracy of the bands is allowed. However, in non-inversion symmetric systems, such as crystals with zincblende lattice, a lifting of the spin-degeneracy by SOI is possible, as first described by Dresselhaus in 1955 [19, 38].

Dresselhaus predicted a spin-splitting that is cubic in **k**. The so-called Dresselhaus Hamiltonian for these structures is now generally written as:

$$H_{\mathrm{D}} = \mathrm{D}\,\boldsymbol{\Phi}_{\mathrm{D}} \cdot \vec{\sigma} \ , \tag{2.21}$$

where D is a constant, $\vec{\sigma}$ is the spin-vector, consisting of the Pauli matrices $\sigma_x, \sigma_y, \sigma_z$ and

$$\boldsymbol{\Phi}_{\mathrm{D}} = \left(k_x\left(k_y^2 - k_z^2\right), k_y\left(k_z^2 - k_x^2\right), k_z\left(k_x^2 - k_y^2\right)\right) \ . \tag{2.22}$$

In 2D nanostructures, this term can be separated into a linear and a cubic component, of which the linear term is the most well-known one:

$$H_{\mathrm{D}}^{(2D,lin)} = \beta\left(\sigma_x k_x - \sigma_y k_y\right) \ . \tag{2.23}$$

This term leads to Fermi-surfaces with a quadrupole-like spin-splitting (c.f. Fig. 2.1 a).
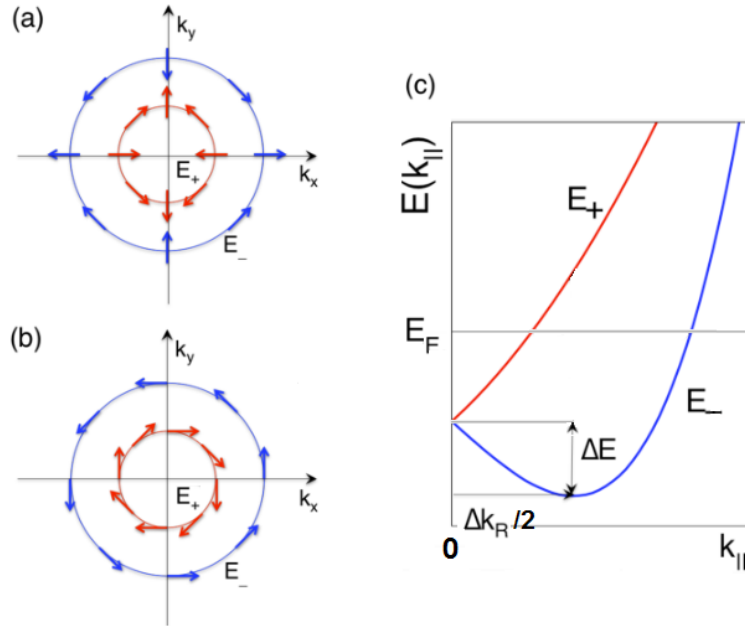
Figure 2.1: a) Spin-structure at the Fermi surface of a 2D free electron gas spin-split by the Dresselhaus effect. b) Spin-structure at the Fermi surface for the Rashba effect. c) Schematic of the corresponding dispersion. Figure adapted from [84].

2.2.3 The Rashba Effect

An effect similar to the Dresselhaus effect is the Rashba effect. It was first described by Rashba and Sheka in 1959 [149]. Rashba then reformulated the description together with Bychkov in 1984 for a two-dimensional system [28, 29], in order to explain then recent measurements on semiconductor heterostructures [171, 172].

Rashba and Sheka showed, that in semiconductors with wurtzite crystal structure, $E(\mathbf{k})$ is linear in $\mathbf{k}$ near the Γ point of the BZ, *i.e.* at $\mathbf{k} \approx 0$. They proposed the simple model Hamiltonian

$$H_R = \alpha \left(\vec{\sigma} \times \mathbf{k} \right) \cdot \mathbf{v} \ , \tag{2.24}$$

where $\mathbf{v}$ is pointing along a high symmetry axis of the crystal [28, 29]. For a 2D system, *e.g.* a surface state, $\mathbf{v}$ becomes the normal direction $\mathbf{z}$ and the Rashba-term then becomes

$$H_R^{2D} = \alpha \left(\sigma_x k_y - \sigma_y k_x \right) \ , \tag{2.25}$$

which is, in structure, very reminiscent of Eq. 2.23, but leads to a chiral spin pattern around the Fermi surface (c.f. Fig. 2.1b).

Let us have a look at the solutions of the Schrodinger equation of a 2D free electron gas with effective mass $m^\star$:

$$\left(\frac{\hbar^2 \hat{\mathbf{k}}^2}{2m^\star} + \alpha \left(\vec{\sigma} \times \mathbf{k} \right) \cdot \mathbf{z} \right) |\psi\rangle = E|\psi\rangle \; . \tag{2.26}$$

The eigenvalues of this equation are

$$E_\pm(k) = \frac{\hbar^2 k^2}{2m^\star} \pm \alpha k \; , \tag{2.27}$$

which corresponds to two free-electron parabolas, which are offset in $k = |\mathbf{k}|$ (c.f. Fig. 2.1c).

The magnitude of the splitting is naturally determined by the SOI, but is also related to the inversion-asymmetry of the wave functions [138] and/or potential gradient in the crystal or at the surface [18, 160, 166]. In fact, this can be exploited, as the surface potential gradient can be manipulated by applying external fields, making it possible to tune the splitting in certain semiconductor heterostructures [46, 128, 165].

2.3 Topological Insulators

The term topological insulator (TI) refers to a certain phase of matter, that - among other properties - features peculiar surface states. This field of fundamental physics has only been discovered and described rather recently, when Thouless, Haldane and Kosterlitz first applied the mathematical concept of topology to the BS of solids [62, 176]. In 2016, they were rewarded with the Nobel prize for these findings.

The mathematical field of topology deals with properties that are conserved under smooth transformations. The most accessible example is the classification of closed 2D surfaces in three dimensions: The transformation from a doughnut shape to a coffee-mug shape can be performed smoothly, *i.e.* by stretching and compressing of the surface. Meanwhile, the transformation from a ball shape to a doughnut shape requires the tearing of a hole and reconnection of the surface. Surfaces can therefore be classified by the amount of holes they possess, *i.e.* the number of holes is a topological invariant.

It has been discovered, that the BS of solids can be classified by a plethora of conserved symmetries and related invariants. In fact, a whole periodic table of different topological states has been created [13, 88, 143, 162].
Simply spoken, the symmetry properties of the electronic states determine whether an insulator, *i.e.* a material with a band gap at the Fermi level, is a topologically "trivial" or "non-trivial" one. I will try to elucidate, what this means specifically for three-dimensional TIs characterized by time-reversal symmetry, as Bi_2Se_3 belongs to this group.

A priory, the concept of topological matter seems unrelated to SOI. And indeed, in contrast to Rashba splitting, the topological phase is not a straight forward consequence of SOC. However, it is mainly found in materials containing heavy elements, *i.e.* in materials with strong SOC. Fu and Kane have shown, that in semiconductors with inversion symmetry, strong SOC is indeed a necessary requirement to form a TI [13, 55].

While the concept of TIs is rather complicated and not in depth necessary to understand the results presented in this thesis, I will nevertheless try to give a rough, more phenomenological introduction. The interested reader shall be referred *e.g.* to reviews by Hasan and Kane [64], Qi and Zhang [144], Hasan and Moore [65], as well as the book by Bernevig and Hughes [13]. Alternatively, Ch. 3 of M. Scholz's dissertation [163] gives a more detailed introduction from an experimentalist's point of view.

2.3.1 Discovering Topological Matter: An Abridged History

Even though Bloch's theory of the band structure stems from the 1920s [21] and the mathematical field of topology has been around since the eighteen hundreds [183], it was not until the 1980s, that both fields were brought into contact [62, 64, 176].

The initial observation, that kickstarted the field of topological matter was that of the integer Quantum Hall Effect (IQHE): von Klitzing *et al.* observed in 1980, that the Hall conductance of the 2D electron gas in a MOSFET is quantized at large magnetic fields ($B \approx 15\,\mathrm{T}$) [90]:

$$\sigma_{xy} = -N\frac{e^2}{h}\ ,\tag{2.28}$$

where N is integer to one part in one billion [91].

Von Klitzing *et al.* explained their findings with the emergence of so-called Landau levels: The magnetic field forces the electrons in the 2D electron gas on circular orbits, leading to quantized energy levels separated by the cyclotron frequency ω_c:

$$E_m = \hbar\omega_c\left(m + \frac{1}{2}\right)\ .\tag{2.29}$$

The BS of such a system, therefore, consists of completely flat, degenerate bands. Driving the Fermi level through the Landau levels by a gate voltage will lead to stepwise increases of the charge carrier concentration and therefore to a quantized conductance.

However, it was Laughlin who first pointed out that the level of quantization in this system is too sharp for a real system. Therefore, he proposed that a fundamental principle must lead to the emergence of the IQHE [106].
One year later, Thouless *et al.* found that this underlying principle can be found in the mathematical field of topology [176]. They formulated a classification of the band structures of an insulator in terms of a topological invariant, that remains robust under

smooth transformations of the Hamiltonian.

In 1988, Haldane *et al.* then proposed a topological state that required no external magnetic field, the so called Chern insulator [62]. This state, however, has not been experimentally realized so far.

The field of TIs has gained new impetus in the 2000s, when topological phases reliant on time-reversal symmetry have been proposed that could be experimentally observed [14, 15, 55, 56, 81, 82]. These are the so called Quantum Spin Hall (QSH) systems, which are the most commonly discussed among the TIs.

The first ones to be experimentally observed, were HgTe quantum wells, sandwiched between (Hg,Cd)Te barriers [92]. If the stochiometry and width of the components is chosen correctly, the parity of the valence and conduction band will be reversed in the HgTe quantum well as compared to the surrounding barriers, which means, that the BS of the HgTe quantum well is topologically different.

Shortly after, Hsieh *et al.* discovered the first three-dimensional material with topologically non-trivial BS: an alloy of bismuth and antimony, $Bi_{1-x}Sb_x$. [73]. On this material, the first DCs have been observed with photoemission. Just one year later, two compounds of the family Bi_2X_3 joined the ranks of proven TIs [74]. Ever since, the field has been continuously growing, and additionally to the focus on finding more new materials and topological phases, a second focus on understanding and harnessing the physical properties of this phase of matter has been established.

2.3.2 Chern Numbers and Chiral Edge States: Properties of Topological Insulators

In this section, I want to introduce the theoretical foundations as well as their phenomenological consequences. A natural starting point seems to be the topological invariants characterizing the different topological phases. The topological invariant characterizing the IQHE is called Chern number, after the mathematician Shiing-Shin Chern. It is strongly related to the Berry flux

$$\mathcal{F}_m = \nabla \times i \langle u_m | \nabla_k | u_m \rangle \ , \tag{2.30}$$

where u_m are the periodic parts of the Bloch functions (c.f. Eq. 2.18). The Berry flux is therefore the flux of the Berry phase, which is the phase of the Bloch function picked up when adiabatically transported around a closed loop in **k**-space [16].

The Chern number n_m is then simply given by the integral of the Berry flux

$$n_m = \frac{1}{2\pi} \int d^2 \mathbf{k} \, \mathcal{F}_m \ . \tag{2.31}$$

Without an external magnetic field, n_m will vanish, as it can only be non-zero when time-reversal symmetry is broken.

Even though n_m is a bulk property, its effect can mainly be observed at the edges of the system: It has been shown, that n_m gives the number of conducting edge channels [63] in the IQHE phase [66]. Phenomenologically, one can imagine these states as skipping orbits of electrons at the edges of the sample, which cannot complete their cyclotron motion due to the edge.

There are two things important to note here:
First, these discussed edge states are chiral, *i.e.* there is only one possible direction of motion on each edge, dictated by the cyclotron orbits. This means, backscattering is forbidden.
Second, the edge channels emerge from a bulk property and are therefore insensitive to defects at the edges. If we keep in mind, that backscattering is forbidden, it is easy to see, why. As a consequence, a charge in the edge channel will simply flow around defects and continue along the edge.

To be a bit more precise, n_m defines the difference between the number of right and left moving edge states, N_r and N_l. This is often referred to as bulk-boundary correspondence:

$$N_r - N_l = n_m \ . \tag{2.32}$$

Now we want to discuss the so-called QSH phase. As we have already established, it relies on the conservation of time-reversal symmetry, in contrast to the IQHE phase. For any time-reversal invariant system, Kramers theorem applies, *cf.* Eq. 2.19. In general, the invariant defining such a system is called $\mathbb{Z}_2$ invariant and the letter ν is chosen to stand for it. ν separates trivial insulators ($\nu = 0$) from the QSH phase ($\nu = 1$)

There are several ways to define ν [54, 55, 58, 59, 81, 117, 143, 155, 182]. However, for the scope of this thesis, the introduction of none of these mathematical definitions seems instructive. In summary, it suffices to know that ν is computed from the occupied Bloch functions and therefore an intrinsic property of the eigenstates. It does not suffice to know the dispersion of the BS, *i.e.* the relation $E(\mathbf{k})$ of the eigenvalues of the Hamiltonian.

The calculation of ν becomes easier, if further symmetries of the system can be exploited. The most prominent is the case of crystals with inversion symmetry. In this case, the $\mathbb{Z}_2$ invariant can simply be computed from the parity p_m of the occupied Bloch eigenstates u_m at those momenta $\mathbf{k}_i$, which are both time-reversal invariant momenta (TRIM) and inversion symmetric:

$$(-1)^\nu = \prod_i \prod_m p_m(\mathbf{k}_i) \ , \tag{2.33}$$

where m runs over all occupied states [55].

This insight makes it very clear, why the inversion of band parity in HgTe-Quantum wells leads to a topologically non-trivial state (c.f. Sec. 2.3.1). Such an inversion of band

parity across the primary band gap can only be achieved by SOI, making it a necessary requirement for non-trivial band structures in materials with inversion symmetry [55].

The transition from a trivial to a non-trivial insulator does not only mathematically require the closing of the band gap, but also physically. This leads to the emergence of protected edge or surface states on the boundaries of TIs. For the 2D-case, they can be envisioned as Kramers-paired copies of the IQHE edge states, *i.e.* two counter-propagating edge states with inverse spin to one another. Please note that at the surface, inversion will be broken even if it is present in the bulk, so surface states are allowed to be spin-polarized, even in time-reversal invariant and inversion symmetric systems (c.f. Sec. 2.2.2).

Due to Kramers theorem, we know that the dispersions of both edge states have to intersect at TRIM, which is only at $\mathbf{k} = 0$ for 1D edge states. Furthermore, the dispersion of these states is typically linear near the crossing point, like massless relativistic fermions. Each of these channels contributes exactly one quantum of conductance e^2/h.

2.3.3 Three Dimensional Topological Insulators

The QSH phase has initially only been described for 2D structures, mainly graphene (which shows an extremely small effect due to almost negligible SOI, only visible at very low temperatures) [82] and HgTe quantum wells [14]. In 2007, the concept was generalized to three dimensions [56, 117].

The largest difference to the two-dimensional case described above, is that now four invariants $(\nu_0; \nu_1 \nu_2 \nu_3)$ are necessary to describe the topological phase [56]. This has to do with the number of TRIM on the surface BZ.
The first of the four invariants determines whether a 3D TI is "strong" or "weak", meaning whether its TSSs persist in the presence of disorder or not and whether it is present on all surfaces [64]. The easiest way to form a weak 3D TI is a stack of 2D TIs, whose surface states are then anisotropic. Strong 3D TIs, however, cannot be derived from 2D TIs. The following discussion will focus purely on strong 3D TIs.

Similar to the edge states of 2D QSH materials, 3D TIs have spin-polarized surface states with linear dispersion. The bulk-boundary correspondence (c.f. Eq. 2.32) then translates to the fact, that there has to be an odd number of intersections of TSSs with the Fermi level on a 3D TI.
At the TRIM, these TSSs have to be Kramers degenerate, forming the so called Dirac points (DPs). The whole dispersion of the TSS typically forms a cone-like structure around these points, therefore they are also often referred to as DCs. The spin of these surface states is locked perpendicular to the momentum, leading to a chiral spin-texture, not unlike one of the Fermi-circles of a Rashba state (c.f. Fig. 2.1b). However, unlike the Rashba state, the DC spans the entire band gap and is therefore always metallic, independent of doping or applied gate voltages, due to the bulk-boundary correspondence.

Such characteristic surface states are ideally observed with angle-resolved photoemission spectroscopy (ARPES), at least the occupied parts. Additionally, the signature of the surface states in the conductivity is less characteristic than in the 2D case, as bulk contributions typically cloud the surface contributions. This made ARPES the primary experimental tool for the identification of 3D TIs.

The first observed 3D TI is the alloy $Bi_{1-x}Sb_x$ [73]. Even though both constituents, bismuth and antimony, are semi-metals in their elemental form, a certain stochiometry range exists (between $x = 0.07$ and $x = 0.22$), where the alloy possesses a final overall band gap with non-trivial topology. The TSS of $Bi_{1-x}Sb_x$ crosses the Fermi level not once, but five times between the $\overline{\Gamma}$ and $\overline{M}$ points of the surface Brillouin zone.

The so-called second generation TIs are Bi_2Se_3, Bi_2Te_3, and Sb_2Te_3 [31, 74, 75, 118]. The surface BS of these materials is significantly less complicated than that of $Bi_{1-x}Sb_x$, with a single nearly-ideal DC spanning the comparably large band gap of a few hundred meV at the $\overline{\Gamma}$ point. The two bismuth-derived compounds lend themselves especially to the study with ARPES, as they are intrinsically n doped by defects in the crystal structure, moving the Fermi level into the conduction band (CB) and leading to an occupied TSS. Antimony-derived compounds show the inverse intrinsic doping, with the Fermi level shifted into the valence band (VB).

Out of the three second generation TIs, Bi_2Se_3 is quite possibly the most studied one, *e.g.* in [30, 33, 79, 135, 156, 159, 167, 168, 177, 180, 188, 189] and many more. It distinguishes itself from Bi_2Te_3 by a larger band gap (roughly $0.3\,eV$ vs. $0.15\,eV$) as well as a more ideal DC. In Bi_2Te_3, the DP is buried in a local dip of the VB at the $\overline{\Gamma}$ point. Furthermore, the DC is significantly deformed and shows a six-fold symmetric, star-like Fermi surface [31]. This deformation is typically referred to as hexagonal warping and is caused by the strong trigonal potential of the lattice. This distortion is actually related to Dresselhaus SOC and can be described with the perturbative $\mathbf{k} \cdot \mathbf{p}$ theory [53].

Chapter 3

Experimental Method

The best method to investigate unoccupied electronic states in solids and their dynamics is arguably two-photon photoemission (2PPE). This method allows to image electrons excited to the unoccupied states of a solid by photoexciting the sample first with an ultrashort laser pulse and then photoemitting the excited carriers with a second laser pulse.

In this chapter, I will discuss the basics of this method as well as the experimental setup by which it is applied throughout this thesis.

3.1 Principles of Two-Photon Photoemission

2PPE is a special form of photoemission spectroscopy (PES), a tool widely used in solid state physics. All forms of photoemission experiments are based on the photoeffect, which was first observed by Hertz in the 19th century [69] and later theoretically described by Einstein [44]. This section will first describe the fundamentals of PES before turning to the specifics of time- and angle-resolved photoemission spectroscopy (tr-ARPES) and 2PPE.

3.1.1 Photoeffect and Photoelectron Spectroscopy

In the 19th century, it was observed that shining light on a solid can lead to the emission of electrons, the so called photoelectrons. This will only happen if the photon energy $h\nu$ exceeds the solid's work function Φ, *i.e.* the difference between energy of the Fermi level E_F and the vaccuum level E_vac. The kinetic energy of the emitted electron can be determined according to energy conservation:

$$E_\text{kin} = h\nu - E_\text{B} - \Phi \ , \tag{3.1}$$

where E_B is the binding energy of the electron, *i.e.* the difference between its initial energy E_init and E_F (*cf.* Fig. 3.1).

Several experimental techniques use the photoeffect to gain information about the sample. They are all summed up under the term photoemission spectroscopy (PES). Light sources used for PES can range from table-top laser setups and gas-discharge lamps to synchrotrons and free-electron lasers. The photoelectrons are detected in most setups
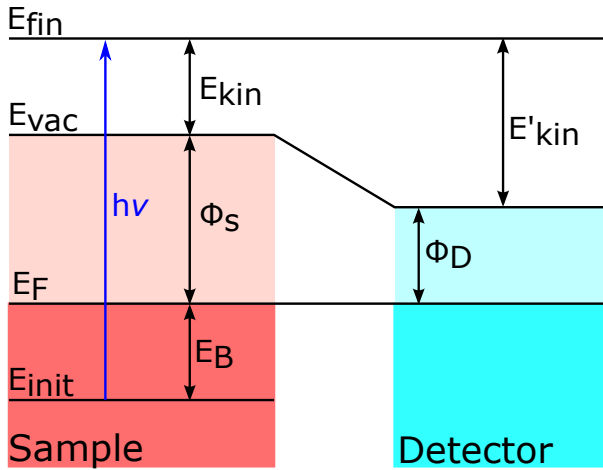
Figure 3.1: Energy scheme for photo-electron spectroscopy. E_{init} and E_{fin} are initial and final energy of the electron, $h\nu$ is the photon energy, E_F is the Fermi level of sample and detector. The difference between vacuum E_{vac} level and Fermi edge is called work function Φ. The work function can be different between sample and detector, leading to a change in the kinetic energy E_{kin}. Figure adapted from [85]

either by hemispherical analyzers or time-of-flight spectrometers, to determine the kinetic energies of the photoelectrons.

In this case, the work function differences between sample and detector have to be taken into account, as well as potential acceleration or deceleration voltages applied in between, as both alter the kinetic energy (*cf.* Fig. 3.1).

In case the detector work function Φ_D is known, the sample work-function can be directly determined from the so called low-energy cutoff. This is the lowest kinetic energy at which photoelectrons are detected. This energy plus the detector work-function then give the sample work-function. In case $\Phi_S < \Phi_D$, one has to apply a bias between the sample and detector to access the cutoff.

PES is known for being very surface sensitive. However, it is not limited by the penetration depth of light into the samples, but rather due to the short escape depth of the electrons. Typically, only electrons from the first few atomic layers of the sample can escape via photoeffect without undergoing scattering during the process. Electrons inelastically scattered during the photoemission process will change their initial energy and momentum and therefore lead to a background signal, that increases towards the low-energy cutoff.

The exact depth for energy and momentum conserving photoemission depends on the incident photon energy, or, more precisely, on the photoelectron's kinetic energy. With photon energies of several keV, which can be achieved with synchrotron light sources, also bulk band structures and buried interfaces can be analyzed. With low energy photoelectrons, the issue of surface over bulk sensitivity is less clear: In general, it is assumed, that the lowest escape depth is reached for electrons with kinetic energies in the range of 50-100 eV, increasing again towards lower kinetic energies. The so called universal curve assumes escape depths as large as 100 Å for electrons with few eV kinetic energy, as investigated in this thesis. However, this increase of escape depth at low electron energies might not be as universally valid as implied [40].

3.1.2 Momentum-Resolution in Photoemission

Like the kinetic energy, the momentum of photoelectrons follows strict rules in the photoemission process as well, which can be exploited to gain further information about the samples' properties. Experimental methods, where both the photoelectrons kinetic energy and momentum are measured, are summed up under the term angle-resolved photoemission spectroscopy (ARPES).

Momentum conservation within a crystal demands that

$$\vec{k}_f = \vec{k}_i + \vec{q} + \vec{G}_{hkl} \ , \tag{3.2}$$

where $\vec{q}$ is the momentum of the absorbed photon and $\vec{G}_{hkl}$ is a reciprocal lattice vector. As the photon momentum is usually much smaller than the electron momentum, we can neglect it. Also, we can take into account $\vec{G}_{hkl}$ by using the reduced zone scheme and end up with the same final momentum as initial momentum of the electron within the solid. Upon exciting the sample, the momentum components parallel to the surface have to be conserved due to symmetry reasons. However, the component perpendicular to the surface will change to overcome the energy barrier. This limits the momenta accessible with a certain photon energy $h\nu$ (*cf.* Fig. 3.2). This range is further limited by the finite acceptance angle θ_D of the detector.

When both kinetic energy and momentum of the photoelectrons are measured, the band structure of the sample can be inferred. Surface states do not disperse perpendicular to the surface, *i.e.* their energy does not change with this momentum component. Therefore, the measurement of E_{kin} and $k_{||}$ suffices to map the entire surface band structure. However, bulk states possess dispersions in all three momentum directions, making the study of bulk bands more challenging due to two reasons: First, they are only accessible, if final states fulfilling both energy and momentum conservations are accessible with the employed photon energies. Second, the momentum component perpendicular to the surface has to be determined by triangulation or by assumptions to the change in momentum during the transition from sample to vacuum.

Most types of analyzers don't measure the parallel momentum directly, but the angle θ, under which the electrons leave the surface. However, from Fig. 3.2 and keeping in mind that $k = \sqrt{2m_e E_{\text{kin}}}/\hbar$ in vacuum, we find that $k_{||}$ of the electron is purely determined by E_{kin} and the emission angle θ:

$$k_{||} = \frac{\sqrt{2m_e E_{\text{kin}}}}{\hbar} \cdot \sin\left(\theta\right) \ . \tag{3.3}$$

The spectrometer used in this thesis and the method to obtain kinetic energy and parallel momentum out of the raw data are described more in-depth in Sec. 3.2.2.
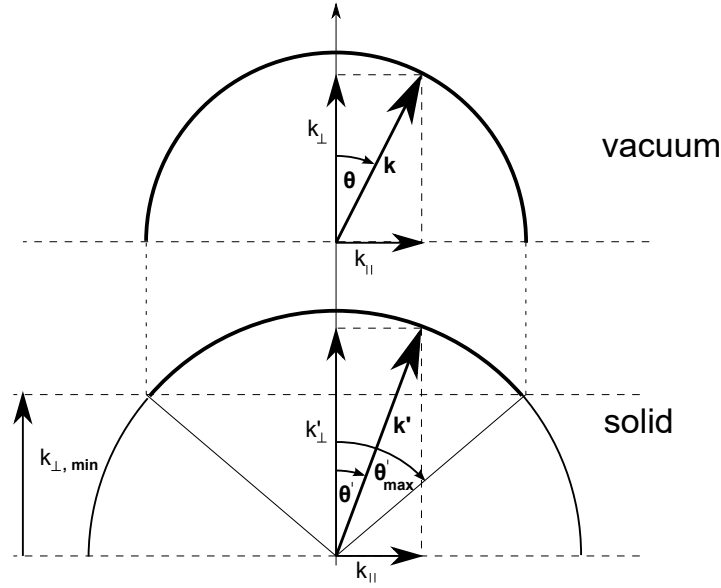
Figure 3.2: Behavior of the momentum **k** of the photoelectron upon transmission through the sample surface. To overcome the work function difference, the total momentum **k**′ has to change. As the symmetry is only broken along the sample normal, exclusively the momentum component perpendicular to the sample $k'_\perp$ is changed. The components parallel to the surface $k'_{||} = k_{||}$ are not affected. This means, the photoelectron has to possess a minimal component $k'_{\perp,\text{min}}$ within the sample, limiting the accessible range of $k'_{||}$. Figure adapted from [100].

3.1.3 Time-Resolution in Photoemission

A likely expansion to photoemission spectroscopy is adding time-resolution in a pump-probe scheme. For this, the sample is first excited with an ultrashort laser pulse with photon energy below the work function. Then a second pulse with higher photon energy is used for the photoemission process.

In general, there is a distinction made between two different time-resolved modes for PES. In so called two-photon photoemission (2PPE), the photon energy of the second pulse does not surpass the work function either, photoemitting only electrons that were previously excited. This makes 2PPE a process described by second order perturbation theory, leading to much smaller intensities in the photoemission spectra compared to direct photoemission [179]. However, it is a very advantageous technique, if the dynamics of the unoccupied states is the focus of the experiment, as the intensity from direct photoemission can obscure the time-dependent signal, especially at low excitation densities, *i.e.* low laser intensities. Due to the character of the 2PPE final state at low kinetic energies, typically an evanescent state, 2PPE is especially surface sensitive. 2PPE is applied in chapter 4.

In time- and angle-resolved photoemission spectroscopy (tr-ARPES), the second pulse

has a photon energy higher than the work function of the sample, so that electrons are emitted from the occupied states as well. However, it requires big excitation densities in order to achieve reasonable time-dependent signals in comparison to the background of direct photoemission. This method is advantageous, if the focus of the experiment is the dynamics of the occupied states or a comparison of occupied and unoccupied states, as presented in Ch. 5.

In both methods, the delay, *i.e.* the difference in time of incidence, between the two incident light pulses is varied during the measurements. This leads to stroboscopic glimpses of the transient electron population at the specific time before, during or after excitation. A series of these measurements with systematically increasing delay can be pieced together to observe the temporal evolution of the system during and after excitation. The dynamics of the intermediate states becomes visible, as the photo-electron (PE) intensity in the respective regions of kinetic energies will decrease with the depletion of the intermediate states. This makes time-resolved methods especially interesting for studying semiconductors and other materials in opto-electronics, where the photoexcitation of currents and the electronic behavior after photoexcitation play a major role for application.

The temporal resolution of both tr-ARPES and 2PPE is limited by the temporal width of the employed light pulses, *i.e.* their so-called cross-correlation. However, the uncertainty principle (or, simply, Fourier transformation) demands that the product of spectral bandwidth $\Delta\nu$ and temporal width Δt of each individual pulse stays above the threshold

$$\Delta\nu\Delta t \geq \frac{1}{4\pi} \; . \tag{3.4}$$

This means, that temporal resolution always comes at the cost of spectral resolution. In the presented experiments, the temporal resolution stays in the regime of a few tens of femtoseconds, while the observed features of the band structures are broadened to a few dozen meV.

In principle, also shorter time scales than the cross correlation of the pulses can be observed by fitting the spectra with suitable functions, typically an exponential decay convoluted with a Gaussian. However, the exact width and position of the cross correlation has to be known and only timescales in approximately the same order of magnitude can be resolved.

During PE, initial, intermediate and final states can cause features in the resulting spectra, because the symmetries of all three types of states influence the transition matrix elements. An example of this is discussed in depth in ch. 4. The contributions can be disentangled by changing pump and/or probe photon energies, as the signatures of initial and intermediate states will move differently in kinetic energy, depending on the changes. Alternatively, the temporal evolution of the states is a clear indicator of their character, as the PE signal from intermediate states will usually feature finite lifetimes, while the signal from initial states will show a time-dependence of its intensity proportional to the cross correlation of the two pulses. Thus, to a certain extend, the

occupied and unoccupied band structure can be mapped at the same time even with 2PPE [60].

3.2 Setup

As we've seen in the previous section, time-resolution in PES requires ultrashort laser pulses, ideally with tunable energy, for the emission of photoelectrons and a setup for the detection and analysis of kinetic energy and momentum. As the photoelectrons need to reach the detector without scattering events, sample and detector are best situated under ultrahigh vacuum (UHV) conditions. Furthermore, this way the contamination of the surface can be kept to a minimum. In addition, stray magnetic and electric fields will influence the electron trajectories and therefore would distort the measured photoelectron spectra. To avoid this, the sample and detector are surrounded by a cylindrical μ-metal shield.

In this section, I will first describe the laser system employed for the experiments of this thesis followed by an introduction of the spectrometer utilized and a description of its advantages over the more common hemispherical analyzers.

3.2.1 Laser

The pulses used for the PE experiments are provided by a laser beamline consisting of generation and amplification of the pulses and multiple non-linear stages. Depending on the requirements of the experiments, different stages can be selected to obtain the desired wavelength for excitation (pump) and photoemission (probe) pulses. The parts of the system, that were actually used in the experiments presented in this thesis, are sketched in Fig. 3.3.

The basic light source is a *Verdi G18* diode laser, providing a continuous wave beam with a wave length of 532 nm at a power of 13.6 W. The beam is divided by a beamsplitter, which leads 30% of the intensity into a self-built titanium sapphire (Ti:Sa) oscillator cavity and 70% into a regenerative amplifier (RegA).

The oscillator cavity delivers 30 fs pulses with a central wavelength of 790 nm and a frequency of 76 MHz generated *via* mode-locking. The method employed to achieve mode-locking is Kerr lensing. This means that the intensity dependence of the refractive index of the Ti:Sa crystal is exploited in the geometry of the cavity. The intensity of a contiuous single-mode output is too small to lead to significant self-focussing inside of the crystal and is therefore partially suppressed in the cavity. When the cavity is disturbed externally by shifting one of the end mirrors mechanically, side modes are excited. Those modes interfering constructively within the crystal will be amplified, thus leading to a short pulse. The output of the seed has a power of about 400 mW and
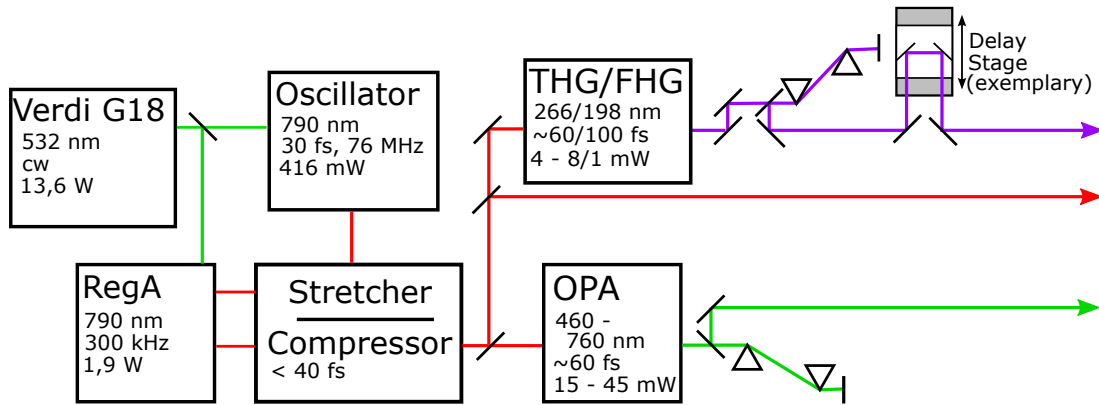
Figure 3.3: Schematic of the laser setup used for the experiments. Ultrashort laser pulses are generated in the oscillator and amplified in the RegA after stretching. The recompressed amplified pulses can be modified by several non-linear setups: an OPA for creation of light in the visible range, equipped with an optional SH stage and a THG or FHG unit for the fundamental wavelength. In this way, excitation and photoemission wavelength can be adapted to the requirements of the different experiments.

an energy of 5.5 nJ per pulse, which is not sufficient for the non-linear stages. Therefore, it is amplified in the RegA.

In the RegA, the continuous wave beam of the *Verdi G18* pumps another Ti:Sa crystal. An optoacoustic modulator is used as a Q-switch to suppress lasing by bending the beam out of the cavity. When maximum population inversion of the lasing electron levels in the Ti:Sa is reached, a second optoaccoustic modulator (cavity dumper) couples the seed-pulse into the cavity. At the same time the settings of the first optoaccoustic modulator are changed to increase the Q-factor and make lasing possible. The pulse is amplified during approximately 28 round trips and then coupled out by the cavity dumper again. The output has a power of 1.8 to 2.0 W and a repetition rate of 300 kHz. As the power of the short seed pulse would exceed the damage threshold of the RegA elements during amplification, it is temporally stretched before entering the RegA. In the stretcher, a grating disperses the different frequencies of the pulse spatially, which then travel different distances before being brought back together, leading to a long, chirped pulse. This process is reversed in the compressor after amplification in the RegA to obtain the desired short pulses again. Unfortunately, the three processes of stretching, amplification and compression slightly reduce the bandwidth of the pulse so that the amplified pulse has an increased duration of approximately 40 fs.

After the compression, the beam is split. The two pulses can be independently manipulated to achieve the desired wavelengths. One possibility is to guide the pulse into an optical parametric amplifier (OPA)[1] equipped with an optional subsequent second-harmonic generation (SHG) unit. Additionally, the laser is equipped with a unit for

---

[1] *Model 9400* by *Coherent*

third-harmonic generation (THG) or fourth harmonic generation (FHG) of the fundamental. Alternatively, the fundamental frequency can be used directly.
In the experiments, where the OPA was employed, the beam is split with a 50/50% ratio, otherwise with a 30/70% ratio.

In the OPA, wavelengths from 460 to 760 nm can be created by the following mechanism:
The incoming beam is first split in a 25/75% ratio. 25% of the intensity is focussed into a sapphire crystal. The refractive index of sapphire is intensity dependent and therefore the flanks of the pulse obtain a temporally dependent phase shift, extending the flanks into the visible and infrared regime. In other words, this generates a long, chirped pulse with one flank spanning the visible spectrum.
The remaining 75% of the initial pulse is frequency doubled in a β-barium borate (BBO). Both beams are then collinearly focussed into a second BBO, where the temporal overlap of the UV pulse with the white light determines, which wavelength is amplified by difference frequency generation (DFG). We chose wavelength of 720 or 650 nm for the experiments on Bi_2Se_3 (*cf.* Ch. 4). After the amplification of a single visible wave length, a second round trip through the BBO strongly amplifies the pulse at the desired wavelength. The amplified wavelength is then separated from the other components by dielectric mirrors and coupled out of the OPA.
This output of the OPA is guided through a prism compressor to post- and pre-compensate chirps picked up in the diverse optical elements. Additionally, residual white light and unwanted side bands of the pulse can be blocked within the prism compressor.

In the THG/THG setup, one third of the fundamental pulse's intensity is split off. The remaining two thirds are sent into a BBO for frequency doubling. The fundamental and second harmonic frequencies are separated by a dielectric mirror, the polarization of the second harmonic (SH) is rotated to match the polarization of the fundamental and they are collinearly focussed into a second BBO for frequency mixing to generate the third harmonic (TH). The TH is then separated from the other two frequencies and compressed in a prism compressor. After compression, the TH can be coupled out of the setup and used directly for photoemission. Alternatively, it can be focussed into a third BBO, together with the initially split off part of the fundamental beam. There, a second step of frequency mixing generates the fourth harmonic (FH), which is again separated from the other frequencies and compressed.

Either the pump or the probe beam is guided over a computer-controlled delay stage, with which the path length of the beam can be varied. The delay stage used has a range of 5.4 cm with a step width of 8.5 nm, which corresponds a range of 360 ps with a resolution of 1.2 fs.

The circular polarization of the pump pulses needed for the experiments on Bi_2Se_3 was achieved with a broad band quarter waveplate. However, the resulting polarization is not perfectly circular due to the broad band character of the waveplate. Further

polarization changes are induced by following mirrors and the window of the vacuum chamber. In order to compensate these imperfections, a Soleil-Babinet compensator is used and the polarization is carefully checked to ensure circular polarization of the beam when it hits the sample.

The pump and probe pulses are united before entering the vacuum chamber, ensuring spatial overlap with the help of several pinholes and temporal overlap with the help of a photodiode. They are guided collinearly onto the sample under an angle of 45°.
The cross correlation of the pulses, characterized on a Cu(111) surface before the measurements on Bi_2Se_3, typically has a full width at half maximum of 60 to 90 fs. Due to the high photon energy of the probe pulse during the measurements on BiTeI, such a caracterization was not possible in this case. Instead, the time constant for depletion of low-lying occupied states on Bi_2Se_3 was used as a reference. These show that the FHG pulses have a significantly longer duration, leading to cross correlations over 120 fs.

The fluence applied to the BiTeI samples (*cf.* Ch. 5) was determined by a two-step process: First, the power of the pump beam was measured at the end of the laser table, shortly before entering the chamber. Secondly, the spot size of the focussed beam was determined at a position corresponding to the sample position. The fluence F then can be determined from the spot size A, the repetition rate f and the average power P:

$$F = \frac{P}{f\,A} \; . \tag{3.5}$$

Due to the many involved non-linear processes, the laser is very sensitive to ambient conditions and can fluctuate significantly in intensity. The measurements taken over a period of one hour or more for satisfying statistics can show irregular strong dips in the laser intensity, which would falsify the dynamics. The presented time-resolved spectra have been averaged over several short measurements recorded with stable laser output power to circumvent these issues. The stability of the laser power during the recording of the photoelectron maps presented in Ch. 4 was also carefully monitored.

3.2.2 Spectrometer

The instrument employed in this thesis to measure the momentum and kinetic energy of the photoemitted electrons is an angle-resolving time-of-flight (ToF) spectrometer (THEMIS, SPECS GmbH). This type of spectrometer determines the electron's kinetic energies by the time they need to travel the distance between sample and detection plate. This way allows for simultaneous recording of kinetic energy, and parallel momentum in two dimensions with a polar acceptance angle of up to ±15°. This means, both k_x and k_y can be measured simultaneously, because in contrast to hemispheric analyzers no spatial direction is needed for the determination of the kinetic energy.
In conventional time-of-flight spectrometers, the electrons pass a drift tube of well-defined length, in the order of several to several dozen centimeters, to determine their

kinetic energy. Thus the detection angle is limited, often to less than 2° from the sample normal. THEMIS is equipped with an electronic lens system instead of the drift tube, which allows for a higher acceptance angle in the lens modes designed for angle-resolved measurements. Additionally to the four angle-resolved modes, the spectrometer features two real space-resolved modes used for alignment.

In this section, I will introduce the working principle of the THEMIS. For a more detailed discussion, *cf.* the PhD thesis of T. Kunze [100] and the Master thesis of M. Bastian [10], which served as a basis for this section.

Lens System and Operating Modes

The lens system of THEMIS consists of cylindrical tubes and has originally been developed for a hemispherical analyzer. A schematic is shown in Fig. 3.4a). The electron lens is equipped with a so called micro tip, an extension that is in contact with the first lens segment and therefore at the same potential, to minimize the electron's path in stray fields outside the detector. The electrons enter the system 5.3 mm behind the sample via the micro tip and traverse a length of 880 mm from sample to detection unit. The typical timescale for this process lies in the nanosecond regime for photoelectrons with few eV of kinetic energy, as produced in the experiments of this work. Both the cylindrical tubes and the micro tip are graphitated, in order to ensure a uniform work function of the entire system.

Depending on the voltages applied to the individual lens segments, the analyzer can switch between different operating modes: Either the momentum of the electrons (angle-resolved modes) is imaged or their spatial distribution (space-resolved modes). For both cases, there is more than one operating mode, so that resolution and acceptance angle/imaged area can be altered. For space-resolved operating modes, all electrons emitted from the same spot on the sample are focused into the same spot on the detector, while in angle-resolved modes, all electrons emitted in the same angle are focused into one spot (c.f. Fig. 3.4b). When applying no voltage at all, we speak of the drift mode. Within this thesis, the space-resolved modes are exclusively used to adjust the light spot on the sample to the optical axis of the instrument while drift mode is predominantly used to determine the work function of the samples.

In contrast to other analyzers like hemispherical analyzers, the angle-resolved detection modes of THEMIS allow for simultaneous recording of k_x, k_y and kinetic energy. This can be a huge advantage if several crystal symmetry axes should be investigated at the same time (*cf.* ch. 4). However, this comes at the expense of an indirect measurement, where the quantities have to be extracted from the raw data. As will be explained in the next sections, this requires a sophisticated software that simulates the electron trajectories within the lens system. It also limits the window of kinetic energy imageable for any given set of parameters, as the transformation from the raw data to the measured quantities has to be bijective.
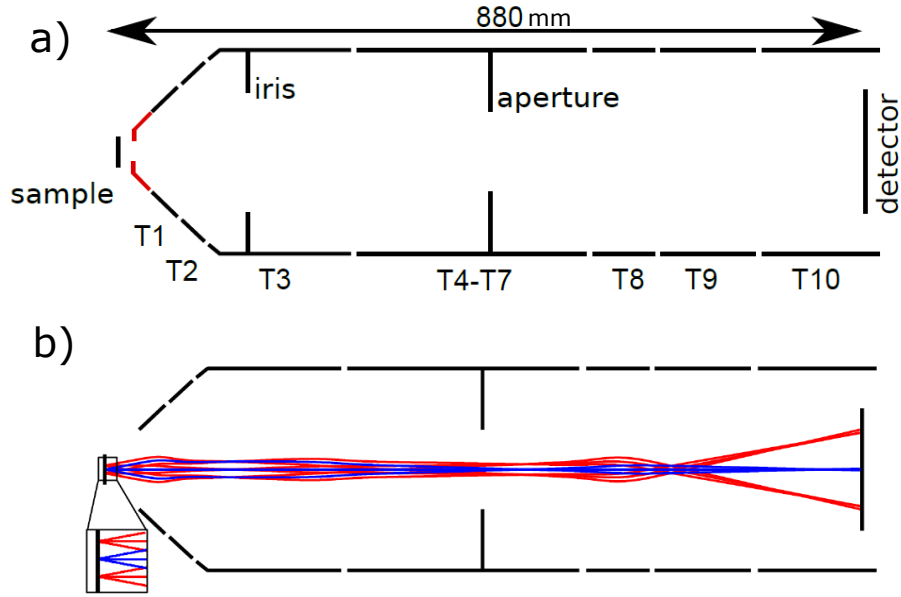
Figure 3.4: Schematic of the drift tube: a) The drift tube consists of several graphitated cylindrical segments (T1-T10), to which voltages can be applied individually. A so-called micro tip (red) is attached to the first segment to decrease the distance between sample and drift tube and therefore reduce the influence of stray fields. b) Exemplary electron trajectories in an angle-resolving detection mode: Electrons leaving the sample under the same angle but from different spots will end up at the same spot on the detector. Adapted from [174].

The width of the imageable energy window is mainly determined by the detection mode, the initial kinetic energy of the photoelectrons E_{kin} and a final energy E_{pass} of those electrons after passing the electron lens, *i.e.* their acceleration or deceleration within, which is described by the retarding ratio RR. Due to spherical and chromatic aberrations of the electronic lens system, RR is limited for each mode [99].

All 2PPE and tr-ARPES measurements presented in this thesis have been recorded in the so called Wide-angle mode (WAM), which features the highest angular acceptance of all modes, namely roughly 15°. Kinetic energies have been chosen to be centered in the area of interest and pass energies of 10 eV allowed for measurement windows of roughly 1 eV around this value at reasonable aberrations.

Detection

Photoelectrons are detected by a so called Delayline Detector (DLD) by surface concept, which is situated at the end of the electronic lens system. This detector consists of two multi-channel plates (MCPs) for the multiplication of the electrons by a factor $> 10^7$ [174] and two meandering isolated wires, called delay lines, which record the signal and transfer it to the analysis unit.
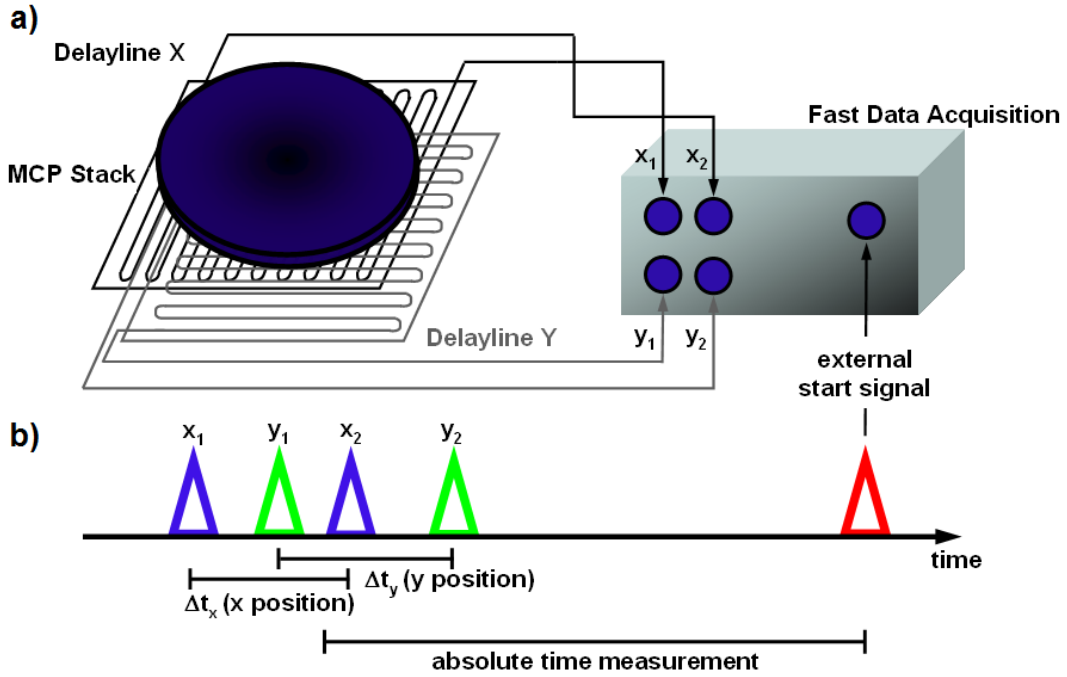
Figure 3.5: Schematic of the detector unit: a) The MCPs (blue) multiply incoming electrons, creating an electron cloud. This cloud induces a RF pulse in the meandered wire beneath. b) The relative time difference between the signals at the end of the wires serve to determine the position (x; y). Adapted from [174].

The MCPs consist of glass sheets, perforated by channels with diameters of 6 to 8 μm, which are tilted by 10° to the surface normal and coated with a semi-conducting material with very low work function. Between the first and second plate, the channels are rotated by by 90° with respect to each other (Chevron-MCP). Upon impact on the material, electrons create secondary electrons, leading to an avalanche while the electrons are accelerated from the front to the back face of the plates by a voltage of 1950 V.

After passing the MCPs, the electron cloud impacts on the delay lines, which are also rotated by 90° with respect to each other, creating electrical pulses which run to each end of the wires (*cf.* Fig. 3.5). The signals are evaluated by a time-to-digital converter (TDC): From the relative arrival times of these pulses, the position of incidence **r** is calculated. Additionally, the arrival times relative to an independent trigger signal provided by the laser pulse itself determines the time of flight t. The TDC provides the raw data in the form of a triplet (x, y, t) for each single electron count.

During the traveling time of the pulses through the wire, no second electron cloud may hit the wires, as the signals would become intertwined. Additionally, the MCPs have a recovery time of about 24 ns[174], before an electron hitting the same spot can

be multiplied. Together with the pulsed light source, this limits the countrate of the spectrometer to approximately 150.000 counts per second.[95, 99]

In contrast to *e.g.* hemispherical analyzers, all electrons emitted from the sample within the acceptance angle will be imaged onto the DLD. If there is a large background of low energy electrons, this can severely limit the possible exposure, as otherwise the maximal countrate might be overshot or, possibly even worse, the MCPs might be damaged, as with most settings, the low energy electron background will be focused on a single spot on the detector. To avoid this problem, the detector is equipped with a unit called Detector Gating Unit (DGU). This unit allows for short 10 V pulses to be applied on the nanosecond timescale to the detector. These serve for the repulsion of unwanted electrons. The timing and width of this pulse can be chosen to only affect the low energy electrons, in order not to influence the region of interest of the spectrum [99]. The DGU has been used during the measurements on BiTeI (c.f. Ch. 5).

Conversion

Obtaining the desired properties of the detected electrons - kinetic Energy E_{kin} and parallel momentum $\mathbf{k}_{||}$ or emission angle θ - from the measured quantities - time of flight t and position of impact $\mathbf{r}$ - is only analytically possible in the drift mode, *i.e.* when there are no voltages applied to the lens system. In all the other modes, the maps or functions $\mathcal{T}$ that transform the raw data to the desired parameter space,

$$(t, \mathbf{r}) \stackrel{\mathcal{T}}{\Rightarrow} \left(E_{\text{kin}}, \mathbf{k}_{||} \right) \ , \tag{3.6}$$

have to be found numerically. To this end, the electron trajectories are simulated to first find the inverse map $\mathcal{D} = \mathcal{T}^{-1}$. As mentioned before, it is therefore crucial that $\mathcal{D}$ and $\mathcal{T}$ are bijective in the region of interest.

For finding $\mathcal{D}$, first the potential landscape $\Phi(\mathbf{r})$ within the spectrometer has to be calculated. This depends on the voltage at each lens segment and the geometry of the lens system. If both are known, we can calculate the potential up to a scalar field from the charge density $\rho(\mathbf{r})$ by the Poisson equation:

$$\Delta\Phi(\mathbf{r}) = -4\pi\rho(\mathbf{r}) \tag{3.7}$$

This equation is numerically solved within the software package *Simion*. The calculation is simplified by the rotational symmetry of the setup, as it suffices to simulate a two-dimensional cut along the length of the system. However, made to the required precision, the calculation still takes hours. Therefore, we exploit the linearity of the poisson equation and the fact, that the geometry of the spectrometer is not changed: The simulation is made once for each segment, with a normalized voltage applied to the respective segment while all other segments are on ground potential. The linear combination of these solutions, all multiplied with the actual respective voltages, will

yield the correct potential for any lens mode and set of parameters. Therefore, it suffices to do the simulation once.

Now that $\Phi(\mathbf{r})$ is known, $\mathcal{T}$ can be calculated. Currently, the spectrometer is equipped with a non-commercial software written by M. Teichmann, called *hdf5plot*, which takes care of finding $\mathcal{T}$ by first computing $\mathcal{D}$: The trajectory of multiple electrons with a known initial set of parameters $\left(E_{\mathrm{kin}}, \mathbf{k}_{||}\right)$ through the electron lens is calculated by the Euler-Method (c.f. Sec. 3.3.1) to gain insight about their final parameters $(t, \mathbf{r})$. This relation then defines the transformation $\mathcal{D}$. The software predicts the energetic region, in which $\mathcal{D}$ can be inverted from the initial parameters and evaluates $\mathcal{T}$.

Once, $\mathcal{T}$ is found for a specific set of measuring parameters, it is included into a second software package by M. Teichmann, called *Themis* like the spectrometer, that simultaneously allows for the control of both the spectrometer and delay stage settings as well as handling the data acquisition. Due to limited computational resources and the non-linear relationship between raw and converted coordinates, the coordinates of each detected photoelectron are typically converted immediately and the data point is binned into a three or four dimensional histogram. Saving raw data, *i.e.* each separate count with the unconverted coordinates, was initially only possible for data sets limited to a few million counts, *i.e.* rather short exposure times. But also the resolution of the binned histograms is limited due to storage reasons, as the size increases cubic or even to the power of four with the bins per dimension. However, the resolution of the spectrometer is typically not limited by the binning but rather the laser pulse's spectral and temporal width.
We expanded *Themis* to record the converted and raw data simultaneously. This, however, requires huge amounts of storage.

T. Kunze has shown, that M. Teichmann's conversion matrices yield correct results for the case of zero voltage between the sample and spectrometer, *i.e.* if the work function difference is balanced by applying a counter voltage [100]. However, for the presented results, we chose not to balance sample and spectrometer, in order to ensure that the regions of interest in kinetic energy can be imaged properly. Unfortunately, this leads to shifts of the energy axis and slight distortions of all three coordinates. This might be due to numerical errors and/or the fact, that the micro-tip is not included in the potentials used by *hdf5plot*.

During the time of this thesis, M. Bastian implemented the software packages *SPOCK* and *SCOTTY* as an alternative for the conversion of the raw data. *SPOCK* simulates the electron trajectories with the more precise Runge-Kutta-Algorithm (c.f. Sec. 3.3.1). Fig. 3.6 shows one exemplary set of initial parameters with the corresponding simulation result. Furthermore, the micro-tip has been included in the determination of the potential landscapes used by *SPOCK*. Due to its higher precision, *SPOCK* has a much longer runtime than *hdf5plot*. Also, the determined conversion matrices cannot be used in combination with the *themis* software. Instead, data is converted from the
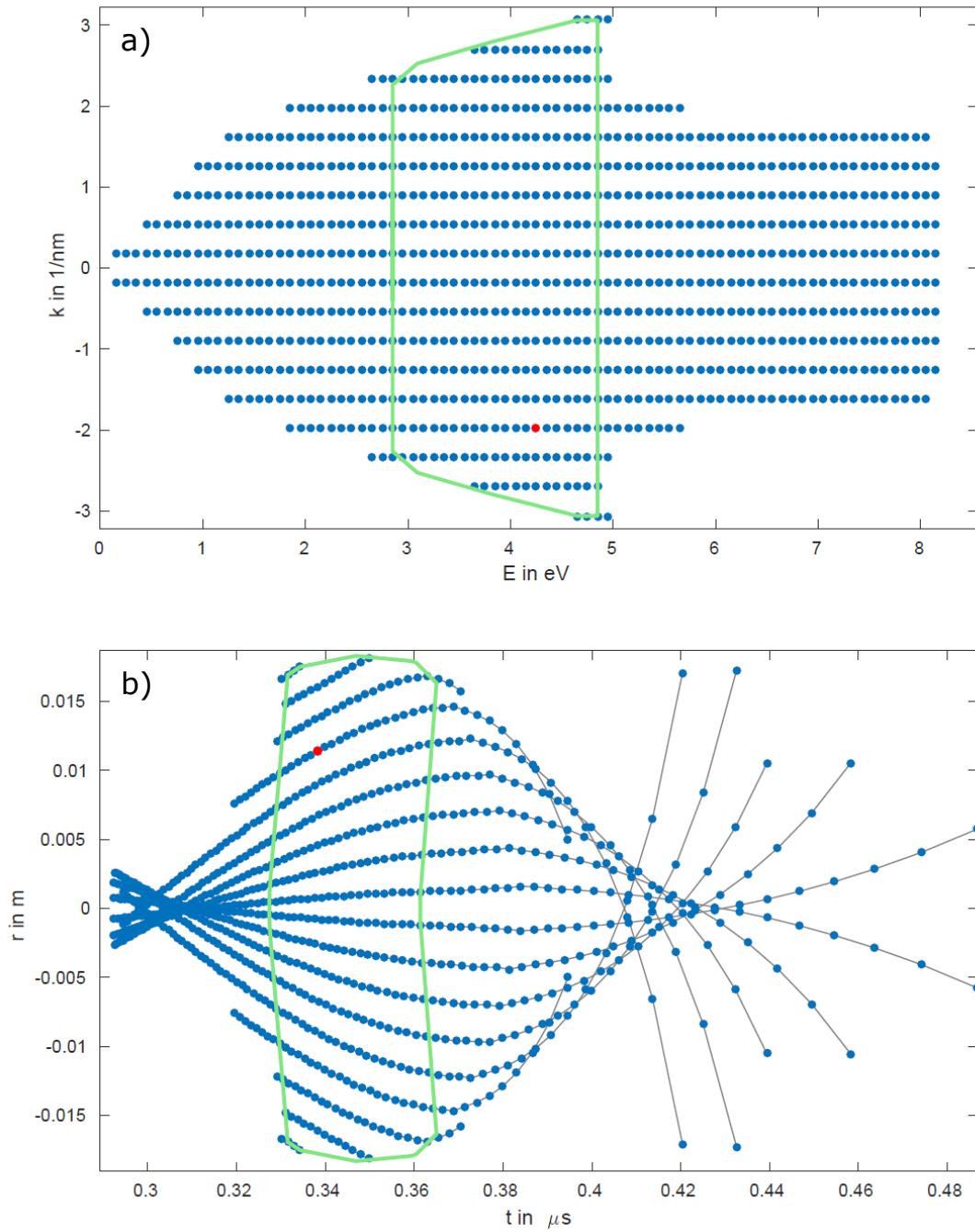
Figure 3.6: Graphical representation of an exemplary set of solutions, calculated by *SPOCK* for one set of parameters corresponding to a measurement in WAM. The green lines encompass the bijective part of the transformation. a) Initial parameters $\left(E_{\text{kin}}, \mathbf{k}_{||}\right)$ of the simulated electrons (each represented by a blue point). b) Numeric solutions $(t, \mathbf{r})$. The red point represents corresponding solution to the initial parameters marked by the red dot in a). The grey lines indicate solutions for equal initial momenta. Figures were compiled by M. Bastian [10].

separately stored raw data by the module *SCOTTY* after the measurement, which is equipped with additional features to avoid aliasing and interpolation errors.

Both software packages for determining the conversion matrix have the drawback, that the exact voltage between sample and detector has to be known a priori. This includes the work function difference between samples and detector. We typically extracted this from the low-energy cutoff in drift mode measurements, where the energy axis should simply be shifted by the voltage between sample and micro tip.

From comparing measurements of the surface states on Cu(111), converted with the original and new softwares, to literature values and drift mode measurements, we found that the software modules by M. Bastian did reduce the shift of the energy axis, most prominently by the inclusion of the micro-tip in the simulation of the potential landscape. However, the spectra still showed offsets between the different modi, whose origins could not be fully clarified. We therefore decided to rely on the more efficient original software for the measurements presented in this thesis.

We manually corrected the coordinates in the following way:
For Bi_2Se_3, we used the rather large difference in work function between sample and detector ($\approx 0.7\,eV$) as an acceleration voltage. This was nescessary, as we were interested in photoelectrons at very low kinetic energies ($< 1\,eV$). Unfortunately, this led to a rather large offset of the energy axis. We therefore referenced the kinetic energies to the low energy cutoff of the data, which should correspond to zero kinetic energy at the sample. We did not correct for the small distortion of the energy and $k_{||}$ axes, as we were not interested in the exact dispersion. Furthermore, the distortion in $k_{||}$ should be of purely radial character, therefore not influencing the symmetries of the observed patterns.
For BiTeI, the determination of a work function was futile, as the spectra showed very broadened left edges after aging (c.f. Sec. 5.1.1), which is typical for samples with contaminated heterogeneous surfaces. Here, we tried to balance detector and sample in a way to keep distortions of the spectra at a minimum. Kinetic energies in the respective chapter are as-measured, without correction. As we are mostly interested in the electron's energy with respect to the Fermi level within the sample, which could be extracted from the data directly. Most spectra are therefore given with respect to $E - E_F$.

3.2.3 Sample Preparation

As surface states and work functions are very sensitive to contamination, the surfaces of our samples and the reference copper crystal need to be prepared in UHV conditions. Even the topological surface state (TSS), which are theoretically insensitive to contaminants, will fade when the samples are too dirty.

Preparation of the Cu(111) Surface by Sputtering and Annealing

The manipulator of the vacuum chamber used for all measurements presented in this thesis is equipped with a fixedly mounted copper crystal oriented and polished to show the (111) surface. PE from the surface states of this crystal are used for the characterization of the temporal shape of the laser pulses before the measurements performed on TIs. The necessary surface states are only visible on a clean copper surface, therefore it needs to be prepared by sputtering and annealing on a regular basis.
For sputtering, the crystal is exposed to an beam of ionized argon atoms for 10 minutes at $10\,\mu A$ sputter current. Subsequently, the sample is annealed at $500\,°C$ for another 10 minutes. Herefor, the sample is heated by a direct current of 12 to $13\,A$. Unless the vacuum has been broken after the last sputtering and annealing, one cycle typically suffices for the Cu(111) crystal to show a strong signal from the surface states.

Preparation of Bi$_2$Se$_3$, Sb$_2$Te$_2$S and BiTeI by *in situ* Cleaving

All crystals investigated within the scope of this thesis, Bi$_2$Se$_3$ and BiTeI, are so called layered crystals. This means they consist of covalently bound sheets of three or five monoatomic layers, so-called quintuple layer (QL) or trilayer (TL), respectively. These two-dimensional QL/TL are bound by van-der-Waals forces to their respective neighboring sheets to form the three-dimensional structure of the crystals. The forces in the so called van-der-Waals gap between two QL/TL are obviously significantly weaker than the covalent forces within each QL/TL, and thus the crystals break easily along these gaps. Due to the difference in strength between the van-der-Waals and covalent forces, the crystal will always break between QLs/TLs. It is possible to cleave the samples under UHV conditions to obtain clean surfaces.

The initial crystals were provided by the respective collaboration partners, *i.e.* Sebastian Otto from the group of Thomas Fauster and Vladimir Voroshnin from the group of Alexander Shikin. In both cases, the samples were grown by the group of Oleg Tereshchenko.
They employ a vertical variant of the modified Bridgman method, where the elementary constituents are sealed in quartz ampules coated with a carbon layer. The ampules are introduced into a furnace with a vertical heat gradient and then slowly extracted, ensuring the progressive growth from a nucleation center.
The resulting ingots consist of one or several single-crystalline blocks. For all materials, a naturally n-doped character was reported, with carrier concentrations in the range of 10^{18} - $10^{19}\,cm^{-3}$.

We split slices of up to $1\,mm$ height from the cylindrical crystals with a razor blade. Then we cut flat and smooth pieces of typically 1 to $4\,mm$ edge length from these slices. These pieces are glued to clean molybdenum sample plates with *EPO-TEK H20E*, an epoxy-based two component conducting silver glue. This glue is hardened for one hour at $120\,°C$.
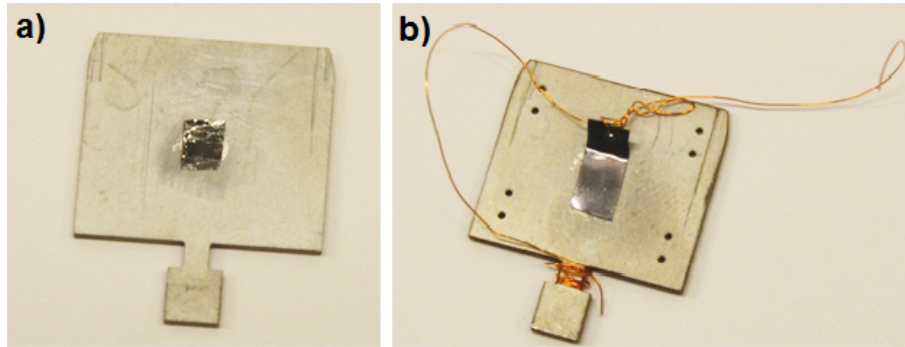
Figure 3.7: Typical samples: a) A Bi$_2$Se$_3$ sample glued on top of a molybdenum plate with conducting epoxy glue. b) A sample equipped with a cleaving mechanism, ready for insertion into the vacuum chamber. The bend tantalum foil can be glued on with epoxy glue or UHV-safe double sided tape. Before measurement, it will be torn off the sample, taking a few layers with it. The optional copper wire prevents the tantalum foil from falling into the vacuum chamber after the cleaving process.

The samples were then equipped with a cleaving mechanism before being transferred into the UHV chamber. The actual cleaving mechanism looks slightly different on the two sample types: For Bi$_2$Se$_3$, we use pieces of 0.5 mm thick tantalum foil, which are slightly wider and a bit more than twice as long than the samples. About 1 mm from one of the shorter edges, we drive a hole of about 0.5 mm diameter through the tantalum foil. Then the foil is bent into an angle of $\approx 90°$. In doing this we exercise care that the part without the hole stays as planar as possible, as this part is glued on top of the sample. Here we either use the same conducting silver glue as before or double-sided graphite-based UHV tape. The perforated part of the foil points upwards from the sample plate. To be able to retrieve the cleaving angles after the cleaving process, we can thread a thin copper wire through the hole and fasten it there and on the molybdenum holder (*cf.* Fig. 3.7).

For cleaving BiTeI, a strip of one-sided stiff UHV-safe tape is stuck on top of the sample with one end standing over and sticking up. This end is wound around a small wire ring.

The prepared samples are either directly inserted into the vacuum chamber and stored in the inbuilt sample garage or stored outside the chamber in an desiccator to keep them water and dust free.

Within the chamber, the samples are cleaved at 2×10^{-9} mbar and transferred to our PE chamber with a base pressure of 6×10^{-11} mbar as fast as possible, typically within less than 2 minutes.

For the cleaving the TIs in the vacuum chamber, we drive the up pointing part of the tantalum foil against a little screw on the sample garage, breaking it off the crystal. In the case of BiTeI, we hook the wire ring onto the screw and pull off the tape. The tantalum foil or tape exfoliates several layers of crystal. If applied, the copper wire then

prevents the tantalum foil from falling into the chamber, so that it can be extracted from the chamber together with the sample after the measurement. To avoid disturbance of the measurements, we ensure that the tantalum foil on the copper wire is hanging well away from the sample, the incoming and reflected laser beams and the trajectory of the analyzed photoelectrons.

To control sample orientation and surface order, the vacuum chamber is equipped with a low-energy electron diffraction (LEED) setup.

Within the PE chamber, Bi_2Se_3 samples were kept at 100 K throughout the entire measurement. No change of Fermi level position was observed on the sample, in contrast to previous studies [11, 17].
BiTeI samples were both investigated at room temperature (≈ 300 K) and cooled with liquid Helium (sample temperature ≈ 60 K) respectively.

Samples of sufficient thickness with smooth surfaces, *i.e.* samples with no glue residues and more or less smooth surfaces can be reused by extracting the samples and equipping them with a new cleaving mechanism.

3.3 Theoretical Calculations and Models

Often, the key to understanding complex physical processes lies in a combination of experimental results and theoretical calculations. This is also the case for the studies presented in this thesis. In this section, I will provide a short insight into the employed theoretical models. As the theoretical part is, however, not a main focus of this thesis and heavily relies on the work of others, this shall only serve as a short information, not a detailed description. The interested reader shall be referred to the works of the corresponding collaboration partners and coworkers, which served as guidelines to this section.

3.3.1 Simulation of Electron Trajectories

As we have seen in Sec. 3.2.2, the conversion of the raw data as gathered by our spectrometer requires the numerical simulation of electron trajectories through the lens system of the detector. For this, we have access to two different custom computer programs, *hdf5plot* implemented by M. Teichmann and described by T. Kunze [100], and *SPOCK* implemented and described by M. Bastian [10]. These programs use the Euler method and Runge-Kutta method for the numerical integration of the equations of motion, respectively.

Both methods aim at solving a differential equation of the form

$$y'(x) = f\left(x, y(x)\right) \tag{3.8}$$

and given initial value $y(x_0)$ by iterating the solution over a grid of values x_n.
We will quickly introduce both methods, but refer the interested reader to a book about numerical mathematics, *e.g.* by Zulehner [191].

Both methods are introduced for a first order differential equation. However, the electrons' equation of motion

$$\ddot{\mathbf{r}} = -\frac{q}{m}\nabla\phi(\mathbf{r}) \tag{3.9}$$

is of second order. However, both algorithms can be adapted for second order [100, 191], which is accordingly done.

Euler Method

The Euler method for numerically solving differential equations of the shape of Eq. 3.8 is very straightforward and the basis for many more complex methods, like the Runge-Kutta method.

Typically, one divides the x-range over which one wants to solve the differential equation into an equidistant grid with step size h, so that $x_n = x_0 + nh$. When the initial value or boundary condition $y(x_0)$ is given, we can recursively iterate the solution via the Taylor expansion in h and by using the relation 3.8:

$$\begin{aligned} y\left(x_{n+1}\right) = y\left(x_n + h\right) &= y\left(x_n\right) + h \cdot y'\left(x_n\right) + o(h^2) \tag{3.10}\\ &\approx y\left(x_n\right) + h \cdot f\left(x_n, y(x_n)\right) \ . \tag{3.11} \end{aligned}$$

Geometrically speaking, this corresponds to an extrapolation of the function by the tangent. The error of the Euler method depends linearly on the number of steps the interval is divided by.

Runge-Kutta Method

The Runge-Kutta method expands on the Euler method by evaluating the tangent at several points in the interval $[x_n, x_{n+1}]$.
More precisely, the algorithm aims at solving the following integral form:

$$y\left(x_{n+1}\right) = y\left(x_n\right) + \int_{x_n}^{x_n+h} f\left(x, y(x)\right)\mathrm{d}x \tag{3.12}$$

by approximating with the quadrature formula

$$\int_{x_n}^{x_n+h} f\left(x_n, y(x_n)\right)\mathrm{d}x \approx h\sum_{i=1}^{s} b_i f\left(x_i, y(x_i)\right) \ , \tag{3.13}$$

where $x_i = x_n + c_i h$ with $c_i \in [0, 1]$ and $\sum_{i=1}^{s} b_i = 1$.

By this, the problem of unknown $y(x_n)$ has been shifted to unknown $y(x_i)$. To calculate those, we can use the same approximation of Eq. 3.12 and Eq. 3.13 again, but on the smaller intervals $[x_n, x_n + c_i h]$:

$$y\left(x_n + c_i h\right) \quad = \quad y\left(x_n\right) + \int_{x_n}^{x_n + c_i h} f\left(x, y(x)\right) \mathrm{d}x \tag{3.14}$$

$$\approx \quad y\left(x_n\right) + h \sum_{k=1}^{s} a_{ik} f\left(x_k, y(x_n + c_k h)\right) \; . \tag{3.15}$$

Again, we have only shifted the problem to smaller intervals.

Now, the values $y(x_n + c_k h)$ are approximated according to the Euler method, which is called *explicit Runge-Kutta method*. The choice of the number of steps s, and the coefficients a_{ik}, b_i and c_k then determines the properties of the method. In *SCOTTY*, a standard fourth-order Runge-Kutta method is chosen [191, Ch. 4.4].

The error of this method inversely depends on the number of points to the power of four.

3.3.2 One-Step Photoemission Calculations

As we will see in Ch. 4, it is crucial to understand the contributions of the different involved electronic states in order to relate our PE spectra to direct measurements of photocurrents on Bi_2Se_3. To that aim, our collaborators J. Braun and J. Minar calculated the theoretical PE intensities between the initial state and final states by determining the corresponding transition matrix elements in the so-called one-step model.

In order to determine these matrix elements, J. Braun and J. Minar first calculated the self-consistent electronic structure of Bi_2Se_3 within the *ab-initio* framework of spin-density functional theory. *"The Vosko, Wilk, and Nusair parameterization for the exchange and correlation potential was used [178]. The electronic structure was calculated in a fully relativistic mode by solving the corresponding Dirac equation using the relativistic multiple-scattering formalism in the TB-KKR mode [41, 42]."*[24] This calculation was performed on a half-space of Bi_2Se_3, as the resulting electronic structure then served as input for one-step photoemission calculations. To that end, the electronic structure was *"represented by single-site scattering matrices for the different layers and the corresponding wave functions for initial and final-state energies".*[24] To obtain the correct description of the energetics and dispersion of all surface-related features, a Rundgren-Malmström-type surface potential [110] was included into the formalism as an additional layer and the relative intensities of surface states and resonances are quantitatively accounted for by calculating the corresponding matrix elements in the surface region [129].

In line with scattering theory, the initial state is then represented by an energy-dependent retarded KKR Green function. A complex value for the energy is used, with a constant imaginary part $V_i(E) = 0.004$ eV, to account for damping effects due to inelastic scattering events and therefore the finite lifetime of the initial state.

The final states are represented by so called inverse LEED states, which are wave functions that correspond to the crystal electronic states within that *"Also in the final-state calculation many-body effects have been included phenomenologically by use of a parameterized, weakly energy-dependent and complex inner potential $V_0(E_f) = V_{0r}(E_f) + iV_{0i}(E_f)$ [70, 136]."*[24]

Chapter 4

On the Origin of Helicity-Dependent Photocurrents in Bi$_2$Se$_3$

*Parts of this chapter have already been published in the author's work "Origin of spin-polarized photocurrents in the topological surface states of Bi$_2$Se$_3$" in Phys. Rev. B **98**, 155406 (2018) [I].*

Bi$_2$Se$_3$ is one of the most commonly studied topological insulators (TIs) [64]. It features two topological surface states (TSSs) at the $\overline{\Gamma}$-Point of its (0001)-surface Brillouin zone (BZ) [125, 127]. As most TIs, Bi$_2$Se$_3$ is intrinsically doped by defects in its crystal structure. As a consequence, one of its TSSs is occupied with the Dirac point (DP) at a binding energy of a few dozen meV, the second TSS is unoccupied and lies approximately 1.7 eV above the occupied one [125, 126]. In Sec. 4.1, the band structure of Bi$_2$Se$_3$ is presented in more detail.

Bi$_2$Se$_3$, along with related TIs, was a likely candidate for the generation of spin-polarized currents. It has sparked even more interest, since McIver et. al. claimed they could excite spin-polarized photocurrents by irradiating the material with circularly polarized pulses of near-infrared light [112]. So far, the observation of photocurrents could be reproduced several times with different detection methods and excitation energies [25, 83, 132]. However, the origin of these photocurrents could not be conclusively clarified and their spin-polarized character remains disputed. Sec. 4.2 summarizes these previous works on photocurrents in Bi$_2$Se$_3$.

I want to address the question of the origin of these photocurrents by directly observing the excited electrons in momentum space. The most common assumption is, that the currents are excited with the participation of the TSSs of the material (*cf.* Sec. 4.2). Due to the spin-polarized character of these states, a current carried by the TSS would also be spin polarized, which would be very convenient for spintronic applications. A current carried by the surface projected bulk bands, in contrast, is not *a priori* spin polarized. A non-zero current manifests as an asymmetric distribution of excited carriers, which should be observable in two-photon photoemission (2PPE). In line with previous experiments on photocurrents, we excited the carriers with circularly polarized near-infrared (nIR) light and then photoemitted the excited carriers from the unoccupied TSS and the surrounding bulk bands (*cf.* Sec. 3.2.1 for the creation of the laser pulses). Their momentum distribution was determined with an angle-resolved time-of-flight (ToF) spectrometer, which allows access to all carriers emitted within a cone with an opening angle of $\pm 15°$ (*cf.* Sec. 3.2.2). Due to the strong spin-orbit interactions in

Bi_2Se_3, the resulting transition probabilities are influenced by a multitude of factors. Therefore, the spatial distribution of the photoelectron signals has to be interpreted carefully and the right photon energies and polarizations have to be chosen for selecting specific processes. Previous and own work on this issue is presented in Sec. 4.3.

I chose to compare data obtained from samples excited either resonantly between the TSSs or off-resonantly with 1.7 eV and 1.9 eV photon energy respectively. For the second pulse, near-ultraviolet s-polarized light of 4.7 eV photon energy was chosen in order to reach final states with an s-like character. In addition, the measurements were compared to one-step photoemission calculations. Hereby, the symmetry of the excitation process can be determined and compared to the expectations. I present the results and their discussion in Sec. 4.4.

Additional insight can be obtained by looking at the temporal evolution of the distribution of excited carriers. The corresponding results are presented and discussed in Sec. 4.5.

4.1 Bi_2Se_3 - Drosophila of TIs

As explained in Sec. 2.3, the term "topological insulator" refers to a class of materials with a peculiar band structure that leads to metallic surface states on an insulating bulk, the so-called topological surface state (TSS). On most 3D TI, these surface states take the form of spin-polarized surface states with almost linear dispersion and a crossing point within or close to a bulk band gap, and are therefore often referred to as Dirac cone (DC). While this class of materials has been first theoretically predicted, Bi_2Se_3 is one of the first 3D materials where these properties were actually observed, which led to Bi_2Se_3 being one of the most studied TIs in general [64, 118]. Unsurprisingly, Bi_2Se_3 was also the first TI, on which helicity dependent photocurrents were reported (*cf.* Sec. 4.2).

As most 3D TIs, Bi_2Se_3 has a layered crystal structure. In this specific case, five alternating layers of Bismuth and Selenium form a covalently bond so-called quintuple layer (QL). These QLs then stack via Van-der-Waals forces to form the 3D crystal structure of Bi_2Se_3 (*cf.* Fig. 4.1b). Cleaving Bi_2Se_3 along the Van-der-Waals planes is very easy (*cf.* Sec. 3.2.3) and will always expose a Se-terminated surface. Each of the monoatomic layers of Bi_2Se_3 shows six-fold rotational symmetry, while the entire crystal structure is threefold symmetric due to the stacking within each QLs being hexagonally close packed. The unit cell spans three QLs to account for the stacking symmetry of the QLs.

Due to the heavy elements it constitutes of, Bi_2Se_3 features strong spin-orbit coupling, which leads to an inverted primary band gap and therefore to a topologically non-trivial band structure (*cf.* Sec. 2.3). DFT calculations of the band structure indicate that a DC spans this band gap at the Γ-point, the DP being situated within the band gap
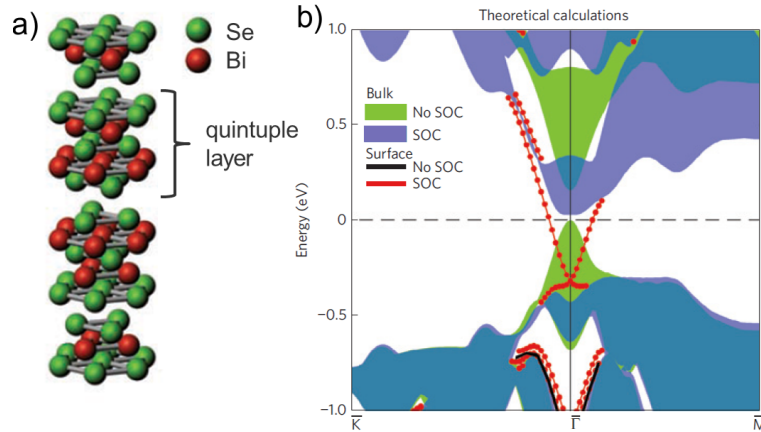
Figure 4.1: a) Crystal structure of Bi_2Se_3, adapted from [31]. b) DFT calculations of the surface projected band structure of Bi_2Se_3. Shaded areas correspond to bulk bands, dotted lines to surface states. It becomes evident that the inclusion of SOC (purple areas, red lines) significantly changes the appearance of the band gap (green areas indicate the bulk bands calculated without SOC, in blue areas both calculations overlap) and leads to the emergence of the DCs. Figure adapted from [187].

(*cf.* Fig. 4.1b). This stands in contrast to the closely related Bi_2Te_3, where the DP lies below the valence band maximum (VBM), albeit at a different momentum [74]. Additionally, it was predicted that hexagonal warping is relatively weak in Bi_2Se_3 (for an explanation of hexagonal warping, *cf.* Sec. 2.3.3).

Bi_2Se_3 is intrinsically n-doped to the point of being a degenerate semiconductor, *i.e.* the Fermi level lies closely above the conduction band minimum (CBM) and the first TSS is fully occupied. In consequence, the occupied TSS and the relatively large band gap of ca. 0.3 eV made Bi_2Se_3 ideal for photoemission spectroscopy (PES) studies of the surface electronic structure. A calculation of the spectral function, *i.e.* the band structure as it should appear in PES, of Bi_2Se_3 is depicted in Fig. 4.2a). Photoelectron (PE) measurements of the electronic structure of Bi_2Se_3 generally confirmed the theoretical predictions [74, 75, 79, 159, 164, 187].

The intrinsic n-doping of the material is created by Se-vacancies generated in the bulk crystal during growth. As the intrinsic doping is strong enough to make Bi_2Se_3 a degenerated semi-conductor or half-metal, it leads to significant bulk conductivity, posing a serious challenge to the measurement of surface currents with conventional transport techniques [26]. To our knowledge, it is not possible to grow pristine Bi_2Se_3 with the Fermi level situated within the band gap.

Niesner *et al.* have shown that Bi_2Se_3 exhibits a second unoccupied TSS between the 2nd and 3rd conduction band, 1.7 eV above the occupied TSS [125, 126]. This finding has been confirmed by theoretical density functional theory (DFT) calculations and later reproduced experimentally by Sobota *et al.* [167]. Hence, photoexciting carriers from
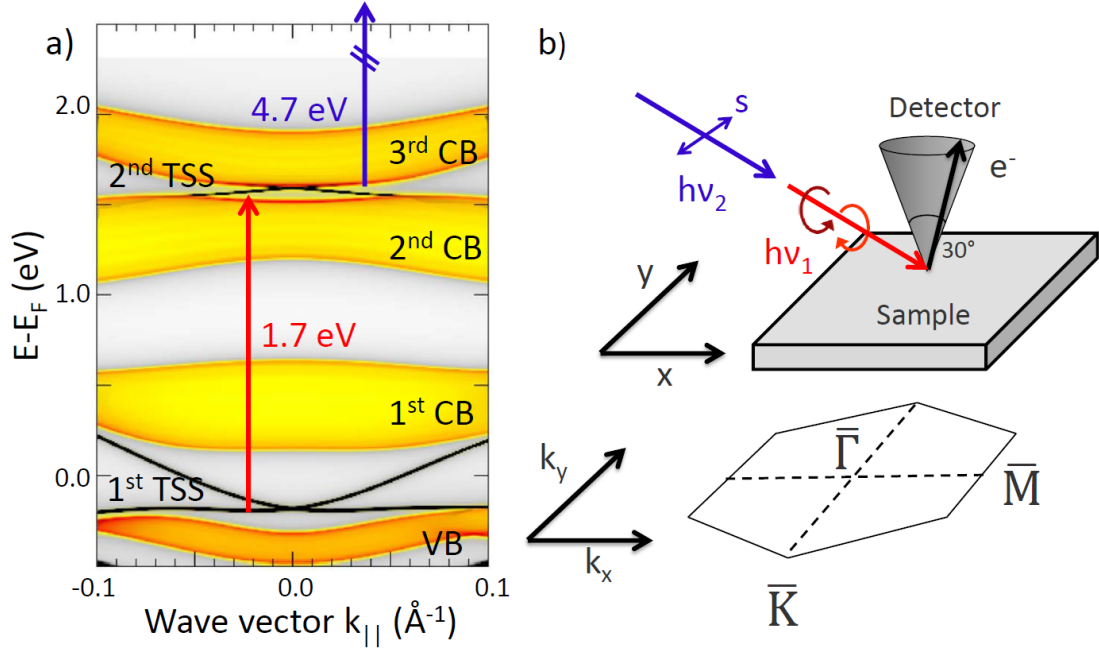
Figure 4.2: a) Spectral function of Bi$_2$Se$_3$ calculated with DFT by J. Minar. The first and second TSSs are separated by $\sim$ 1.7 eV. The red arrow indicates interband transitions for resonant excitation. b) Experimental geometry: The laser beams are oriented so that the in-plane component is parallel to the $\overline{\Gamma\text{M}}$-direction at an angle of incidence of 45°. Photoelectrons are detected in a cone around the surface normal with 30° opening angle by an angle-resolving ToF spectrometer.

the occupied to the unoccupied TSS (*cf.* Fig. 4.2a) constitutes a promising approach to drive spin-polarized photocurrents relatively insensitive to details of the bulk doping and concomitant Fermi-level position, as compared to, *e.g.*, intraband excitation.

Fig. 4.3 shows the photoemission intensity obtained from the energetic region of the second TSS after excitation with unpolarized pulses of 1.7 eV photon energy. The probe pulses with a photon energy of 4.7 eV were obtained by third-harmonic generation (THG) of the titanium sapphire (Ti:Sa) fundamental (*cf.* Sec 3.2.1). This photon energy is not sufficient to overcome the Bi$_2$Se$_3$ work function of 5.6 eV, but enough to fully access the unoccupied TSS. Both pulses were incident on the sample in the plane spanned by the surface normal and the $\overline{\Gamma\text{M}}$-direction of the surface BZ and have a cross correlation of 80 fs.

Upon excitation with unpolarized pulses of 1.7 eV photon energy and probing with s-polarized pulses of 4.7 eV photon energy, the 2PPE intensity maps show the signature of a single DC, *cf.* Fig. 4.3a). Note that the signal from the lower DC is overlapped with the intense signal from the valence band (VB) and/or second conduction band (CB) while the upper DC is clearly resolved. This is in contrast to the calculations of the spectral function presented in Fig. 4.1. This might be due to the signal being

dominated by the initial state dispersion, where the DP lies much closer to the VB than the CB. However, getting exact band structures from DFT, especially for unoccupied states and around band gaps is very challenging [2, 3, 113], so that the calculated spectral function might also slightly deviate from the actual band structure. In either case the spectral bandwidth of the probe pulse, a direct consequence of the temporal resolution, limits our energy resolution and therefore blurs the bands together, even if they are well separated.

As only one DC is discernible in the spectra recorded with 1.7 eV exitation energy, while off-resonant excitation with 1.9 eV reveals both TSSs (*cf.* Sec. 4.3 and Fig. 4.8a) we can support the assumption that resonant excitation between the two topological surface states is possible at 1.7 eV photon energy.

The cut through the upper branches of the TSS is fairly isotropic, but shows a small threefold modulation of the 2PPE intensity, which is a signature of a weak warping, which influences the matrix elements (*cf.* Sec. 2.3.3 and Fig. 4.3b). This warping is also perceivable in the calculations for direct photoemission with 4.7 eV photon energy from the second DC (Fig. 4.3c). The calculations assume an isotropic population of the 2nd TSS and thereby suggest that the s-polarized probe pulses accurately image the population of the intermediate state and therefore do not influence the circular dirchoism in the angular distribution (CDAD) patterns obtained with circularly polarized pump pulses. This issue is further discussed in Sec. 4.3.

Additionally to the signature of the TSS, a strong 2PPE signal is obtained for transitions from the VB to the 2nd CB, as already mentioned, and a much weaker signal at a kinetic energy around 0.9 eV for excitations from the occupied part of the 1st CB into the 3rd CB.

An additional feature of the spectrum presented in Fig. 4.3b) is a weak parabolic band with the band bottom appearing at approximately 0.9 eV kinetic energy. This feature corresponds to the image-potential state of Bi$_2$Se$_3$ [167]. Image-potential states are surface states found on most surfaces, and correspond to an electron being bound in front of the surface by its image charge (for more detail on image-potential states, *cf. e.g.* [43]). Energetically, these states lie close below the vacuum level, *i.e.* in a very different energy range as the states we are interested in. The image-potential state appears at similar kinetic energies as the TSSs, as it is populated by the 4.7 eV pulse and then photoemitted by the 1.7 eV pulse. It bears, however, no dichroic signal and cannot influence the dynamics significantly due to the energetic separation, and therefore it can be neglected in all the upcoming discussions.

4.2 Previous Experiments on Photocurrents in Bi$_2$Se$_3$

Photocurrents can in principle be created by illuminating a sample with light of arbitrary wavelength and polarization. Due to symmetry arguments, an excitation of photocurrents in the bulk of Bi$_2$Se$_3$ is forbidden and only allowed at the surface due
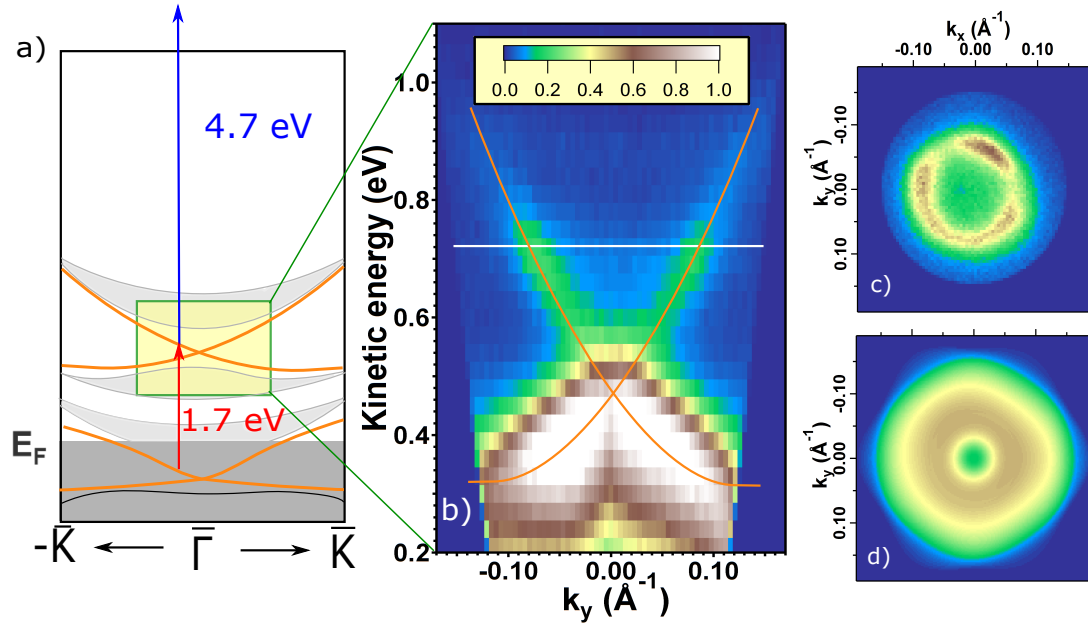
Figure 4.3: a) Excitation scheme for resonant excitation with 1.7 eV photon energy and probing with s-polarized light with 4.7 eV photon energy in Bi$_2$Se$_3$. b) Photoelectron intensity along $\overline{\Gamma K}$ for excitation by both *rcp* and *lcp* light and s-polarized probe pulses. c) The map of the full angular distribution at 0.76 eV kinetic energy (energy indicated by the white bar in b) reveals a nearly isotropic photoelectron intensity. d) The calculated PE spectrum with 4.7 eV photon energy assumes an isotropic electron distribution at 190 meV above the unoccupied Dirac point. The s-polarized probe pulses lead to isotropic PE and therefore do not alter the CDAD maps shown in Fig. 4.7 and following.

to the breaking of inversion symmetry. However, due to the possible involvement of surface projected bulk bands, currents excited on the surface of the material are not *a priori* spin polarized. There have been many studies in the recent years trying to create photocurrents specifically in the TSS of Bi$_2$Se$_3$, as these would be spin-polarized due to the spin-orbit coupling (*cf.* Sec. 2.3). In 2011, Hosur proposed to excite the samples with circularly polarized light, because his calculations on a model system suggested that the photon angular momentum couples to the parallel component of the electron spin.

McIver and coworkers were the first to report helicity-dependent photocurrents on Bi$_2$Se$_3$ [112] in line with Hosur's predictions. In their experiments, they equipped a flake of Bi$_2$Se$_3$ with strip contacts and illuminated the sample with near-infrared laser pulses. Apart from significant helicity-independent photocurrents, they observed a helicity-dependent component. This component, however was only excited under a specific geometry, namely oblique incidence parallel to the strip contacts. For normal incidence and oblique incidence perpendicular to the contacts, no helicity-dependence was observed. In line with theoretical predictions [72], these currents were assigned to

originate from the TSSs.

By theoretically studying a model system, Junck *et al.* tried to determine the origin of the currents observed by McIver *et al.*. They found that the photogalvanic current is strongly suppressed within the TSS of Bi_2Se_3, and concluded, that helicity dependent currents can only be created if there is an interaction with bulk bands [80].

In 2014, Kastl *et al.* studied the temporal development of the photocurrents on Bi_2Se_3 flakes via an Auston-switch setup [83]. From their data, they concluded that the currents excited by circularly polarized light rise right after the excitation and prevail for approximately 4 ps. In addition, the velocity of the carriers corresponds roughly to the Fermi velocity of Bi_2Se_3. As the excitation mechanism, Kastl *et al.* also propose the coupling of the light to the helical spin texture of the TSS.

Another study indicating that the currents stem from carriers at the Fermi level was published in 2017 by Pan *et al.* [133]. They show that the helicity dependent currents are sensitive to the position of the Fermi level in compounds of the family $(Bi_{1-x}Sb_x)_2Te_3$. $(Bi_{1-x}Sb_x)_2Te_3$ exhibits a Fermi level within the bulk band gap, as intrinsic p- and n-type doping compensate. Therefore it can be gated. When grown in bulk, however, the stoichiometry will vary spatially, leading to inhomogeneous doping and local charge puddles, which strongly influence the transport properties of the respective TIs [22, 154].

In order to look directly at currents stemming from the Fermi level, the group of S. Ganichev used terahertz (THz) radiation for the excitation of photocurrents on different TIs [132, 139–141]. This type of radiation has very low photon energies and therefore only excites the carriers directly around the Fermi edge. They find that linear photogalvanic and photon drag effects strongly outweigh the circular effects. They attribute the measured currents mainly to anisotropic scattering of the excited carriers from the threefold symmetric surface potential.

Another way to probe currents with THz radiation, other than the transport measurements introduced so far, is to look at the THz radiation emitted by the electrons in motion. This method, combined with near-IR excitation was applied by L. Braun *et al.*, who also found mainly a linear photogalvanic effect. They attributed their signal to charge shifts of the electrons along the Se-Bi bonds. [25]

The latter results and the theoretical study question the spin-polarized character of the photocurrents, as the bulk states are not *a priori* spin-polarized and therefore the involvement of the surface projected bulk states in the currents might strongly affect the net spin-polarization. In addition to that possible involvement, Bi_2Se_3 is a known thermoelectric material. Even though the experiments described above do their best to minimize contributions to the currents that result from the heating of the material by the exciting laser pulses, small experimental inaccuracies can never be fully excluded.

In the following sections, I will introduce CDAD as a method to look directly into the TSS and CB of Bi_2Se_3 in order to determine their contribution to the photocurrents.

However, there is one contribution that might be involved in the measurements presented above which I cannot directly study: As many of the transport measurements have been performed under ambient conditions, not only the partially occupied bulk bands might contribute to the observed currents. It has been observed that Bi$_2$Se$_3$ undergoes strong surface band bending when exposed even to residual gases under UHV conditions. Within the resulting potential well, Rashba states might appear that could contibute to the observed photocurrents [8, 11, 86]. As the results presented in the following were obtained on samples under UHV conditions that did not show a surface band bending, this possible contribution cannot be observed.

4.3 Circular Dichroism on Topological Insulators

As the spin texture of the TSSs in TIs is one of their most characteristic properties, a lot of work has been put into measuring it with spin-resolved PES [30, 170] and - more indirectly - with circular dichroism [125, 180, 181]. The latter tries to exploit the fact, that the probability of electrons coupling to a photon depends on the relative orientation of the electron's spin and the photon's angular momentum. CDAD patterns are obtained by subtracting individual maps excited with either right circularly polarized light (*rcp*) or left circularly polarized light (*lcp*) normalized to the combined photoelectron intensity. Typically, the contrast in these photoelectron maps is assumed to directly map the spin structure of the initial state.

However, thorough investigation has shown that due to the strong spin-orbit coupling in TIs, the photoelectron spin is not necessarily conserved during PE. And also the CDAD from TIs stems from the complicated interplay between the spin and orbital symmetries of the involved initial, intermediate, and final states [159], *i.e.* it depends strongly on, *e.g.* the orbital symmetry properties of all electronic states involved in the transition [77, 79, 134, 135, 156, 158, 159, 185, 188, 189], *i.e.* not only the spin initial state.

4.3.1 Influence of the Probing Step

As we want to observe the interaction of the incoming circularly polarized light with the system, we have to exclude any influence of the probing step on the patterns. Previous studies have shown that the final states for our excitation energy, which combines to 6.4 eV photon energy, have s-like character, so their influence on the circular dichroism should be minimal [77, 135, 159, 189]. However, we found that the recorded CDAD patterns depend strongly on the polarization of the probe pulses: The patterns above the DP look anti-symmetric when recorded with p-polarized pulses (*cf.* Fig 4.4, upper row), as assumed by McIver *et al.*[112], but rotated by about 45° from the expected orientation. However, they look threefold symmetric when recorded with s-polarized probe pulses. The patterns in the TSS below the DP look threefold symmetric for both s- and p-polarized probe pulses (*cf.* Fig 4.4, lower row), possibly induced by the valence
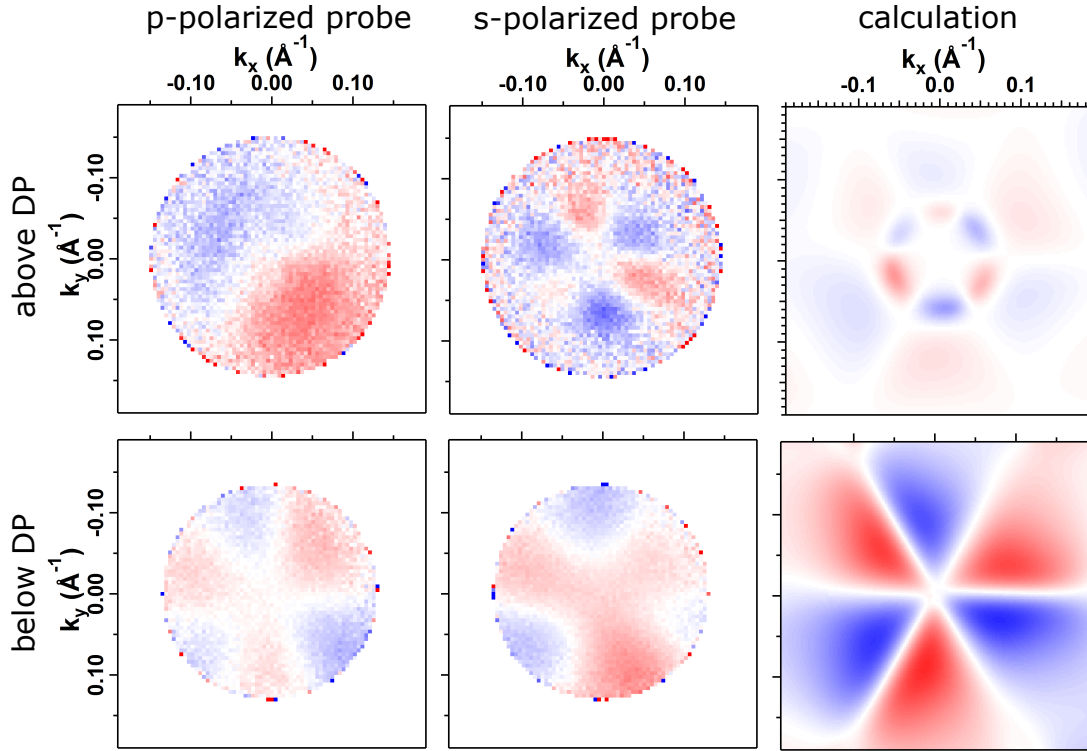
Figure 4.4: CDAD patterns above (top row) and below (bottom row) the DP. The first and second column show data measured on the same Bi_2Se_3 sample upon circular excitation with 1.7 eV photon energy. The spectra in the first column were recorded with p-polarized probe pulses and the spectra in the second column with s-polarized probe pulses (both cases: 4.7 eV photon energy). The third column shows the calculated patterns for the case of direct PE from the occupuied DC with circularly polarized light of the combined photon energy (6.4 eV).

band symmetry. While this pattern does not look perfectly symmetric in both cases, the asymmetry between positive and negative k_x values (the direction in which symmetry is broken by the incoming light) seems to be more prominent in the images recorded with p-polarized pulses.

To gauge the general influence of the probing step and identify the origin of the CDAD patterns, we compare our results to one-step PE calculations provided by our collaboration partners J. Braun and J. Minár (*cf.* Sec. 3.3.2). These were done for direct photoemission with circular polarized light with the photon energy of 6.4 eV. This corresponds to the sum of pump and probe pulse energies and therefore a direct transition from initial to final states. The obtained theoretical predictions for CDAD patterns are shown in the third column of Fig. 4.4. We find very good agreement for PE from the lower and upper TSS when recorded with s-polarized probe pulses. This indicates, that the out-of-plane component of the p-polarized probe pulses distorts the transition matrix elements from the intermediate state to the final state. While the exact mechanism

is not understood and cannot - so far - be reproduced by theory, it is reminiscent of the linear dichroism that was observed when photoemitting electrons from both occupied and unoccupied TSSs on various TIs [100, 107, 125, 151, 190]. It might result from the interaction during the photoemission process of the electrons stemming from different layers of the crystal, as described by Zhu *et al.* [190], but might alternatively be a signature of an actual asymmetric excitation process [107]. In any case, it highlights that photoemission from the TSSs is not as straightforward as one might first assume and that other effects, besides the helical spin texture of the DC, can play a significant role in the process.

In contrast to the involved spectra recorded with p-polarized light, comparison between the spectra and the one-step calculation indicates that in the case of s-polarized probe pulses, the symmetry of the intermediate state does not play a significant role. We were able to further corroborate this finding by switching to circular polarized probe pulses (see below) as well as through the investigation of off-resonant excitation and time-dependence of the patterns (presented in sections 4.4 and 4.5, respectively). All in all, this supports our hypothesis that the recorded CDAD patterns presented in those sections reflect the coupling of the circularly polarized photons to the initial state, *i.e.* the occupied TSS.

As already stated, a further test to investigate the coupling of the light to the involved states is to switch to linearly polarized pump and circularly polarized probe pulses.
It has been shown that p-polarized light couples significantly better to the TSS of Bi- and Sb-derived 3D TIs [100], so we chose p-polarized pump pulses to increase the signal intensity. However, this might lead to the previously mentioned linear dichroism, exciting predominantly one branch of the TSS.[100, 107, 125, 151] To disentangle signatures from occupied and unoccupied TSS, we go for off-resonant excitation, *i.e.* 1.9 eV photon energy.

As can be seen from Fig. 4.5, the dichroic signature mainly appears in the energy range to which the electrons from the occupied states are excited to. In the upper branches of the occupied TSS (Fig. 4.5b), a very peculiar pattern can be found: There is only a dichroism at positive k_x values, which is anti-symmetric in the k_y direction. The asymmetry in k_x could possibly be described by the linear dichroism of the pump pulse, while the anti-symmetric pattern in the k_y direction is expected from the predictions of Park *et al.* [135], if the excitation process preserves the spin polarization. However, the latter is probably not the case, as shown by Sánches-Barriga *et al.* [159]. In addition, one might expect an anti-symmetric dichroic signature from the unoccuied TSS, if the model of Park *et al.* [135] holds up, which is clearly not the case here. On the contrary, there seems to be no signature from the unoccupied TSS at all. The lower branch of the occupied TSS (Fig. 4.5c, energetically also the region of the upper unoccupied branch) shows no clear pattern. As only half of the signature is visible due to the linear dichroism, the observed structures can alternatively be two- or threefold symmetric, or distorted anti-symmetric patterns.

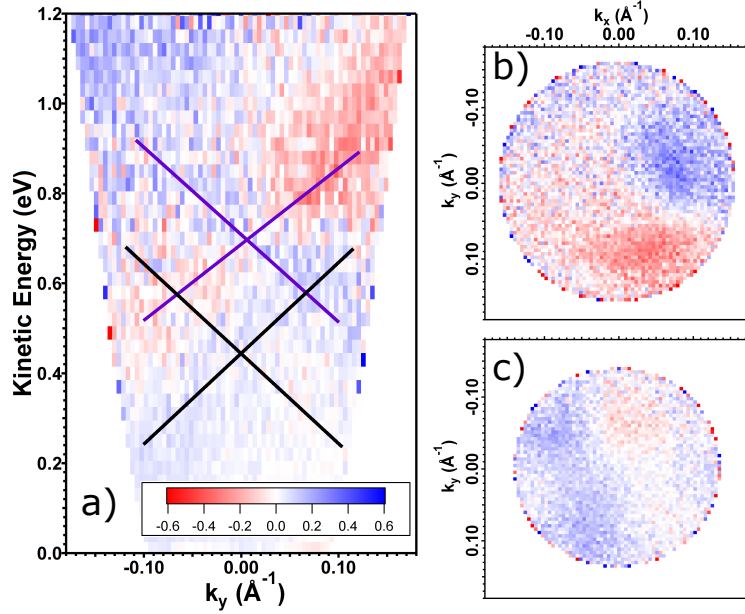A complete understanding of the providence of the observed patterns would require

Figure 4.5: CDAD patterns measured with p-polarized pump pulses of 1.9 eV photon energy (off-resonant excitation) and circularly polarized probe pulses on Bi_2Se_3. a) Cut along the k_y direction at $k_x = 0$ Å^{-1}. The lines indicate the positions of photoelectrons originating from the occupied TSS (purple lines) excited into the third CB and from the VB excited into the unoccupied TSS (black lines) respectively. b) Cut at 0.86 eV kinetic energy, corresponding to the upper branch of the occupied TSS. c) Cut at 0.62 eV kinetic energy, corresponding to the lower branch of the occupied TSS and the upper branch of the unoccupied TSS.

extended and systematic experimental studies as well as one-step 2PPE calculations including both pump- and probe step. Unfortunately, such calculations are so far not feasible, as they require the description of the intermediate state by a retarded lesser Green's function [51].

4.3.2 Influence of the Crystal Symmetry

We have seen, that the CDAD patterns we recorded on Bi_2Se_3 show mainly three-fold rotational symmetry, reminiscent of the bulk crystal symmetry (*cf.* Fig 4.4), especially considering the comparably weak warping of the TSS. We therefore investigated the impact of the crystal orientation during excitation on the CDAD patterns.

Fig 4.6 shows the CDAD patterns recorded with circularly polarized pump pulses with 1.7 eV photon energy and s-polarized probe pulses with 4.7 eV photon energy, for two different sample orientations. The crystal axes were rotated by approximately 90° with respect to each other in the two measurements, as identified by low-energy electron diffraction (LEED). The upper row shows spectra recorded with the $\overline{\Gamma M}$-axis approximately in the plane of incidence of the light. During the measurements presented in
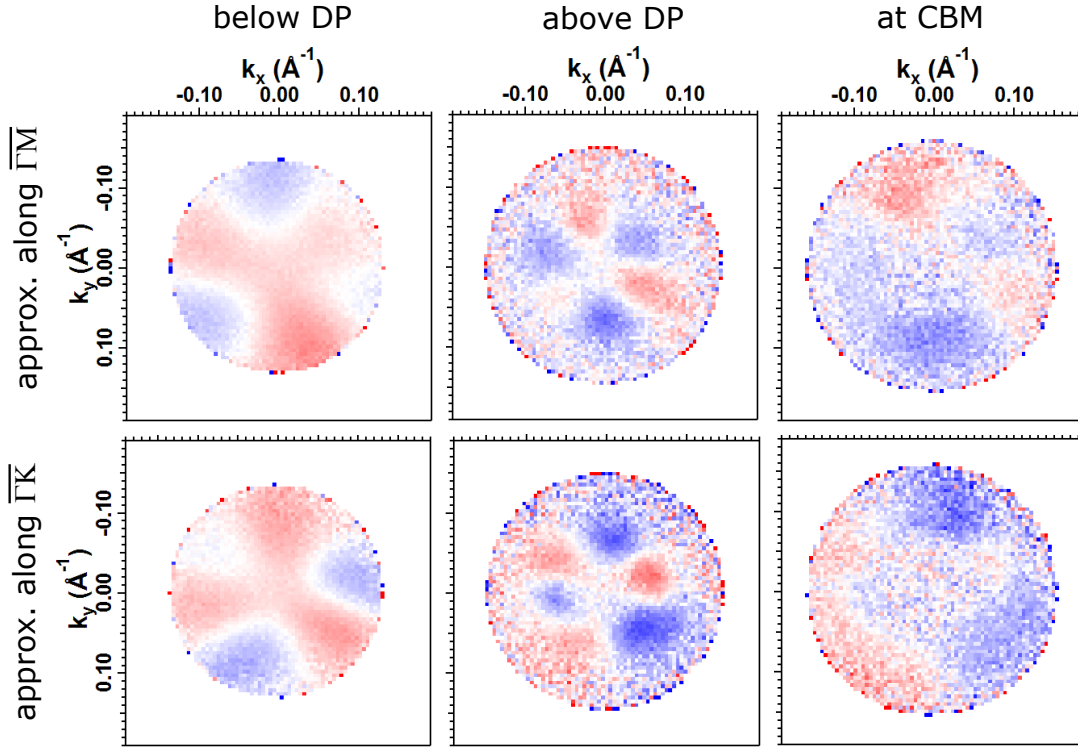
Figure 4.6: CDAD patterns recorded with the plane of incidence of the light (always the x-axis) along the $\overline{\Gamma M}$ (top row) and $\overline{\Gamma K}$ (bottom row) crystal directions. We show the patterns below the DP (first column), above the DP (second column) and at the CBM (third column). All spectra were recorded upon circular excitation with 1.7 eV photon energy and with s-polarized probe pulses (4.7 eV photon energy).

the lower row, the $\overline{\Gamma K}$ crystal axis was approximately aligned with the incidence of the light.

The patterns stemming from the TSSs (first and second column) are six-fold symmetric in both cases, both above and below the DP. Furthermore, they are rotated by approximately 90° with respect to each other, confirming that they indeed reflect the crystal symmetry. The pattern recorded along the $\overline{\Gamma K}$ direction seems to be a little more distorted, possibly due to experimental inaccuracy.
The measurements presented in all other sections of this chapter were recorded with the plane of incidence of the light along the $\overline{\Gamma M}$ direction.

The patterns stemming from the first/third CBM (third column) do not reflect the crystal symmetry, but are rather asymmetric or anti-symmetric, *cf.* right column in Fig 4.6. However, they strongly resemble color inversions of each other (the color representing the sign of the dichroism). This inversion of the dichroic contrast as well as the deviation of the pattern in the CBM from the calculations is unexpected and cannot be easily explained. Apparently the sign of the CDAD is determined by the intensity at

$k_x \approx 0$ in the DC below. The possible origins of these asymmetric patterns, amongst other things, are discussed in the following section.

4.4 Circular Dichroism as a Signature of Photocurrents in Bi$_2$Se$_3$

As shown in Sec. 4.3, photon energies and polarizations have to be chosen carefully in order to obtain reliable information from the photoemission spectra. In the following section, I will present and discuss spectra obtained with circular polarized pump and s-polarized probe pulses. In particular, I will discuss the implications of our results with respect to the excitation of photocurrents on the surfaces of Bi$_2$Se$_3$ and, as a consequence, on TIs in general.

CDAD maps obtained upon resonant excitation between the TSSs are depicted in Figs. 4.7a)-d). Figure 4.7a) shows a cut perpendicular to the plane of incidence of the light. At first sight, a strong dichroic contrast of up to 60% is visible in the energy range of the TSSs. Even though it is slightly distorted, the red and blue areas arrange in a way reminiscent of a cross with legs of opposite contrast. This signal stems from the opposite branches of the TSS, which have opposite spin polarization. This observation is similar to the results of Soifer *et al.* on the second TSS of Bi$_2$Se$_3$ [169] and of Kuroda *et al.* on the first TSS on Sb$_2$Te$_3$ excited with mid-infrared radiation [101, 102] and would support the thesis of the light coupling predominantly to electrons whose spin corresponds to the photon angular momentum [112].

However, the full CDAD maps reveal clear threefold symmetric patterns, both at energies below and above the DP: Below the DP, a strong threefold pattern can be seen that extends uniformly over the entire measured k-range (Fig. 4.7b). Above the DP, a threefold pattern shows up at the constant energy surface of the TSS (Fig. 4.7c). Such symmetric excitation patterns would not lead to a photocurrent. Instead, the threefold patterns reflect the bulk symmetry, even though the initial state is of surface character. Asymmetric patterns, the signature of photocurrents, can only be seen in energy ranges in which the TSS hybridizes with the bulk bands (Fig. 4.7d). It should be emphasized that the threefold symmetrical excitation patterns in the energy range of the TSS can only be observed by recording the full k$_{||}$-range, while cuts along a single k$_{||}$ direction, as they are recorded with hemispherical analyzers, can be misleading (*cf.* Fig. 4.7).

The comparison between our results and one-step photoemission calculations in Fig. 4.7 c) *vs.* f) and d) *vs.* g) suggests little to no influence of the intermediate states (*cf.* also Sec. 4.3 and Fig. 4.7). As the only exception, the calculations were not able to reproduce the asymmetric patterns we observed close to the Fermi level, *cf.* Fig. 4.7 b) *vs.* e). This indicates a more complex process here, involving the pump and probe step, the intermediate state or possibly other mechanisms not captured by theory.
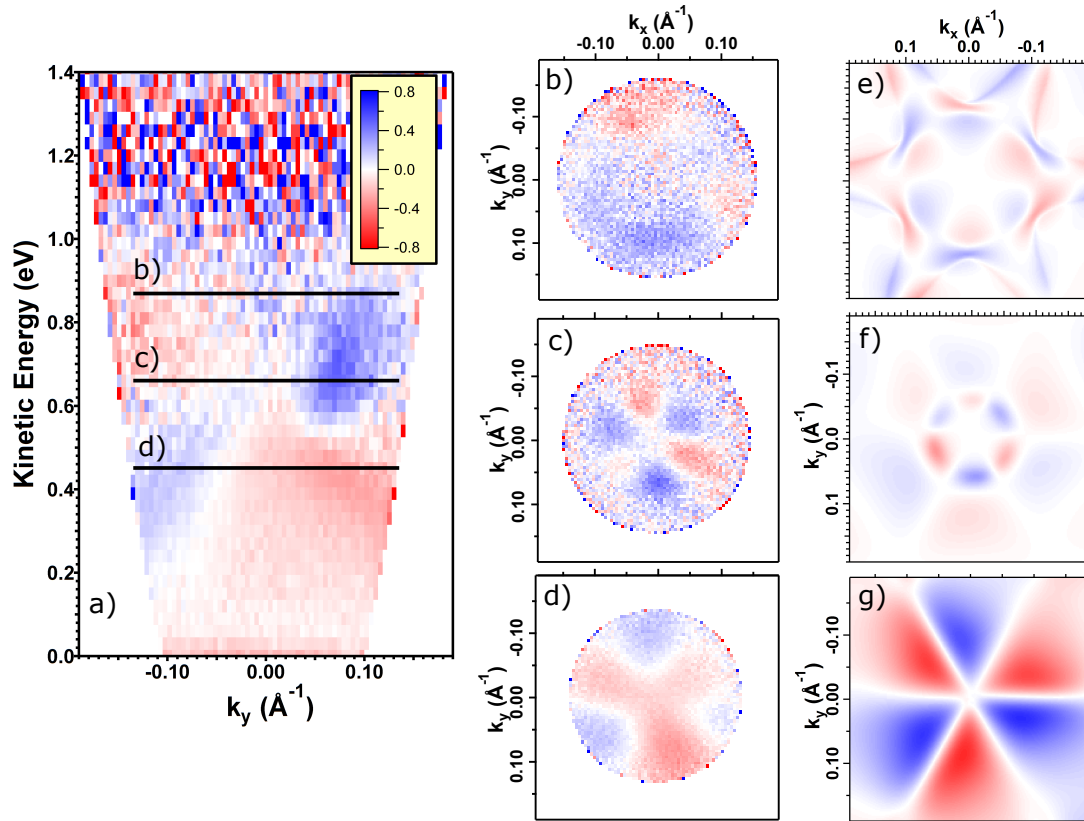To further test the influence of the intermediate state on the spectra, we performed

Figure 4.7: CDAD maps of the TSSs of Bi$_2$Se$_3$ recorded with circularly polarized pump pulses of 1.7 eV photon energy (resonant excitation) and s-polarized probe pulses with 4.7 eV photon energy. a) The 2D-pattern along k_y (at $k_x = 0$ Å^{-1}) shows the expected reversed dichroism at the DP. b-d) The complete CDAD maps extracted at the kinetic energies indicated by vertical lines in Fig. 4.7a. The narrow energy range where the TSS hybridizes with the bulk CB exhibits an anti-symmetric pattern (b), while the spectra reveal threefold patterns for the upper (c) and lower (d) TSS inside the bulk band gap. e-f) Calculated CDAD patterns for direct photoemission with circularly polarized light of 6.4 eV photon energy from the occupied TSS agree well with the measurements, indicating little influence of the intermediate states (unoccupied TSS).
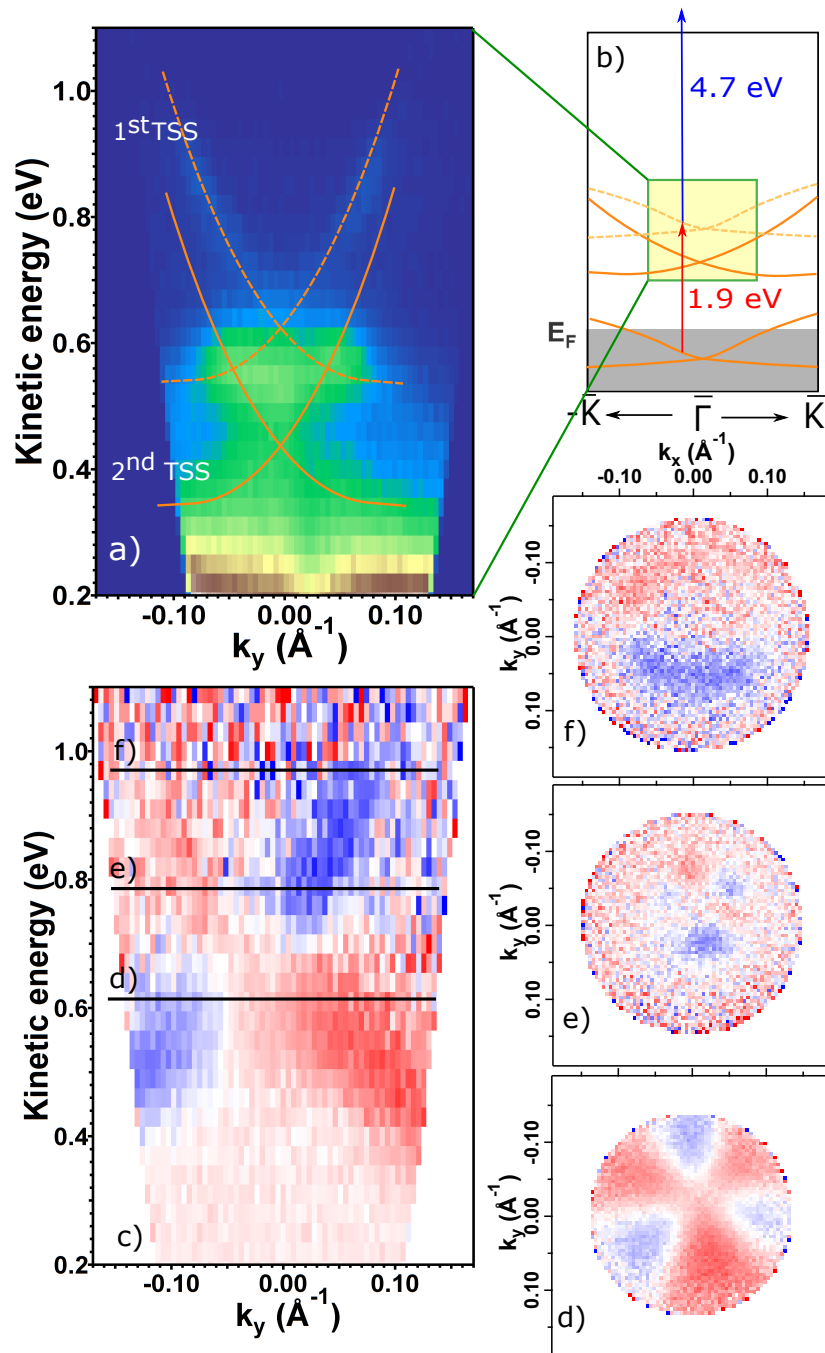
Figure 4.8: a) 2PPE intensity map along k$_y$ for off-resonant excitation. Occupied (1st) and unoccupied (2nd) TSSs are both discernible (orange lines serve as guide to the eye). b) Pump-probe scheme for off-resonant excitation. d-f) The CDAD maps extracted at kinetic energies indicated by the horizontal lines in Fig. 4.8c show patterns very similar to the resonant case (*cf.* Figs. 4.7b-d).

2PPE measurements with the excitation detuned from resonance. At a pump pulse photon energy of 1.9 eV the photoelectron intensity map in Fig. 4.8a shows signatures from both Dirac cones, separated by 0.2 eV. Fig. 4.8b) illustrates the off-resonant pump and probe scheme. The corresponding CDAD patterns reveal no distinct features in the energy range that corresponds to photoelectrons from the 2nd, unoccupied TSS (Fig. 4.8c). In contrast, the CDAD signal from the 1st, occupied TSS manifests very strong similarities to the case of resonant excitation: The cut perpendicular to the plane of incidence of the light shows an anti-symmetric pattern as assumed by McIver *et al.* [112] (Fig. 4.8c). However, the CDAD above and below the DP shows distinct threefold patterns (Figs. 4.8d and e), while anti-symmetric patterns can only be found at an energy range that corresponds to initial states close to the Fermi level (Fig. 4.8f), *i.e.* where the TSS hybridizes with bulk bands. These results match those for resonant excitation and therefore indicate that the intermediate state does not influence the observed CDAD patterns.

In conclusion, the circular dichroism we observe in Bi₂Se₃ stems from the coupling of the circularly polarized light of 1.7 eV and 1.9 eV photon energy to the initial state. Neither the intermediate nor the final states or the probe photons influence these patterns. The CDAD patterns therefore reflect the excitation patterns of Bi₂Se₃ with circularly polarized light.

Perfectly threefold excitation patterns of the carriers do not support photocurrents, as any contribution is canceled by the two symmetrically equivalent features rotated by $\pm 120°$. However, it is evident from the spectra in Fig. 4.7 and 4.8, there are residual asymmetries present in the experimental data. In order to compare our results more qualitatively to the reported photocurrents, we want to extract this asymmetry and estimate the strength of the current resulting from the asymmetry.
We obtain the overall asymmetry with respect to the kardinal directions k_x, k_y by integrating the measured asymmetry over the spectra and weighting with a cosine function to account for the $k_\parallel$ component along the specified direction:

$$A_i^{\text{tot}} = \frac{\sum_{k_\parallel} I_{CDAD}\left(k_\parallel\right) \cos\phi_i}{\sum_{k_\parallel} \cos\phi_i} \ , \quad \phi_i = \angle k_i, k_\parallel \ . \tag{4.1}$$

The projection by the $\cos\phi_i$ onto one of the directions serves to directly estimate the current in this direction: Within the TSS, the linear dispersion leads to uniform group velocity, pointing radially out from the $\overline{\Gamma}$ point. The weighted integration therefore gives us the percentage of carriers in the excited population contributing to a current in this direction, weighted with the projected velocity in that direction.
From the two CDAD patterns of the Dirac cone presented in Fig. 4.7b and c, we derive the asymmetries presented in Tab. 4.1. k_y marks the direction perpendicular to the plane of incidence of the light, while k_x is the k-space direction parallel to the incidence of light. From the commonly assumed excitation mechanism, one would expect large differences between these two directions, namely large asymmetries in k_y and small

to no asymmetry in k_x. However, we find asymmetries that are in the same order of magnitude within the TSS, but slightly more pronounced asymmetries in the CBM. The difference is less pronounced than might be intuitively expected due to the smaller maximal asymmetry in the region of the CBM.

For comparison, we also present the asymmetry

$$A_y^{\text{strip}}$$

integrated along a narrow strip ($\Delta k_y \approx \pm 0.01\,\text{Å}$) around $\overline{\Gamma}$ as opposed to the entire accessible k-range. These values corroborate that the spectra along a single **k**-direction can be very misleading with regard to the total asymmetry of an excitation and therefore the presence of photocurrents. The presented asymmetries are representative for the respective energy ranges, *i.e.* integration over the full energy region with the respective pattern yields very similar numbers (*cf.* Tab. 4.2).

Energy range	A_y^{strip}	A_y^{tot}	A_x^{tot}
CBM	-8.2%	-5.6%	0.6%
Above DP	-14.8%	-2.5%	1.5%
Below DP	11.0%	3.2%	2.0%

Table 4.1: Integrated asymmetries (*cf.* Eq. 4.1) of the CDAD spectra shown in Fig. 4.7.

Energy range	A_y^{strip}	A_y^{tot}	A_x^{tot}
CBM	-8.6%	-5.0%	0.6%
Above DP	-13.8%	-3.5%	1.2%
Below DP	9.5%	2.9%	1.8%

Table 4.2: Integrated asymmetries (*cf.* Eq. 4.1) over the energy ranges corresponding to the CBM, the TSS above the DP and the TSS below the DP for one exemplary sample.

From these asymmetries, we can try to estimate the transient currents present in the excited states in order to compare our measurements to previously reported transport measurements [83, 112, 133].

With the definition of the asymmetry A_i^{tot} in Eq. 4.1, the photocurrent density is given by

$$j(k_y) = n_{ex}\, e\, v_e\, A_y^{\text{tot}}\ , \tag{4.2}$$

where n_{ex} is the number of excited carriers, e is the electron charge and v_e is the quasi-particle velocity. v is easily determined from the DC's slope $\hbar v \approx 3.2\,\text{eVÅ}$(*cf.* Fig. 4.2). From this, we can also determine the density of states in the DC to be $n_{DC} \approx 2 \times 10^{13}\,\text{cm}^{-2}$. We assume that 1% of the electrons in the DC are excited, *i.e.* $n_{ex} = 0.01 n_{DC}$. This yields current densities in the order of $j(k_y) \approx 2 - 3 \times 10^2\,e\text{cm}^{-1}\text{fs}^{-1}$. Niesner *et al.* have reported, that the lifetimes of carriers in the unoccupied TSS are

70 fs (*cf.* also the following section) [126]. However, the corresponding photoholes are assumed to have a much longer lifetime in the picosecond range [127, 151], which is compatible with the duration of the observed photocurrents [83]. We therefore assume the photocurrents are mainly carried by the photoholes. With the respective lifetimes and a repetition rate of $\approx 300\,$kHz and a spot size of $\approx 300\,\mu$m, we end up at $10^8\,e$/s, which corresponds to 10 pA.

Alternatively, we can estimate the number of carriers contributing to the current from the photoelectron intensity: The overall countrates in the presented spectra is in the order of $10^5\,e$/s. In general, the probability of 2PPE is about five orders of magnitude smaller than direct photoemission, which would mean $\approx 10^{10}$ excited carriers per second. With asymmetries in the order of a few percent in the energy ranges that show any dichroic singnal at all (and therefore about 1% overall asymmetry), we again obtain $10^8\,e$/s, which corresponds to 10 pA.

The estimated currents correspond remarkably well to all of the reported helicity dependent photocurrents [83, 112, 133], while the applied fluences are equally comparable. Therefore, the residual asymmetry in our spectra might well be a sufficient explanation of the observed photocurrents. However, these asymmetries are mainly residual asymmetries, possibly provenient from small experimental inaccuracies, the only exception being the energy range of the CBM. We therefore conclude, that the observed photocurrents in these materials are no intrinsic property of the TSS and therefore can't *a priori* be assumed to be spin-polarized.

4.5 Temporal Evolution of the CDAD Patterns

In the previous sections, we have exclusively discussed CDAD spectra obtained in the temporal overlap of pump and probe pulses, *i.e.* when pump and probe impinge on the sample at the same time. To obtain further insight into the occuring processes during and after photoexcitation of the sample, we can introduce an additional delay between the pulses. In this section, I accordingly show the recorded CDAD of the photoelectrons for several time delays between pump and probe pulses and compare them to the overall intensity in the corresponding energy ranges. In the following, negative delays will refer to the probe arriving before the pump pulse and vice versa at positive delays. A delay of 0 fs corresponds to time zero, *i.e.* the maximal overlap of the pulses.

We performed time-resolved measurements for all polarization and wavelength combinations, however, I will limit this chapter to the data obtained for resonant excitation and s-polarized probe, as it lends itself best to the discussion of photocurrents. In principle, all the findings were reproduced in the other measurements. As the recording of the CDAD patterns requires fairly long exposure times (5-15 min per polarization and delay), it was not possible to record full dichroic delayscans. Instead, CDAD patterns were recorded at selected delays and are compared to delayscans recorded separately on the same sample with both linear pump and probe pulses and a stepwidth of 15 fs.
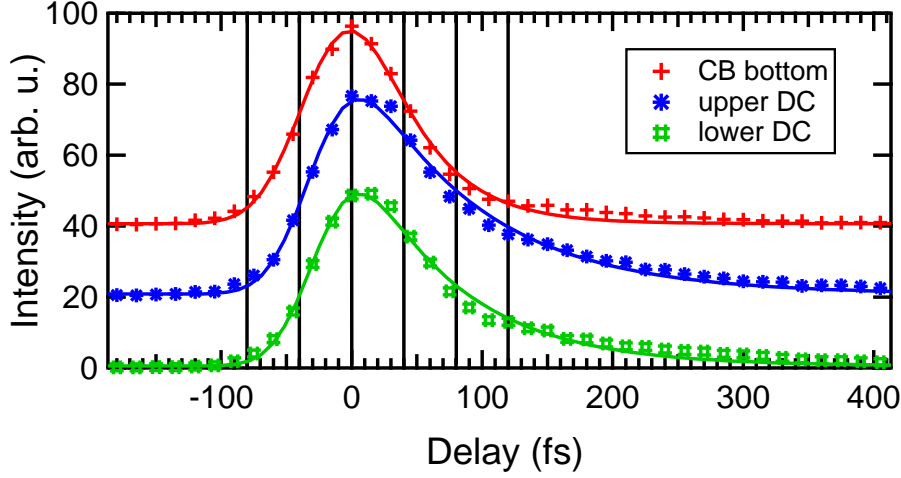
Figure 4.9: Photoelectron intensity as a function of pump-probe delay for three different energies, corresponding to the CDAD patterns in Figs. 4.7, 4.8, 4.10, 4.11. The delay spectra were obtained with p-polarized pump pulses of 1.7 eV photon energy and s-polarized probe pulses with 4.7 eV photon energy. The intensity was integrated over the entire accessible k-space and slices of 30 meV width.

Fig. 4.9 shows the photoelectron intensity at different kinetic energies over the pump-probe delay, integrated over the entire accessible k-space. The selected energies correspond to the CDAD patterns shown in Figs. 4.10, 4.11 and in the previous sections, *i.e.* the TSS below the DP, the TSS above the DP and the bottom of the CB. For all three energies, the intensity peaks at the so called time zero. These spectra are a convolution of the cross correlation of the two pulses, *i.e.* the time resolution of 80 fs, with an exponential decay representing the lifetimes of the electrons in the unoccupied TSS. Fitting yields lifetimes between 40 and 90 fs, in line with previously reported values [126]. Note that these short lifetimes are not compatible with the reported photocurrents, which were present for times in the order of picoseconds after photoexcitation [83]. This indicates, that the photocurrents are carried by the photoholes rather than the excited electrons, as already established in the previous section. We come to this conclusion, because the former are suspected to have much longer lifetimes in the picosecond range but possibly the same asymmetry.

Figs. 4.10, 4.11 shows the CDAD patterns at the delays indicated by the black lines in Fig. 4.9. Especially at negative delay, the previously reported patterns are clearly discernible. Even with minimal overlap between pump and probe pulse (-80 fs delay), the threefold patterns in the upper and lower DC as well as the anti-symmetric pattern in the CBM start emerging. The most intense dichroic signal is found at delays from approximately -40 fs to 0 fs, so slightly before time zero. Notably, the contrast in these patterns decays much faster than the population (*cf.* the spectra recorded at positive delays), most evident in the comparison of the spectra 80 fs before and after time zero. In other words, the contrast of the CDAD patterns follows the cross correlation rather
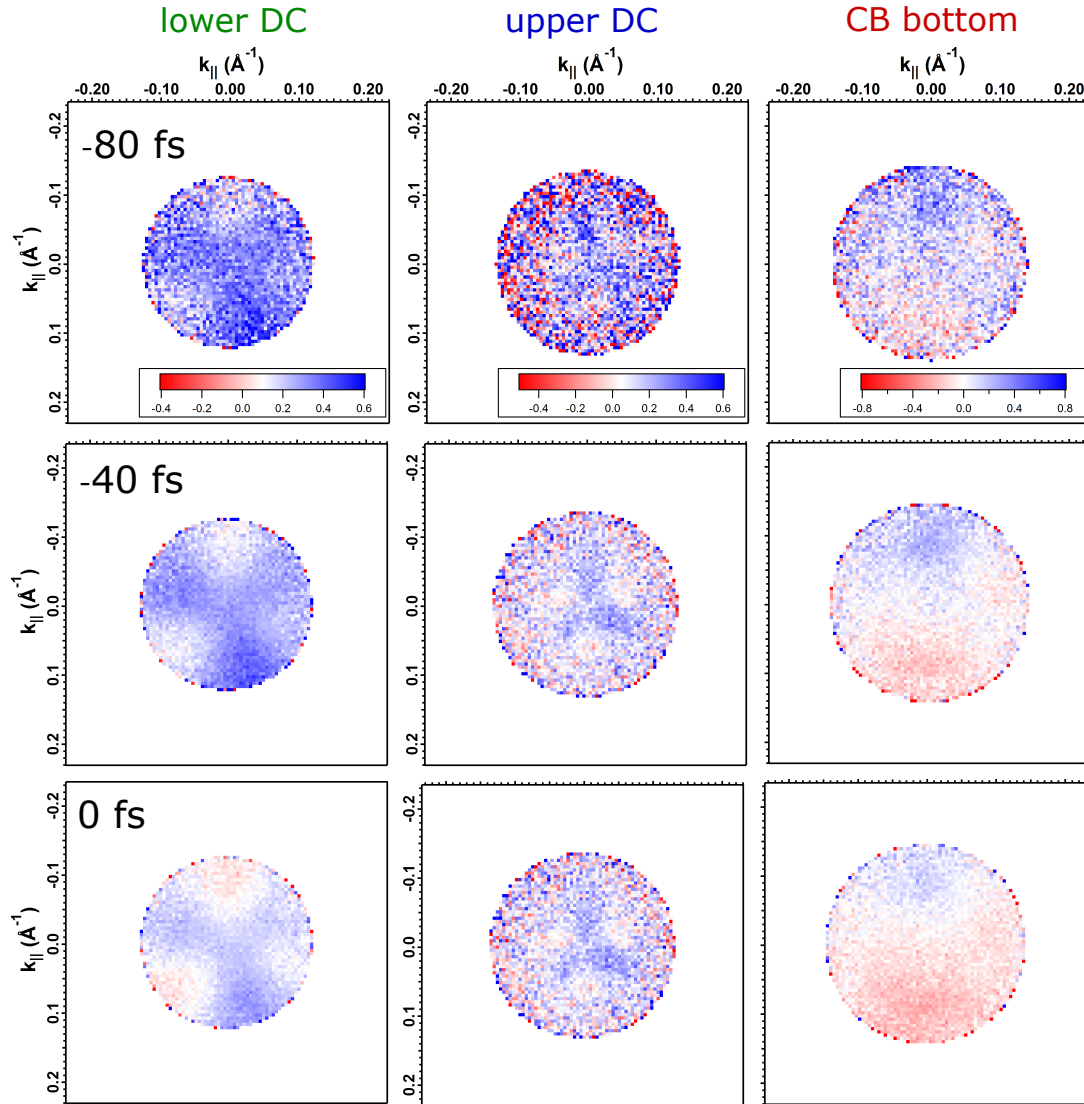
Figure 4.10: CDAD patterns recorded at different delays and kinetic energies for resonant excitation with circularly polarized pump pulses. Spectra in the first column stem from the TSS below the DP, the second column from the TSS above the DP and the third column within the CBM (*cf.* Figs. 4.7 and 4.8 of the previous section). The rows correspond to different delays between the pump and probe pulse, from top to bottom 80 fs before time zero, 40 fs before time zero and at time zero, as indicated by the first three black lines in Fig. 4.9. The patterns recorded after time zero can be found in Fig. 4.11.
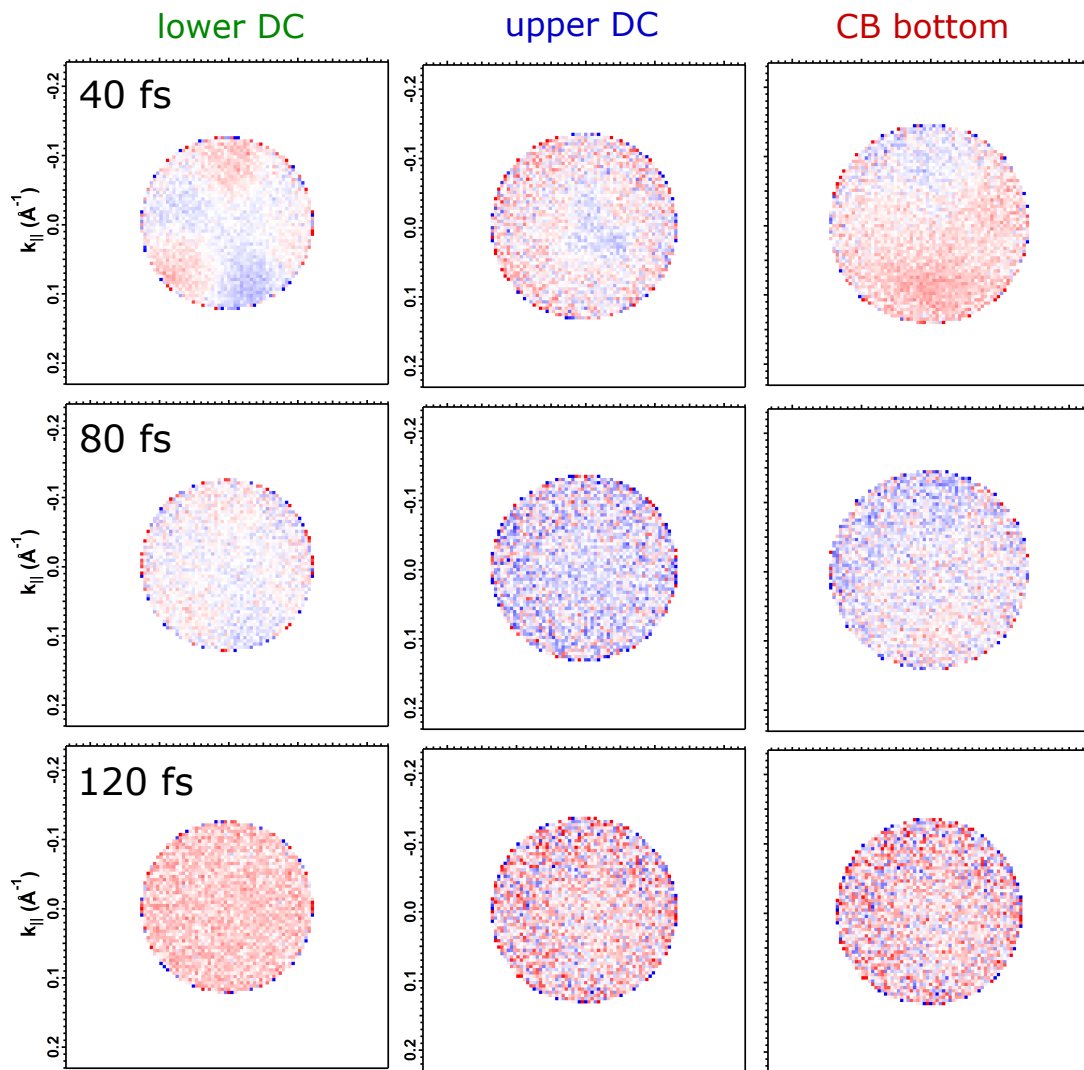
Figure 4.11: Continuation of Fig. 4.10, showing the CDAD patterns at delays of 40, 80 and 120 fs, as indicated by the last three black lines in Fig. 4.9.

than the population in the intermediate state or actually decays possibly even faster than that. This is further proof that the observed patterns stem from the initial states and then quickly dephase, even within the duration of the pump pulse. We observe this trend both for s- and p-polarized probe pulses.

4.6 Conclusion

In this chapter, the excitation of the electrons in the TSS of Bi_2Se_3 by circularly polarized light was studied by means of 2PPE. The aim was to clarify the origins of helicity-dependent photocurrents observed in previous transport measurements [112].

We showed that the CDAD patterns observed in the PE spectra depend heavily on the choice of probe pulse polarization. When s-polarized probe pulses are used, the CDAD patterns agree well with direct photoemission calculations, indicating little to no influence of the intermediate state and the probing step. The CDAD patterns follow the orientation of the crystal, with minor deviations.

Variation of the pump pulse energy from 1.7 to 1.9 eV, which corresponds to resonant and off-resonant excitation between the TSSs respectively, corroborates, that the intermediate state has little to no influence on the CDAD patterns. Furthermore, the final state should not influence the patterns due to its s-like character [158]. We therefore conclude, that the patterns stem from the coupling of the photons to the initial state.

The observed CDAD patterns do not conform with the generally assumed coupling of the photon angular momentum to the electron spin. This coupling mechanism would lead to anti-symmetric patterns with respect to the plane of incidence of the light. Instead, we observe three-fold rotational symmetric patterns reflecting the bulk crystal symmetry. Symmetric patterns like these cannot carry a photocurrent. However, there is residual asymmetry present in the patterns, especially at the CBM, potentially stemming from experimental inaccuracies and/or physical processes involving the intermediate state, as they are not reproduced in the theoretical calculations. An estimation of the currents corresponding to these residual asymmetries yields the same order of magnitude as observed in transport experiments.

Time-resolved measurements show extremely short lifetimes of the intermediate state and an even faster decay of the CDAD patterns. This faster decay of the excitation patterns indicates a redistribution though elastic scattering or symmetric filling from the higher lying states. This decay is much faster than the persistence of photocurrents [83], which corresponds more to the expected lifetime of the holes left behind by the excited electrons.

We therefore conclude, that the helicity-dependent photocurrents observed in various transport measurements do not stem from the anti-symmetric excitation of the occupied TSS. While it is true that the coupling of the photon to the initial state dominates

the distribution of electrons in momentum state, this coupling leads to a symmetric distribution that cannot carry photocurrents. Residual asymmetries, especially in the region of the CBM, are probably the source of the photocurrents. The exact origins of these asymmetries remain unclear, but we propose experimental inaccuracies like residual linear dichroism and possibly scattering mechanisms or similar effects in the CBM. Due to their duration in the order of a few picoseconds, it is likely that the photocurrents are carried by the photoholes, not the excited electrons.

Chapter 5

Electron and Hole Dynamics in BiTeI

Parts of this chapter have already been discussed in the Master thesis by M. Polverigiani [142], that was supervised by the author.

In the previous chapters, we have already seen that materials with spin-split surface states, induced by spin-orbit interaction (SOI), feature both intriguing fundamental physics as well as a host of possible applications [36, 64, 173]. While the discussion in the last chapter focused on a so-called topological insulator (TI), in this chapter I want to approach a different, but related class of materials, so-called Rashba materials, by looking at the representative BiTeI. While there has been much less focus on Rashba materials in the scientific community, as compared to TIs, there have still been numerous studies towards their properties and possible applications that show a lot of similarities, ranging from thermoelectric properties [98] to possibly spin-polarized photocurrents [111, 130, 131].

While the topological phase is predominantly found in materials with inversion symmetry, the Rashba effect requires the absence of it (*cf.* Sec. 2.2). Therefore, the first time Rashba-type spin splitting could be observed by angle-resolved photoemission spectroscopy (ARPES) was at surfaces of noble metals, where a Rashba-splitting of a few meV is visible in the Shockley surface state [7, 97, 105, 138, 152]. BiTeI, in contrast to those materials, lacks inversion symmetry in its crystal structure and therefore exhibits both spin-split bulk and surface states, as discussed in more detail in Sec. 5.1. As we will see, the lack of inversion symmetry additionally leads to a polar surface with two possible terminations: a layer of Tellurium or Iodine atoms, respectively. In particular, the polar surface of BiTeI leads to an unsual aging process of the material, which can be taken advantage of in order to separate signals from either surface. This is discussed in Sec. 5.1.1. We then focus on the Te-terminated surface and discuss the corresponding electronic structure in more detail in Sec. 5.1.2.

Additionally, the polar surface leads to peculiar electron and hole dynamics. This work focuses on the dynamics in the Rashba states on the Te-terminated surface, which exhibits a significant asymmetry between electrons and holes (*cf.* Secs. 5.2.1, 5.2.2 respectively).

Finally, it has been reported that addition of Mn improves the crystal growth of BiTeI, but does not influence the electronic structure [78]. We investigate the influence on the electronic structure and in more depths on the electron and hole dynamics and compare to a different dopant, namely V. The corresponding findings are presented in Sec. 5.3.

5.1 BiTeI - a System with Giant Rashba Splitting

Arguably the most direct influence of SOI on the surface electronic structure of a material is the so called Rashba effect [28, 29, 150] (for an introduction to the topic *cf.* Sec. 2.2). While the first Rashba-split surface states (RSSs) resolvable by ARPES were found on the surface of Au(111) [105], recently the interest has shifted from noble metals with RSS to systems with so called giant Rashba splitting of several dozen meV [47–49]. One of these materials is the layered crystal BiTeI. Due to its stacking sequence, BiTeI crystals lack inversion symmetry and therefore BiTeI does not only exhibit a giant Rashba splitting of its surface states, but also Rashba split bulk bands [47, 78, 104, 108, 157]. Additionally, it features polar surfaces with large surface band bending, an electron-like RSS on the Te-terminated surface, and a hole-like RSS on the I-terminated surface [34]. Stacking faults within the crystal lead to a coexistence of both terminations on the same surface [27].

5.1.1 Crystal Structure, Electronic Structure, and Aging of BiTeI

BiTeI, similar to the TI Bi_2Se_3 discussed in the previous chapter, grows as a layered crystal composed of covalently bound multilayers, stacked by Van-der-Waals forces. In its case, Te-Bi-I trilayers (TLs) form, which exhibit a covalent bond between Te and Bi, which in turn are almost ionically bound to the strongly electronegative I. As a consequence, the TL lacks inversion symmetry and features partial charges on its two surfaces, namely a positive partial charge δ^+ on the Te-terminated surface and a negative partial charge δ^- on the I-terminated surface. The stacking ...-I)–(Te-Bi-I)–(Te-Bi-I)–(Te-... is energetically favourable, leading to an overall crystal structure that lacks inversion symmetry (*cf.* Fig 5.1a).

The peculiar stacking sequence of BiTeI leads to polar surfaces of the crystal, and therefore to band bending at both surfaces in order to compensate the surface charges. The combined band bending of both surface terminations, measured by X-Ray Photoelectron Spectroscopy, has been reported to be as large as $0.8 − 0.9$ eV on freshly cleaved samples [27, 34], in line with calculations of the surface potential [47] (*cf.* Fig 5.1b). These predict a change in surface potential within the top TLs of almost 0.3 eV.

BiTeI crystals are semiconductors, *i.e.* they possess a bulk band gap. However, they are intrinsically n-doped, shifting the Fermi level into the conduction band minimum (CBM), making them degenerated semiconductors [37]. Reported carrier densities are typically in the order of 10^{19} cm^{-3} [71, 78, 98]. The intrinsic doping stems from over-stochiometric iodine, which is built into the lattice on tellurium sites during the growth of the crystals, typically in the range of 2% (by number). These defects are partially ionized, acting as donors [71].
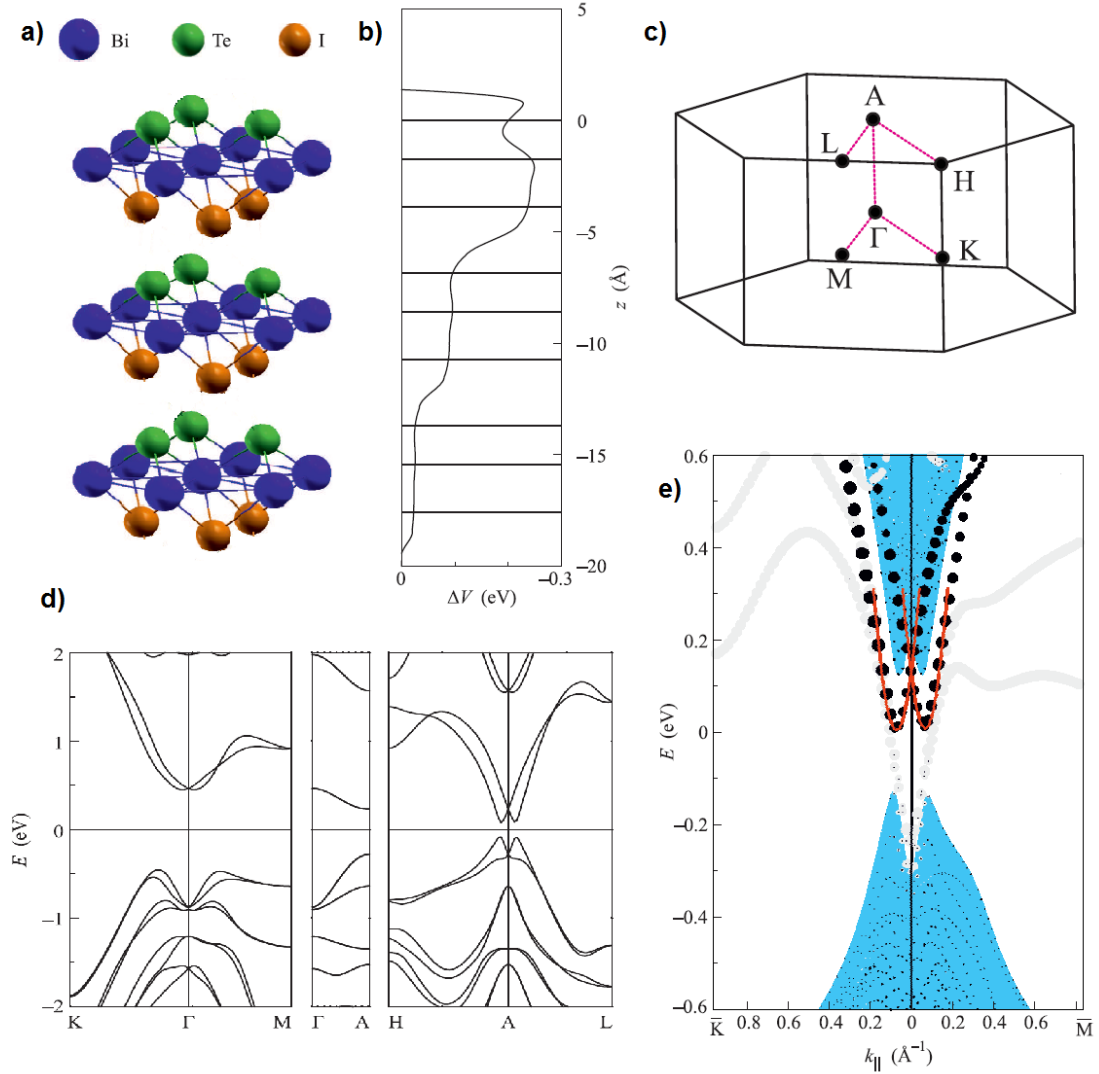
Figure 5.1: a) Schematic of the trilayer crystal structure of BiTeI. b) Calculations of the change in potential in the near-surface layers of a Te-terminated crystal indicate the band bending. c) Schematic of the *hcp* bulk BZ d) DFT calculation of the bulk BS of BiTeI between the high symmetry points of the BZ e) DFT calculation of the surface electronic structure of Te-terminated BiTeI. Calculations b) and e) were performed with a 8 TL slab with hydrogen on the I-terminated side. Figure adapted from [47].

The TL of BiTeI are ordered in a hexagonally close packed (*hcp*) lattice, similar to Bi_2Se_3. This leads to a hexagonal Brillouin zone (BZ), as depicted in Fig 5.1c). Density functional theory (DFT) calculations, supported by ARPES measurements have revealed that the band gap of BiTeI has direct character and is situated at the *A* point of the BZ [47, 78]. As BiTeI crystals lack inversion symmetry (*cf.* Fig 5.1a), not only the surface states of BiTeI are Rashba split, but also the bulk states (*cf.* Fig 5.1d), particularly those forming the valence band maximum (VBM) and CBM. The difference in binding energy of the VBM and CBM, *i.e.* the size of the band gap, has been repoted to be just short of 0.4 eV [34]. The RSSs of BiTeI form around the VBM and CBM respectively, *i.e.* at the surface projection of the *A* point, which is the $\overline{\Gamma}$ point. This in combination with the intrinsic n-doping of the crystal makes these states easily accessible for ARPES, even when performed with low photon energies (for limitations of low-energy ARPES, *cf.* 3.1).

The charge of the polar surface of BiTeI highly influences the formation of the aforementioned RSSs, leading to hole-like RSSs with downwards band bending on the I-terminated surface and electron-like RSSs with upward band bending on the Te-terminated surface. A DFT calculation of the surface projected band stucture of Te-terminated BiTeI, which will be the focus of this chapter, can be found in Fig 5.1e).

Bulk stacking faults lead to a coexistence of both types of surface terminations on the same crystal surface, with domain sizes in the order of 100 nm [27, 49, 50] (*cf.* Fig 5.2a) or on the order of 150 μm [34]. This makes it nearly to fully impossible to focus our laser beams (beam diameter in focus $\approx 150 - 200$ μm, *cf.* Sec. 3.2.1) onto a single domain of our crystals. Due to the opposite band bending on the two surface terminations, features from both terminations would overlap in the ARPES spectra and become indistinguishable with our spectral resolution (*cf.* Fig 5.2b-d).

In order to obtain better signals, we were able to exploit the higher reactivity of the I-terminated surface as compared to the Te-terminated surface [34, 50]: Samples were cleaved *in-situ* at room temperature (RT) and a pressure of 2×10^{-9} mbar and left at these conditions for at least 12 h in order to achieve an aging of the surface. During that time, the I-terminated surface domains saturated with residual gases, which suppresses the photoemission signal from these domains. More accurately, it flattens the band bending, removing the states of the I-terminated surface from the probed energy region [34, 50]. Furthermore, the electron-like RSS of the Te-terminated surface, due to their steeper dispersion and the band bending of that surface, are much better accessible with our available photon energies than the hole-like RSS of the I-terminated surface would be. Therefore, the following analysis will purely focus on the Te-terminated surface. We observed no further change of the surface throughout the ARPES and time- and angle-resolved photoemission spectroscopy (tr-ARPES) measurements, which were performed at pressures of $\leq 7 \times 10^{-11}$ mbar. During these measurements, the samples were kept either at RT or at 60 K.
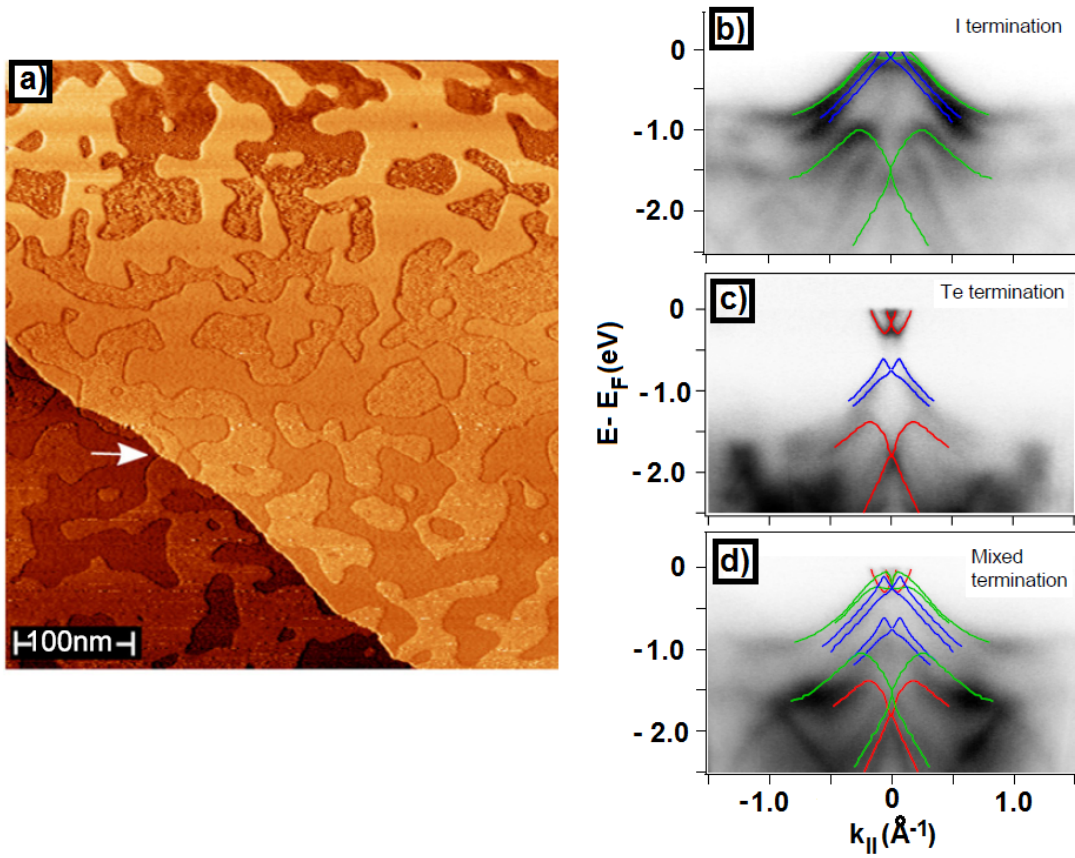
Figure 5.2: a) STM image of a BiTeI surface. The different domains are clearly distinguishable. The white arrow indicates a domain wall that spans over two different trilayers, indicating that the domains continue into the bulk. Taken from [50] b-d) Photoemission spectra from areas with different terminations on the same BiTeI crystal. Figure adapted from [34].

5.1.2 Static Measurements on BiTeI

In this section, I will present static measurements obtained on three different samples of BiTeI: pristine BiTeI, BiTeI with 2.5% vanadium doping and BiTeI with 3% manganese doping. All samples were cleaved and aged at 2×10^{-9} mbar as described above in order to suppress the photoelectron (PE) signal from the I-terminated surfaces. However, the signal from the samples was spatially less than homogeneous, showing regions with clearly recognizable dispersions as well as regions with much more blurred signal. The best signal was typically obtained on regions with smeared out left edges in the photoemission signal, indicating surface contamination and therefore a range of work functions within the laser spot. On samples transferred into the better vacuum of the analysis chamber ($8 \cdot 10^{-11}$ mbar) right after cleaving, typically a sharp left edge at a work function of 5.3 eV was observed, but the angle-resolved images revealed no discernible
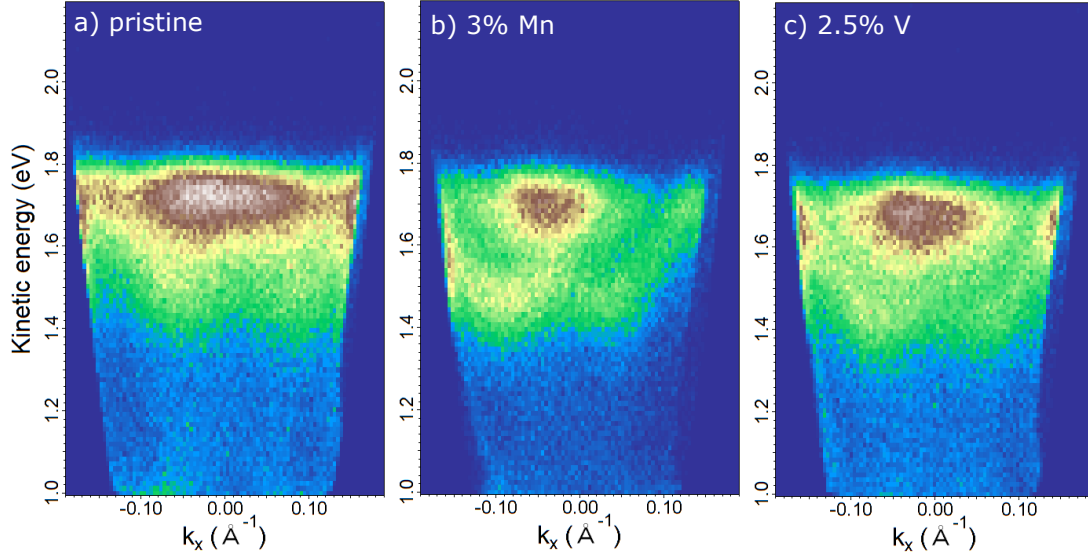
Figure 5.3: PE spectra recorded on three different aged BiTeI-samples: pristine BiTeI (a), BiTeI with 3% manganese doping (b) and BiTeI with 2.5% vanadium doping (c). All presented spectra were recorded at $60\,\mathrm{K}$ and $8\cdot 10^{-11}\,\mathrm{mbar}$ with $6.2\,\mathrm{eV}$ photon energy and an integration time of five minutes.

dispersions whatsoever. This is very much in line with the observations of Crepaldi *et al.* and Fiedler *et al.*: Residual gases will predominantly react with the I-terminated surface, flattening the band bending and thereby removing the according signal from the probed region [34, 50].

We carefully selected spots with the best discernible dispersions on each sample for our measurements. Resulting exemplary spectra can be found in Fig 5.3. Due to the orientation of the crystallites, the spectra sometimes are slightly offset from normal emission. As the sensitivity of our detector had deteriorated in the center, we did not correct for this offset but rather increased it in the k_x-direction, to image the crossing point of the RSS parabolas, often referred to as Dirac point (DP) in the literature, at a more sensitive detector region.

On first sight, the signal is comparable in energy and dispersion on all three samples, indicating the same level of carrier doping. Furthermore, all three samples show the expected spectra: The large blurred intensity at low binding energies, *i.e.* from right below the Fermi level to binding energies of $E_B = E_F - E \approx 0.1\,\mathrm{eV}$, stems from the Rashba-split bulk conduction band (CB). In constrast to direct photoemission measurements [34, 78, 108], we cannot resolve these bands in detail, probably due to the larger spectral widths of our probe pulses and to the larger escape depth that, combined with the surface bend bending, leads to a blurring of the bulk bands. The signal from the CBM overlays the inner branches of the Rashba-split Te-surface states, which lie at roughly the same energies and momenta. The signal below the CBM stems from the

RSS and accounts for the intensity up to $E_B = E_F - E \approx 0.3\,\text{eV}$ on all samples. The signal below the bottom of the RSS stems from within the band gap and is therefore probably composed of electrons from defect states within the band gap as well as inelastically scattered photoelectrons from the main features.

It is evident from Fig. 5.3, that the RSS parabolas are much better resolved on the doped samples compared to the spectrum of the pristine sample. This is surprising, as the freshly cleaved samples of both doped BiTeI specimen macroscopically looked significantly more flaky than the mirror-like pristine sample.

This apparent difference in quality of the spectra can have three different explanations: First, the dopants might improve the growth - *i.e.* the bulk crystal structure - of the samples on a microscopic level, as proposed by Ishizaka *et al.* [78]. Second, they might improve purely the surface quality, either by reducing the reactivity of the Te-terminated surface or by favoring the formation of evener surfaces during the cleaving process. As a third possibility, the reverse might be the case and the pristine sample possesses the better (surface) crystal quality. Our observations indicate that in this case the photoemission from the bulk material is more effective, *e.g.* by a larger electron mean free path during the photoemission process, leading to an increased signal from the bulk carriers overshadowing the signal from the surface. Unfortunately, low-energy electron diffraction (LEED) measurements on all samples were difficult due to the small sample sizes and could not reveal significant differences in the crystal structure. However, comparison of the dynamics (*cf.* Sec. 5.3) indicates that indeed the Mn-doped sample features less defect scattering of the excited carriers, which would in turn indicate a better crystal structure.

As the dispersions seem very similar on all samples, I will exemplarily focus on the Mn-doped sample for the quantitative discussion of the features, as its spectra show the best quality both in average and absolute. Fig. 5.4 shows cuts through a static ARPES spectrum recorded on a different spot on the same Mn-doped sample presented in Fig. 5.3 at 60 K. The cut along the k_x direction (Fig. 5.4a) through the DP of the RSS was fitted with two parabolas in order to obtain the Rashba parameters of the sample. The fit yields a Rashba splitting, *i.e.* a $k_{||}$ displacement, of $\Delta k_R = 0.11\,\text{\AA}^{-1}$ and a Rashba energy, *i.e.* a downshift in energy due to the SOI, of $E_R = 97\,\text{meV}$. Both of these values are in excellent agreement with previously reported values [34, 78].

The spectra presented in Fig. 5.4 b-e) are obtained by cutting at certain energies ($\Delta E = 12\,\text{meV}$) through the obtained three dimensional data. They reveal the constant energy contours of the RSS and the CBM. The black lines superimposed in the spectra serve as guide to the eye. As mentioned before, the sample was slightly tilted in the k_x and k_y direction in order to access at least half of the Fermi contour of the outer branch of the RSS and to remove the DP from the less sensitive spot at the center of the detector. The outer Fermi contour of the RSS (Fig. 5.4b) shows weak hexagonal warping (*cf.* Sec. 2.3), which might also explain the slight deviation of the RSS parabolas from the fit close the the Fermi edge in Fig. 5.4a). Meanwhile, the inner Fermi contour, overlapped with the signal from the CBM, shows no evident warping, as predicted by Eremeev *et al.* [47].
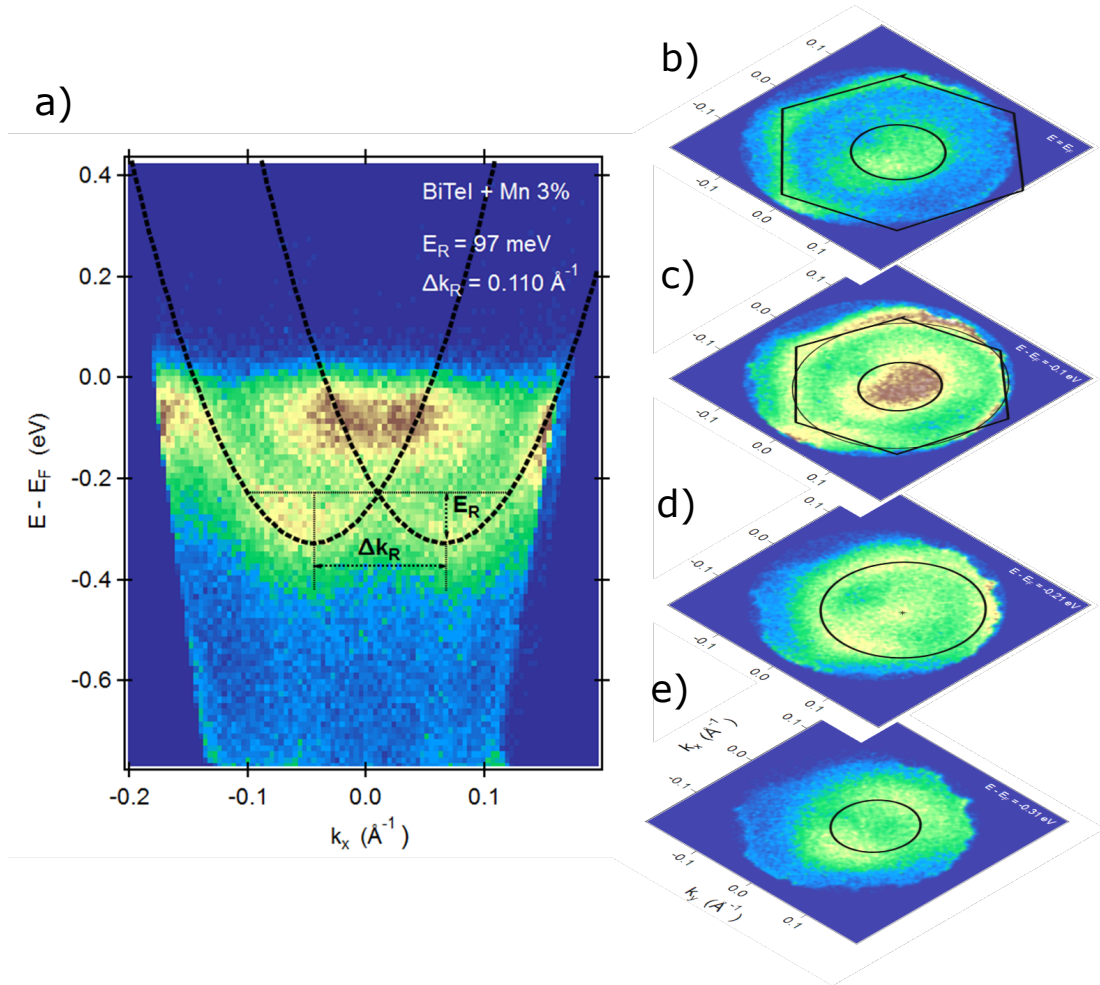
Figure 5.4: PE spectra recorded on an aged Mn-doped BiTeI-sample at $60\,\mathrm{K}$ sample temperature. a) Dispersion along the k_x direction. The superimposed parabolas were fitted to the dispersion of the RSS and yield a Rashba splitting $\Delta k_R = 0.11\,\text{Å}^{-1}$ and Rashba energy $E_R = 97\,\mathrm{meV}$ according to literature. b-e) Full $k_{||}$-maps at different energies show a small hexagonal warping (*cf.* Sec. 2.3.3) of the RSS at the Fermi energy (b), the band bottom of the conduction band at $0.1\,\mathrm{eV}$ binding energy, overlapping with the inner contour of the RSS (c) the DP of the RSS at a binding energy of $0.21\,\mathrm{eV}$ (d) and the band bottom of the RSS at a binding energy of $0.31\,\mathrm{eV}$ (e)

The latter result has, however, to be taken with a grain of salt, as a warping would be hard to determine due to the limited resolution and the distortion of the spectrum due to the inhomogeneous detector sensitivity.

Fig. 5.4c) shows the constant energy contours at a binding energy of $E_B = E - E_F = -0.1\,\text{eV}$, which corresponds to the bottom of the CB. At this energy, the warping of the outer branch of the RSS is less pronounced.

At an increased binding energy of -0.21 eV (Fig. 5.4d), which corresponds to the DP of the RSS, there is no more warping discernible in the outer branch.

The band bottom of the RSS is shown in Fig. 5.4e). It is situated at a binding energy of -0.31 eV and has the expected ring-like structure.

For a more quantitative comparison between the band structures, more precisely the band positions, of the three different samples, we integrated the spectra over the entire recorded $k_{||}$-space and fitted them with a function representing the to-be-expected density of states (DOS): Three terms to account for the different features, cut off with a Fermi function and convoluted with a Gaussian to account for the limited spectral resolution of the probe pulse (*cf.* Fig 5.5). The bulk bands are modelled with a sqareroot function, as to be expected for a parabolic three-dimensional dispersion. The RSS is a parabolic two-dimensional state and should thus possess a constant DOS. However, we found that the low-energy edge is significantly broadened due to the single-particle lifetime at the bottom of the band. We therefore modelled it with an arcus tangens. The third component of the fitting function is a background that accounts for the underlying signal, most probably derived from defects and inelastically scattered electrons.

We can see in Fig 5.5, that this model yields very good fits for all three spectra, corroborating our interpretation of the respective spectral features. In addition, one can see that the relative intensities of RSS and CBM vary in dependence of the doping. This is in line with the observations in the k-resolved spectra, see the discussion above.

The positions of the respective band bottoms, as obtained from the according fits, can be found in Tab. 5.1. On first sight, it is apparent that the binding energies of the RSS and the CBM are very similar for all three samples. However, the binding energy of the RSS is slightly larger (around 50 meV) for the doped samples, as compared to the pristine sample, while the CBM also shows a slightly increased binding energy on the V-doped sample, indicating that Vanadium might contribute to the doping of the sample.

Sample	E_{SSB}-E_F [eV]	E_{CBM}-E_F [eV]
pristine	0.29	0.15
3% Mn	0.34	0.15
2.5% V	0.33	0.17

Table 5.1: Positions of the band bottoms of the surface state (SSB) and conduction band (CBM) in relation to the Fermi energy for the three different investigated samples. The values were obtained by fitting the integrated DOS, as presented exemplarily in Fig 5.5.
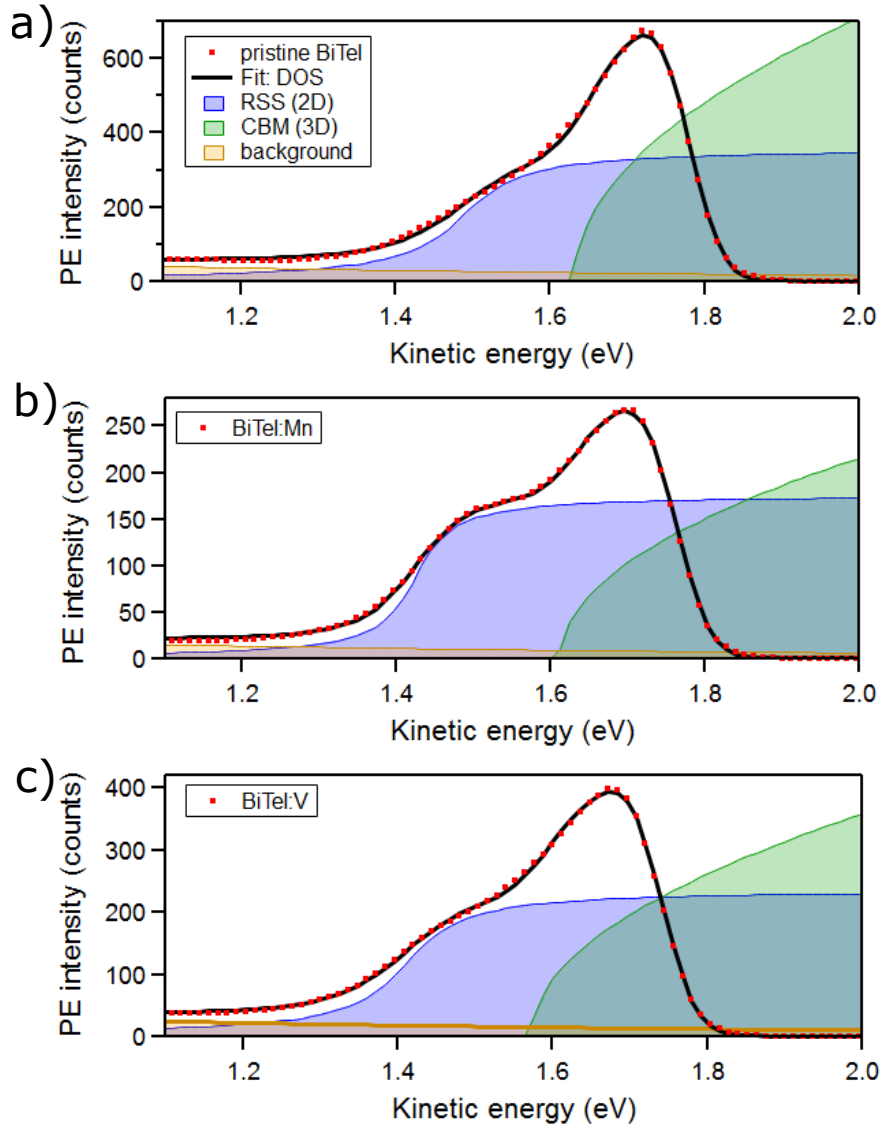
Figure 5.5: Integrated PE intensity of the pristine (a), the Mn-doped (b) and the V-doped (c) BiTeI sample (red). The spectra were fitted with a function comprising of a squareroot to account for the bulk DOS (green), an arcus tangens to account for the lifetime-broadened surface DOS (blue) and an exponential background (orange). These where multiplied with a Fermi function to model the Fermi edge and convoluted with a gaussian to account for the resolution. This yields the actual fit function (black).

In summary, doping BiTeI with generous amounts of Mn and V does not significantly alter the dispersion of the bands close to the Fermi level on the Te-terminated surface. The dispersion of the bands of our Mn-doped sample is in excellent agreement with reported dispersions [34, 78]. Qualitative comparison shows similar dispersions on the pristine and V-doped sample, albeit the spectra have lower quality, especially in the pristine case. Quantitative evaluation of the band positions reveals that the band bottom of the CB is situated at very similar binding energies for all three samples, while the RSSs show slightly higher binding energies on the doped samples.

5.2 Carrier Dynamics on the Te-Terminated Surface of BiTeI

In this section, I will present our results on the electron and hole dynamics in the RSS and CBM of the Te-terminated surface of BiTeI after photoexcitation with $1.5\,\mathrm{eV}$ photon energy.

To our knowledge, the only previous work discussing electron dynamics on BiTeI has been published by Mauchain *et al.* [111]. This work features a qualitative discussion of the electron dynamics in BiTeI, focussing on the first couple of hundred femtoseconds after excitation. Furthermore, spectra recorded with either circular polarized pump or circular polarized probe pulses are discussed.

We expand on this previous work by providing better resolution of the RSS in our time-resolved spectra and discussing the dynamics in much more detail. We will look at some general features like the fundamental k- and E-dependency before discussing the electron (Sec. 5.2.1) and hole (Sec. 5.2.1) dynamics of the pristine sample and then comparing to the doped samples (Sec. 5.3).

Our results regarding circular dirchoism in the angular distribution (CDAD) on BiTeI are presented in Sec. 5.4 and compared to Mauchain *et al.*'s results.

Figure 5.6 shows tr-ARPES spectra recorded on BiTeI:Mn at six exemplary delays between the $1.5\,\mathrm{eV}$ pump and the $6.2\,\mathrm{eV}$ probe pulse. Before the pump pulse arrives at the sample (t $= -1\,\mathrm{ps}$), during the photoexcitation process (t $= 0\,\mathrm{ps}$) and at four different times after the excitation (t $= 1, 5, 10, 15\,\mathrm{ps}$). We can see, that before photoexcitation the spectrum corresponds to the unpumped case (*cf.* Fig. 5.3), as one would expect. During and right after the excitation process, the intensity of all occupied features decreases significantly, most prominently in the CBM, at binding energies up to $0.1\,\mathrm{eV}$. At the same time, we gain PE intensity above E_F, stemming from the excited electrons. The relaxation of the carriers, *i.e.* the recovery of the initial signal, takes place on a picosecond timescale.

While the bulk states and the RSS dispersions below the Fermi edge are clearly discernible at all times, the statistics of the distribution of the excited carriers above E_F is not good enough to unambiguously determine the dispersion of the unoccupied parts of the bands.
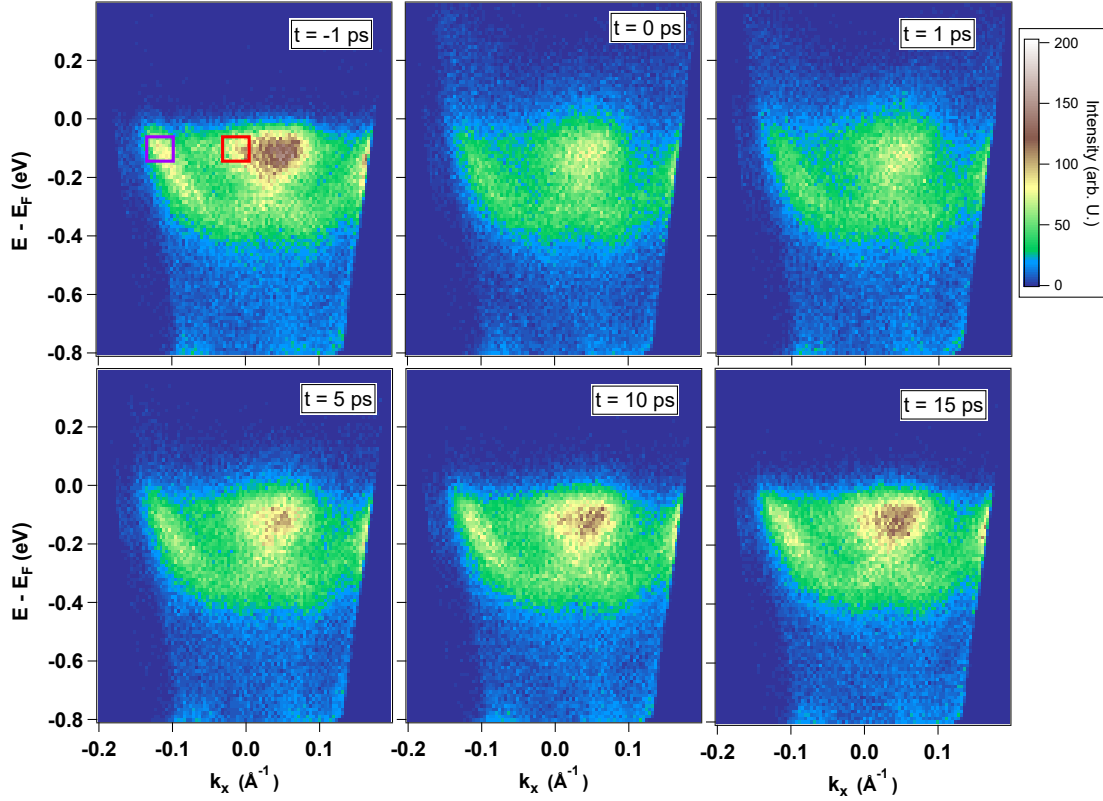
Figure 5.6: PE intensity of the BiTeI:Mn-sample at exemplary times before (t = −1 ps), during (t = 0 ps) and after (t > 0 ps) excitation with an ultrashort laser pulse of 1.5 eV photon energy and a fluence of $150 \, \mu J/cm^2$. During the measurement, the sample was kept at 60 K. Each spectrum was recorded with an exposure time of five minutes. The RSS and bulk bands are clearly discernible at all times, but their intensity decreases significantly during the pump process and then recovers on a picosecond timescale. The boxes in the first spectrum indicate the (k,E)-regions, from which the spectra in Fig. 5.7 were obtained.

As the dynamics within the first couple of hundred femtoseconds after excitation have already been discussed by Mauchain *et al.* [111], we decided to focus our study on the carrier relaxation, *i.e.* the dynamics taking place over the picosecond timescale. We therefore mainly recorded spectra with 100 fs stepwidth and a total duration from roughly 1 ps before to 11 ps after the excitation process. We chose to record the full delay spectra with an exposure time of 3 seconds per delay and integrated over nine separate runs, recorded back to back, as a compromise between feasible recording times and a sufficient signal-to-noise ratio. Meanwhile, the spectra shown in Figure 5.6 were each recorded with an exposure time of five minutes at a pump fluence closely below the damage threshold of the sample. To record a full range of delay spectra with such long exposure times is hardly feasible, as a full scan would require a recording time of ten hours or more.
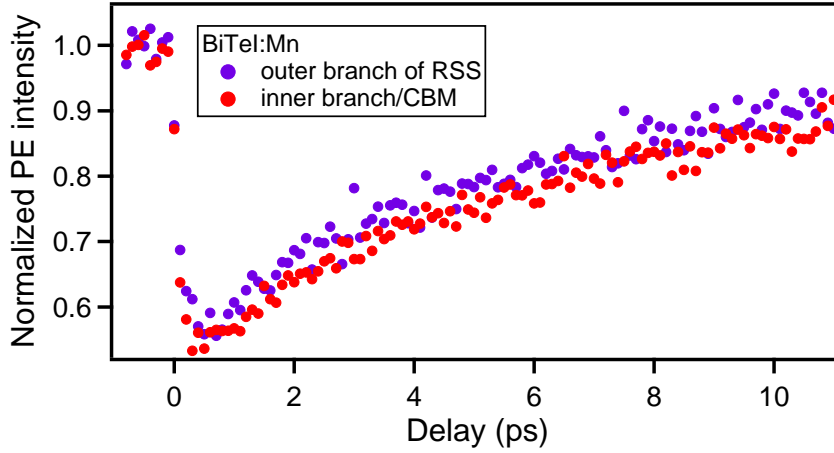
Figure 5.7: PE intensity of the Mn-doped BiTeI sample over pump-probe delay. The spectra were integrated over small sections of $k_{||}$ and energy at two different regions of interest around 100 meV binding energy (indicated by the colored boxes in Fig. 5.6): The outer branch of the RSS (violet) and the inner branch, overlapped by the CBM (red). The spectra were normalized to the intensity before the pump process. I have chosen spectra that were recorded on the same sample and under the same conditions as the spectra presented in Fig. 5.6. When comparing to corresponding spectra derived from other datasets, we see that the deviations between the two presented ones are not systematic.

As the full delay scans yield PE spectra over four independent variables, namely $(k_x, k_y, E_{kin}, \Delta t)$, it is crucial to carefully analyze the dependence on each one of them, before altering additional experimental variables as the sample temperature or the pump fluence.

The first surprising result in this regard, is the fact that the dynamics on neither of the samples show significant dependence on either $k_{||}$ direction. This is shown exemplarily in Fig. 5.7: We have plotted the PE intensity integrated over two small sections of (k_x, k_y, E_{kin}), namely at the inner and outer branches of the RSS at $E_B \approx 0.1$ eV, over the pump-probe delay, normalized to the intensity before the arrival of the pump pulse. One can see that the intensity decreases significantly directly after the excitation and then recovers on the already mentioned picosecond timescale. Thereby, the decrease and recovery of PE intensity recorded at the outer branch of the RSS and the intensity of the inner branch and the CBM show no significant differences. This k-independence is observable at all energies and pump fluences respectively. As we will see later, we would expect significantly longer lifetimes of the photoholes in the outer branches, as compared to the inner branches [121, 123]. A possible explanation for this discrepancy is elastic or quasi-elastic scattering at high rates, probably in the low fs regime, which would lead to a constant redistribution of the electrons in $k_{||}$ without changing their energy. At high temperatures, this process can be electron phonon scattering, in which the absorption and emission of phonons goes with n_{ph} and $n_{ph} + 1$ respectively, n_{ph} being the phonon population. Other partners for elastic scattering are defects within
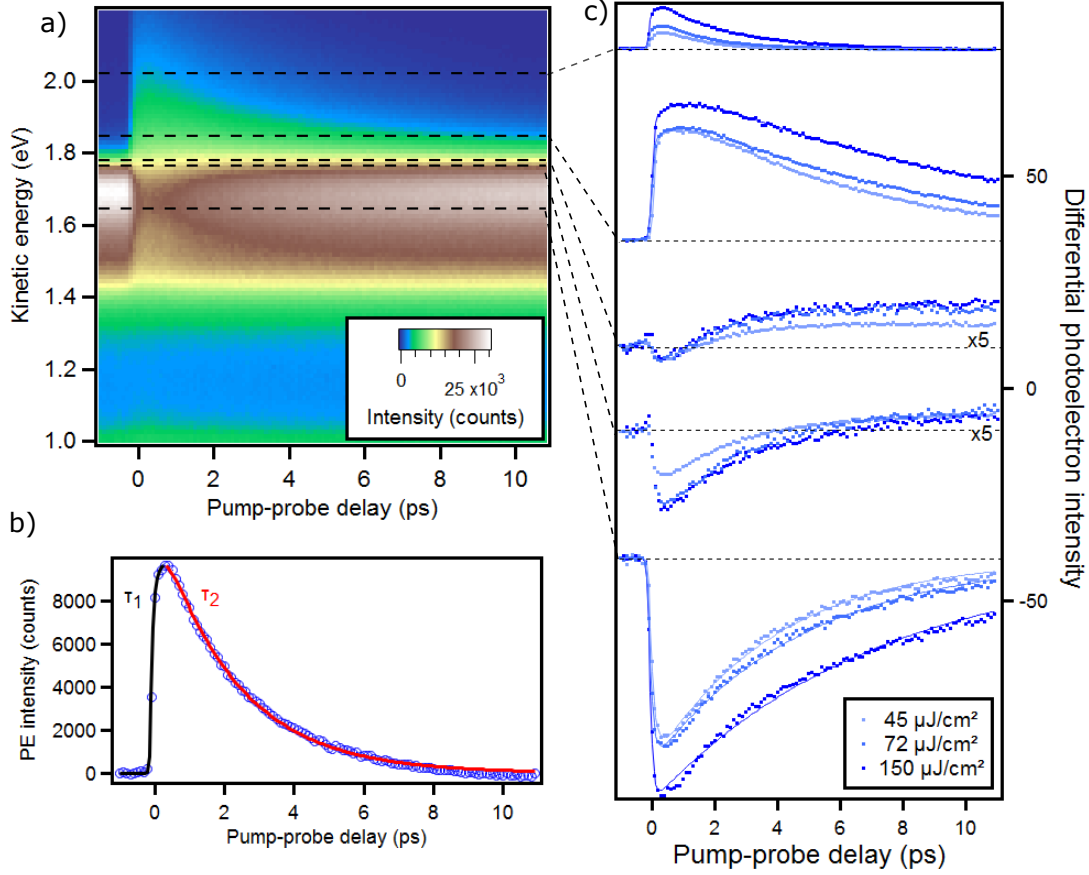
Figure 5.8: a) PE intensity of the BiTeI:Mn sample, plotted over binding energy and pump-probe delay. The intensity was integrated over the entire accessible $k_{||}$ range. The spectrum was recorded at a temperature of $60\,\mathrm{K}$ with a pump fluence of $150\,\mu\mathrm{J/cm^2}$.

b) Exemplary delay spectrum at a single kinetic energy bin ($\Delta E = 12\,\mathrm{meV}$) at the highest indicated energy in a), with the corresponding fit. The fit function, used to fit all delay spectra, contains two exponential functions, one to account for the thermalization after the excitation (time constant τ_1, *cf.* Mauchain *et al.* [111]) and one to account for the relaxation back to the initial distribution (time constant τ_2). The exponential functions are multiplied with a step function to represent the excitation process and folded with a gaussian to model the temporal resolution of our experiment, given by the cross-correlation of the two laser pulses. c) Delay spectra and fits recorded with three different pump fluences at the energies indicated by dashed lines in a). The points represent the measured data, while solid lines are corresponding fits. The traces around the Fermi level have been multiplied by a factor of 5 for clarity.

the crystal structure, such as the boundaries of regions with different stacking sequence, dopants, iodine atoms on Te-crystal sites, general irregularities in the crystal structure and surface contaminants. As all defect states are spatially localized, they can redistribute momentum very efficiently.

In the further evaluation, we will exploit this k-independence by integrating the spectra of each individual measurement over the entire accessible $k_{||}$-range in order to further improve the signal-to-noise ratio.

Next, we want to look at the evolution of the carrier distribution with respect to the binding energy. Fig. 5.8a) shows a false color plot of the PE intensity over binding energy and pump-probe delay, recorded on the BiTeI:Mn sample at 60 K and with 150 μJ/cm^2 pump fluence, then integrated over the entire accessible $k_{||}$ range. As we have seen in Fig. 5.6, the intensity of the occupied features decreases during the excitation, while we gain signal above E_F (*cf.* Fig. 5.8b,c). Over the next picoseconds, the intensity above E_F decays, while the intensity below E_F recovers. If we look at the delay spectrum at a single energy bin, *i.e.* a slice of 12 meV width, we get spectra as shown in Fig. 5.8b) (in this case at an energy above E_F): A steep change of intensity during the excitation process, followed by a quick change of signal within the first few hundred femtoseconds (τ_1, represented by the black part of the curve). This is the equilibration time of the excited carriers, which has already been reported by Mauchain *et al.* [111]. The second timescale (τ_2, represented by the red part of the curve) describes the decay of the photoexcited carrier population (electrons above E_F, holes below). Accordingly, we fit the delay spectra at each energy with a function that consists of two exponential decays and a step function, convoluted with a gaussian to account for the time resolution limited by the cross correlation of pump and probe pulse. Fig. 5.8c) shows the differential PE intensity obtained at the energies indicated by the dashed lines in Fig. 5.8a), for three different pump fluences. Even without looking at the quantitative fit results, we can see that τ_2 depends both on the binding energy of the electrons and the pump fluence. Furthermore, the change in signal right around the Fermi edge is much smaller and shows unusual trends comared to 50 meV away from it either towards higher or lower energies.

If we look at the time constants obtained from these fits and plot them over the respective energies, we can achieve a more quantitative understanding of the carrier dynamics. To do so, I will now focus on the pristine sample for the rest of the section, before returning to the doped samples in Sec. 5.3.

Fig. 5.9 shows the time constant τ_2 obtained from the fitting procedure explained above, for a dataset measured on a BiTeI:Mn sample kept at 60 K and pumped with a fluence of 150 μJ/cm^2. We can see, that indeed τ_2, from here on referred to as the decay constant, is in the picosecond range for all recorded energies. It depends on the binding energy of the carriers both above and below the Fermi level, albeit with very different trends: The decay constants of electrons excited above the Fermi level increases towards the Fermi-level in a non-linear fashion, while the decay constants of the holes, *i.e.* the repopulation after the depletion of the occupied bands, increases linearly towards the
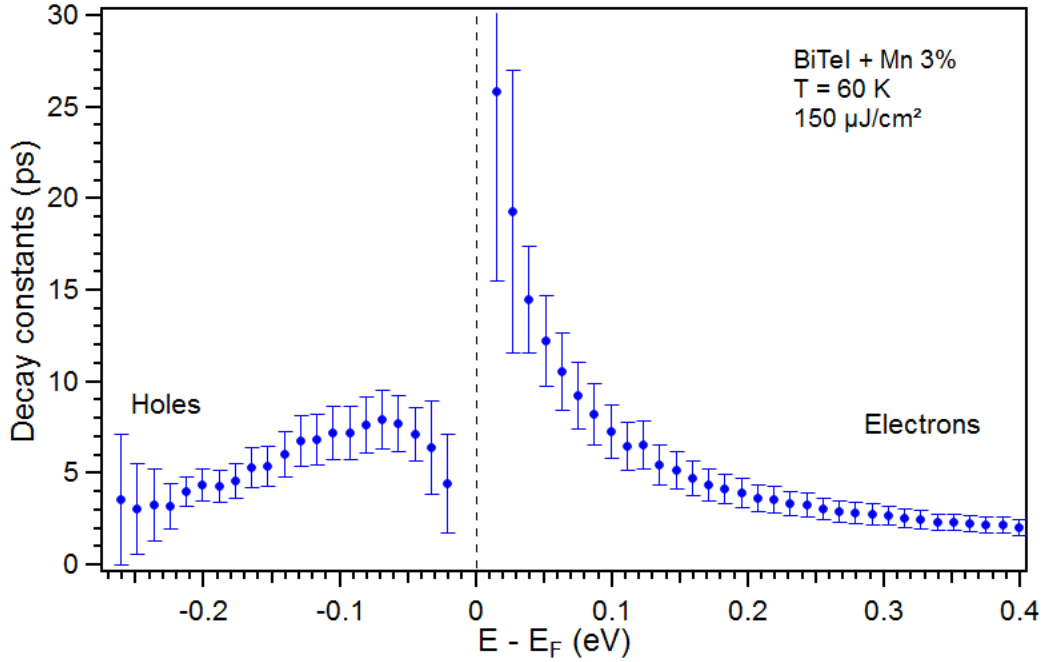
Figure 5.9: Decay constants τ_2, obtained from the fitting procedure explained in Fig 5.8, of the excited electronic system of BiTeI:Mn, plotted over the respective energies. The sample was kept at $60\,\mathrm{K}$ and pumped with a fluence of $150\,\mu\mathrm{J/cm^2}$. The error bars are determined from the robustness of the fits. In most cases, they correspond to 20% of the value, exceptions being the energies next to the Fermi level and within the RSS. Here, the lower quality of the data, mostly because of the reduced change of signal, leads to a larger insecurity of up to 80% of the value. This is true for all presented time constants obtained from the fits, if not stated otherwise.

Fermi level but then drops sharply at low binding energies. As we will see later, these trends generally hold on all three samples. The following sections (5.2.1 and 5.2.2), will discuss these trends on the pristine sample as well as their fluence and temperature dependence in detail. In Sec. 5.3.1 we will return to the discussion of the dynamics of the doped samples and compare.

τ_1, on the other hand, as obtained from the same fits, is fairly independent from the binding energy, mostly lying in the region of a few hundred femtoseconds (not shown, see below). This, by itself, is in good agreement with the results of Mauchain *et al.* [111], who observed a thermal equilibration of the excited carriers by electron-electron scattering within the first 300 fs after excitation. We identify τ_1 as the corresponding time constant and will henceforth call it the equilibration constant. As the spectra presented in Fig. 5.8 are measured with a comparably large step size (100 fs) and the time constants τ_1 and τ_2 show a strong covariance in the fits, we decided to record spectra with smaller time steps over a shorter temporal range. Exemplary delay spectra and
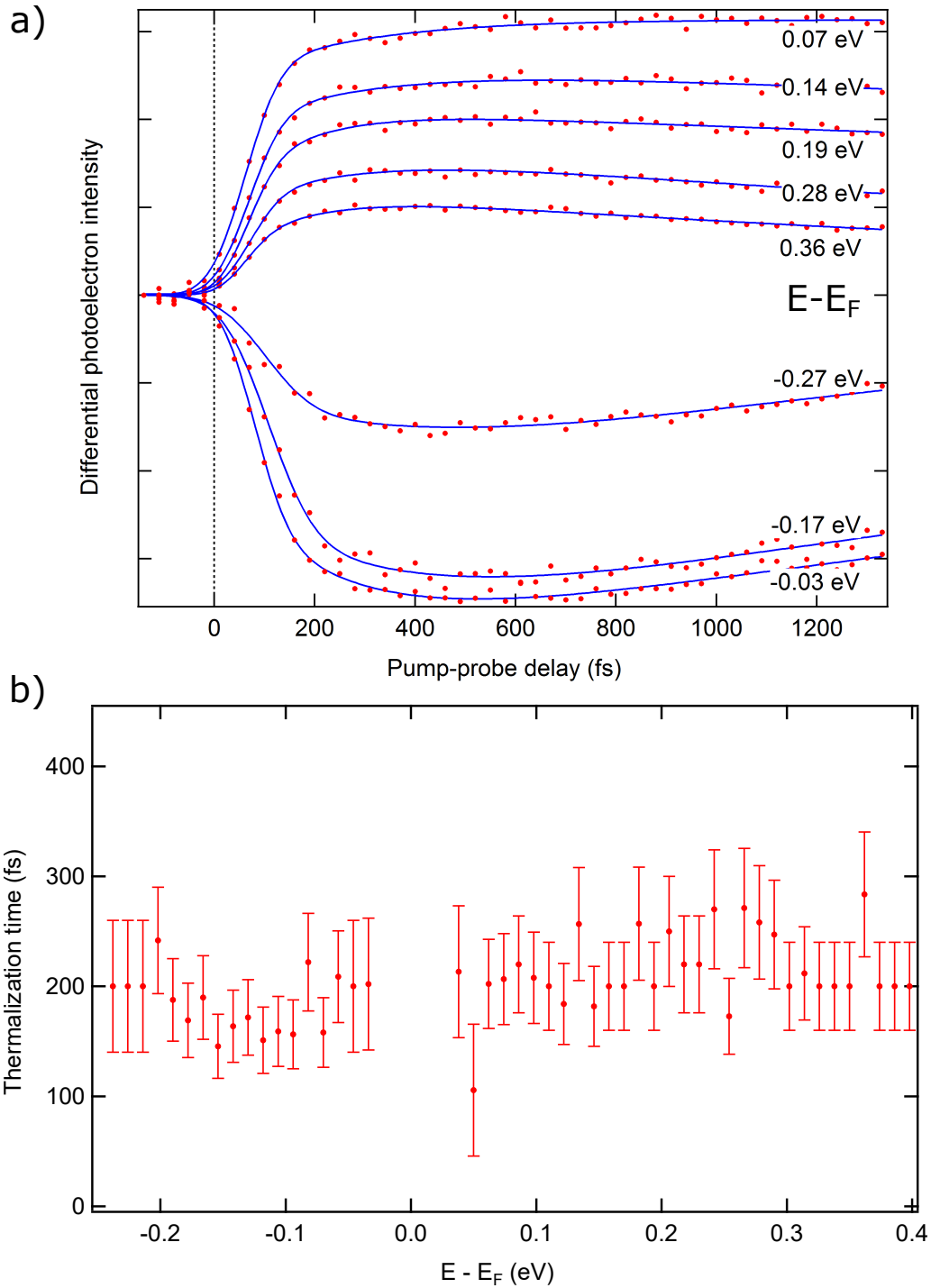
Figure 5.10: a) Exemplary delay spectra of BiTeI:Mn at a range of selected binding energies (red dots), integrated over the entire accessible $k_{||}$ range. The spectra were recorded with a step width of 15 fs over a total range of 1.5 ps and fitted with the function introduced in Fig 5.8 (red lines). The sample was kept at 60 K and pumped with a fluence of $150\,\mu\mathrm{J/cm^2}$. b) Equilibration constants τ_1, obtained from the fits in a), plotted over the respective energies. The error bars are determined from the robustness of the fits, as explained in Fig. 5.9.

their respective fits can be found in Fig 5.10a). Here, we can see that the sharp change of PE intensity described above is acutally smeared out, both due to the rather large cross correlation of our two laser pulses during these experiments ($\geq 120\,$fs, *cf.* 3.2.1) and due to the already mentioned thermalization of the carriers, as described by τ_1. Fig. 5.10b) displays the resulting equilibration constants τ_1, which are clearly energy-independent at a value of $\tau_1 \approx 200\,$fs. The small offset between values below and above the Fermi level is within error bars.

5.2.1 Electron Dynamics

As we have seen so far, the carrier dynamics in BiTeI depends on various factors. Most notably, the energy dependence of the population decay shows different trends above and below the Fermi level. In this section, I will purely focus on the carrier dynamics above the Fermi level, *i.e.* of the electrons, for the pristine sample. The dynamics below, *i.e.* of the photoholes, will be discussed in the next section, followed by a discussion of the influence of the dopants on the dynamics.

Fig. 5.11a) shows the decay constants obtained on pristine BiTeI, by fitting the dynamics above the Fermi level of three different datasets, measured on the same sample, but with three different pump fluences. We can see that for all pump fluences, the decay constant of the electron population increases non-linearly or possibly even diverges towards the Fermi level. This effect becomes stronger when a larger pump fluence is applied. But even far from E_F, the decay times increase with the pump fluence. A more quantitative analysis shows that the decay constants increase more or less linearly with fluence (τ_2 for exemplary energies is shown in Fig. 5.11b), but with an energy-dependent slope. This divergence towards E_F as well as the almost linear behavior of τ_2 with respect to fluence (at least if we suspect to excite carriers over the band gap in the same order of magnitude as the CB is already doped), *i.e.* the number of carriers n, heavily reminds of Fermi liquid theory for a three-dimensional electron gas [87, 145]:

$$\tau_{\text{FL}}(E) \approx 171 \frac{\epsilon_0^{1/2} \hbar^4}{e_0 m_e^{3/2}} \, n^{5/6} \, (E - E_{\text{F}})^{-2} \tag{5.1}$$

Meanwhile, the decay constants displayed in Fig. 5.12, which were obtained from spectra recorded at the same pump fluence, but at RT and 60 K sample temperature respectively, show no significant differences. This again is in line with Fermi liquid theory, which is per se not temperature dependent.
However, with carrier concentrations in the order of 10^{19} cm^{-3} [71, 78, 98], Fermi liquid theory predicts lifetimes τ_{FL}, in the order of tens of femtoseconds in the regarded energetic region, at least two orders of magnitude below the observed decay constants.

This is, in fact, because τ_2 results from an ensemble of hot electrons interacting with the crystal lattice. In order to understand this, we can make the following argument, resting on several findings we already made:
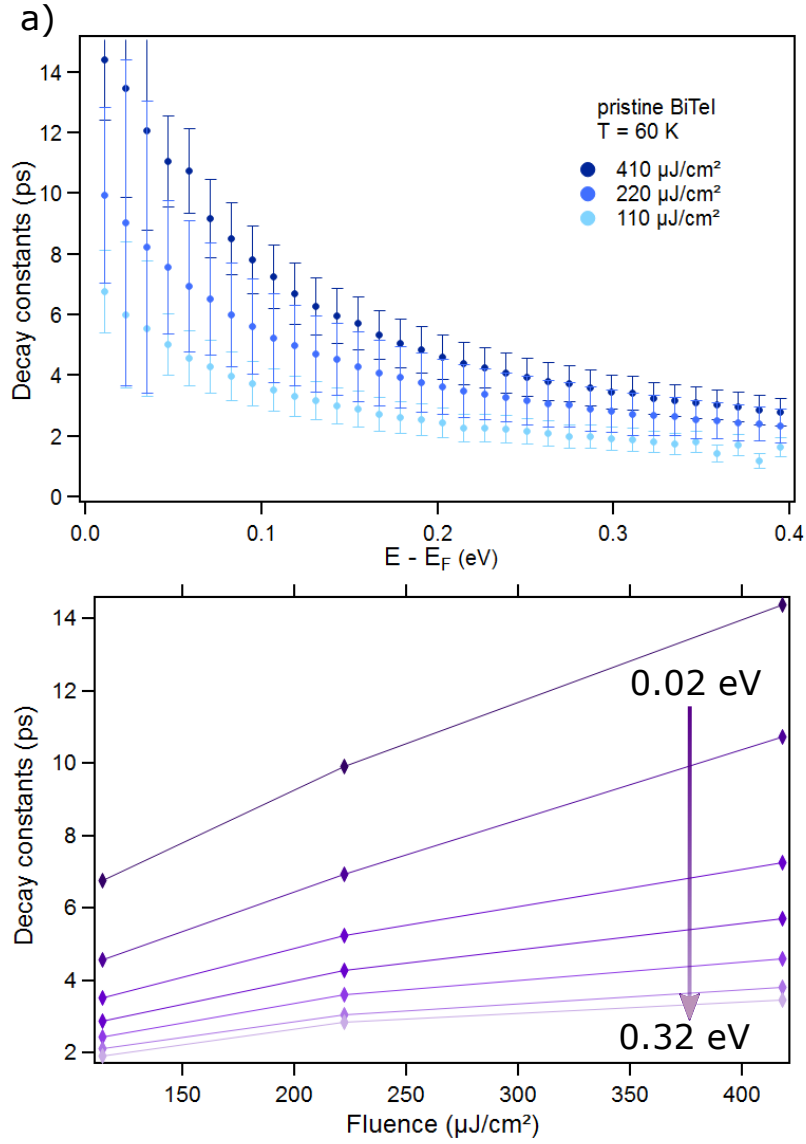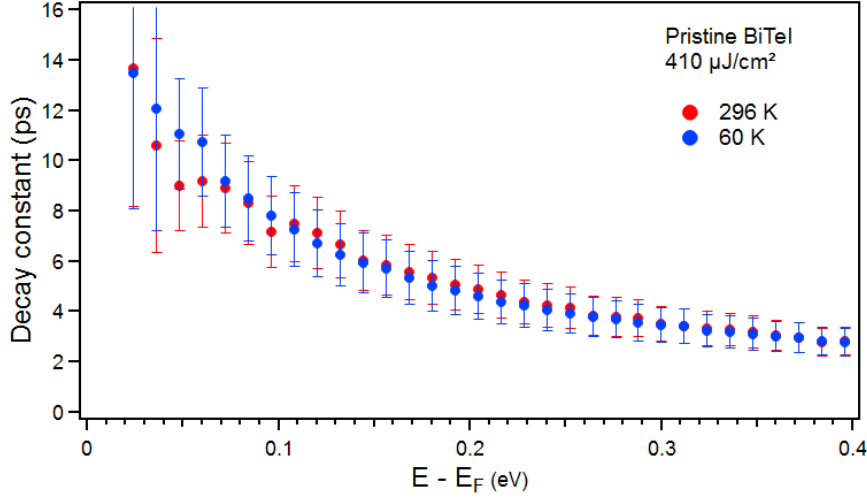
Figure 5.11: a) Decay constants τ_2 of the electrons excited above the Fermi level in pristine BiTeI. The decay constants were obtained as explained in Fig 5.8 from three different datasets measured on the same sample, but with different pump fluences. The sample was kept at 60 K throughout all measurements. The error bars are estimated in the way explained in Fig. 5.9. b) τ_2 plotted over the fluence for selected energies, starting right above the Fermi level ($\Delta E = 50\,\text{meV}$). Error bars are omitted for clarity.

Figure 5.12: Decay constants τ_2 of the electrons excited above the Fermi level in pristine BiTeI. The decay constants were obtained from the fitting procedure explained in Fig. 5.8 from two different datasets measured on the same sample, but at different temperatures. The pump fluence was $420\,\mu\mathrm{J/cm^2}$ in both cases. The error bars are estimated in the way explained in Fig. 5.9.

First, from extrapolation of the DOS fits in Fig. 5.5, the signal is expected to be dominated by bulk contributions in the regarded energetic region, especially on the pristine sample.

Second, the observed broadening of the surface state (*cf.* Fig. 5.5) indeed indicates scattering rates Γ_e in agreement with the predictions of Fermi liquid theory.

Third, the thermal equilibration both above and below E_F, which happens through electron-electron scattering, takes place on a timescale of a few hundred femtoseconds (*cf.* Fig. 5.10), also indicating a high efficiency of that process, *i.e.* high electron-electron scattering rates.

Fourth, and most important, we observe depletion of the occupied bands in the order of several tens of percent (*cf.* Fig. 5.7). This, by itself, might be rather surprising, as the applied fluences are relatively low, compared to fluences needed to induce phase transitions in metals [52, 109, 119, 153]. However, we must not forget that due to the quasi semi-metallic nature of the sample, the DOS at the Fermi level of these samples is orders of magnitude smaller than on a metal. Therefore the required fluence to achieve similar depletion rates is also orders of magnitude smaller than on metals. This is corroborated by other studies on degenerate semiconductors like the TI Sb_2Te_2S, where comparable fluences also have an effect on the electron dynamics, indicating ensemble dynamics [100].

All this together makes it very clear, that τ_2 is the decay constant of an ensemble of hot electrons, not a single particle lifetime, and therefore not describable with Fermi liquid theory. On the contrary, what we observe on BiTeI is the cooling of a hot electron gas,

constantly thermalized by highly efficient electron-electron scattering.

Most commonly, it is assumed that hot electrons will cool by thermalizing with the lattice *via* electron-phonon scattering. This is very likely to be the case for BiTeI as well. Electron-phonon scattering as the main decay channel can also explain the dependency of τ_2 on both the fluence and the sample temperature:

With increasing fluence, we increase the number of excited carriers and therefore the energy that has to be dissipated. In other words, both the peak temperature of the electronic distribution as well as the equilibration temperature with the lattice increase [52]. Therefore the cooling takes longer, which manifests itself in higher decay constants. The independence of the electron dynamics on the sample temperature is a bit less straightforward to understand. From second quantization, we know that the rate Γ_{em} for phonon emission of a single electron, *i.e.* loosing thermal energy to the lattice, is proportional to $n_{ph} + 1$, where n_{ph} is the phonon population at a certain phonon energy. This alone would suggest a faster cooling at a higher lattice temperature. The phonon absorption rate Γ_{abs}, however, *i.e.* gaining thermal energy from the lattice, is proportional to n_{ph}. This makes the overall electron phonon scattering rate $\Gamma_{el-ph} = \Gamma_{em} + \Gamma_{abs} \propto (2n_{ph} + 1)$, which explains the broadening of the spectra at RT. But the dissipation rate $1/\tau_{diss} = (\Gamma_{em} - \Gamma_{abs}) \propto 1$ is independent of the phonon population and therefore from the lattice temperature.

The cooling process by thermalization of the electronic system with the lattice can be modeled by the so-called two-temperature model [4, 23, 109]. In principle, the two-temperature model consists of coupled differential equations for the electronic and lattice temperature, T_e and T_l:

$$C_e(T_e)\frac{\partial T_e}{\partial t} = S(z,t) - H(T_e, T_l) + \frac{\partial}{\partial z}\left(\kappa\frac{\partial T_e}{\partial z}\right) \qquad (5.2)$$

$$C_l(T_l)\frac{\partial T_l}{\partial t} = H(T_e, T_l) , \qquad (5.3)$$

where $C_{e,l}$ are the specific heat capacities, $S(z,t)$ describes the absorbed energy density from the laser, $H(T_e, T_l)$ describes the transferred energy depending on electron-phonon coupling and the last term in the first equation describes dissipation of heat from the electronic system through diffusion, κ being the temperature dependent electronic thermal conductivity.

These equations cannot be solved analytically, but integrated numerically for the respective parameters. The central term $H(T_e, T_l)$, that describes the energy transfer between the electronic and phonon subsystems, depends on the electron-phonon coupling constant γ. Unfortunately, the electron-phonon coupling constant γ has not been determined for BiTeI, at least to our knowledge. Therefore, we will compare our results qualitatively to the predictions of the two-temperature model instead.

Fig. 5.13 exemplarily shows the results of the integration of a two-temperature model: The electronic temperature increases sharply with the incidence of the pump pulse,
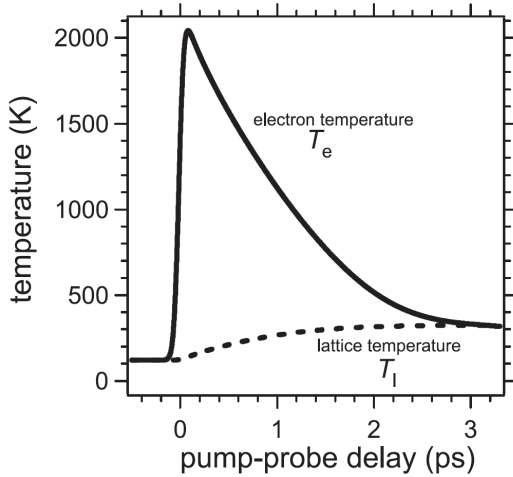
Figure 5.13: Example of electronic and lattice temperature as obtained from the two-temperature model. Figure adapted from [23].

showing little to no delay [4]. However, within the first couple of femtoseconds, the photoexcited electrons in the actual systems will typically not have thermalized yet. As a consequence the predictions in this delay range have to be understood as a theoretical electronic temperature more than an actual observable [23]. After reaching the peak electronic temperature, it decays in a fashion reminiscent of an exponential decay, while the lattice temperature increases. Typically, this increase is even visible on cooled samples, as the involved timescales are much shorter than the lattice heat dissipation and the corresponding therm is omitted from the two-temperature model [23].

As a consequence, the final electronic temperature is slightly increased with respect to the initial value, leading to a slightly broadened Fermi edge and therefore an increased number of carriers above E_F, even at large delays in the picosecond regime. Therefore, electron populations following the predictions of the two-temperature model will show a divergence of lifetimes towards the Fermi edge, reminiscent of the effect we see in our data.

In order to test, how well our data conforms with the two-temperature model, we fitted the DOS for each delay as explained in Fig. 5.5. That means, for each delay, we integrated the photoelectron intensity over $k_{||}$ and plotted the result over the kinetic energy. This was then fitted with a function representing the electronic DOS, which was multiplied with a Fermi distribution and convoluted with a Gaussian to account for the experimental resolution. All spectra were fitted simultaneously, keeping the DOS-parameters equal and only varying the width of the surface state, electronic temperature and chemical potential. One would expect a good agreement of the integrated data with a fit obtained with a broadened Fermi function as soon as the electronic system is in thermal equilibrium. The results are displayed in Fig. 5.14:

From the comparison of the experimental DOS with the fits, we can see, that the electronic distribution is very well matched before the excitation ($\Delta t = -1$ ps) and long after the excitation ($\Delta t = 10$ ps), but can't be perfectly matched during the excitation and even after five picoseconds. This is much longer than expected from the equilibra-
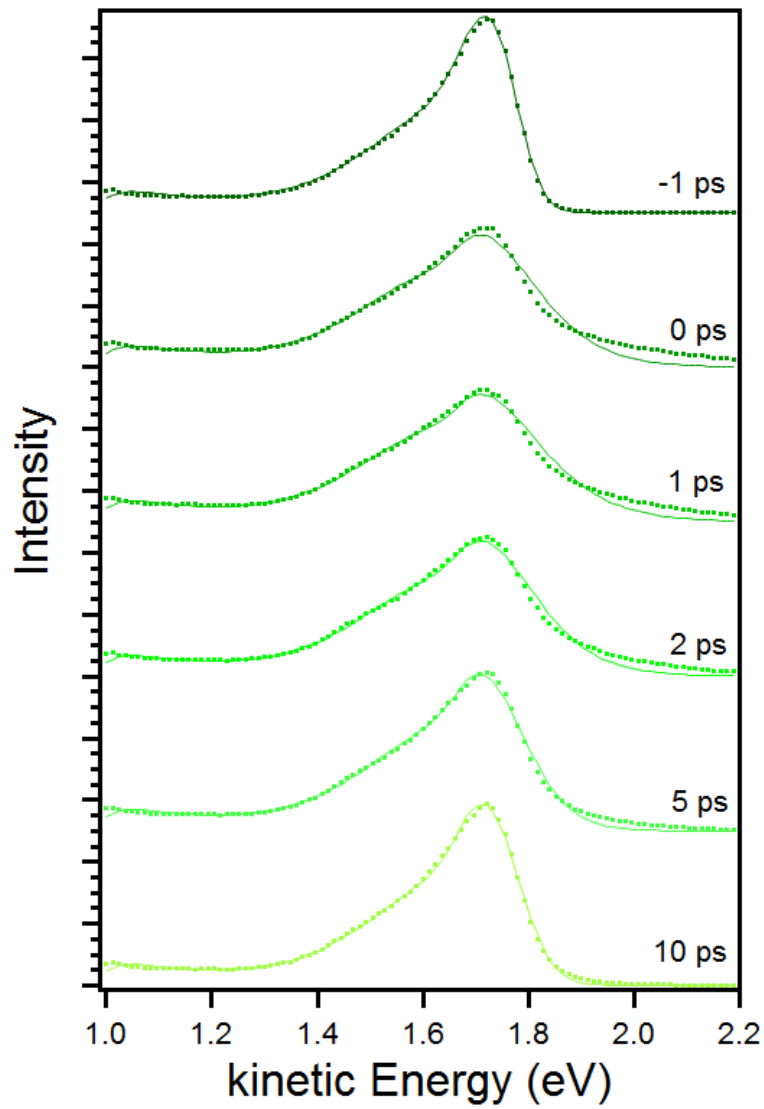
Figure 5.14: The PE intensity recorded on pristine BiTeI plotted over the kinetic energy at five characteristic delays (dots). The data was fitted as explained in Fig 5.5 (solid lines). The sample was kept at $60\,\mathrm{K}$ throughout the measurements and was excited with a fluence of $220\,\mu\mathrm{J/cm^2}$. We see a good agreement of the fits with the data before the excitation and long after the excitation ($\Delta t \geq 5\,\mathrm{ps}$).
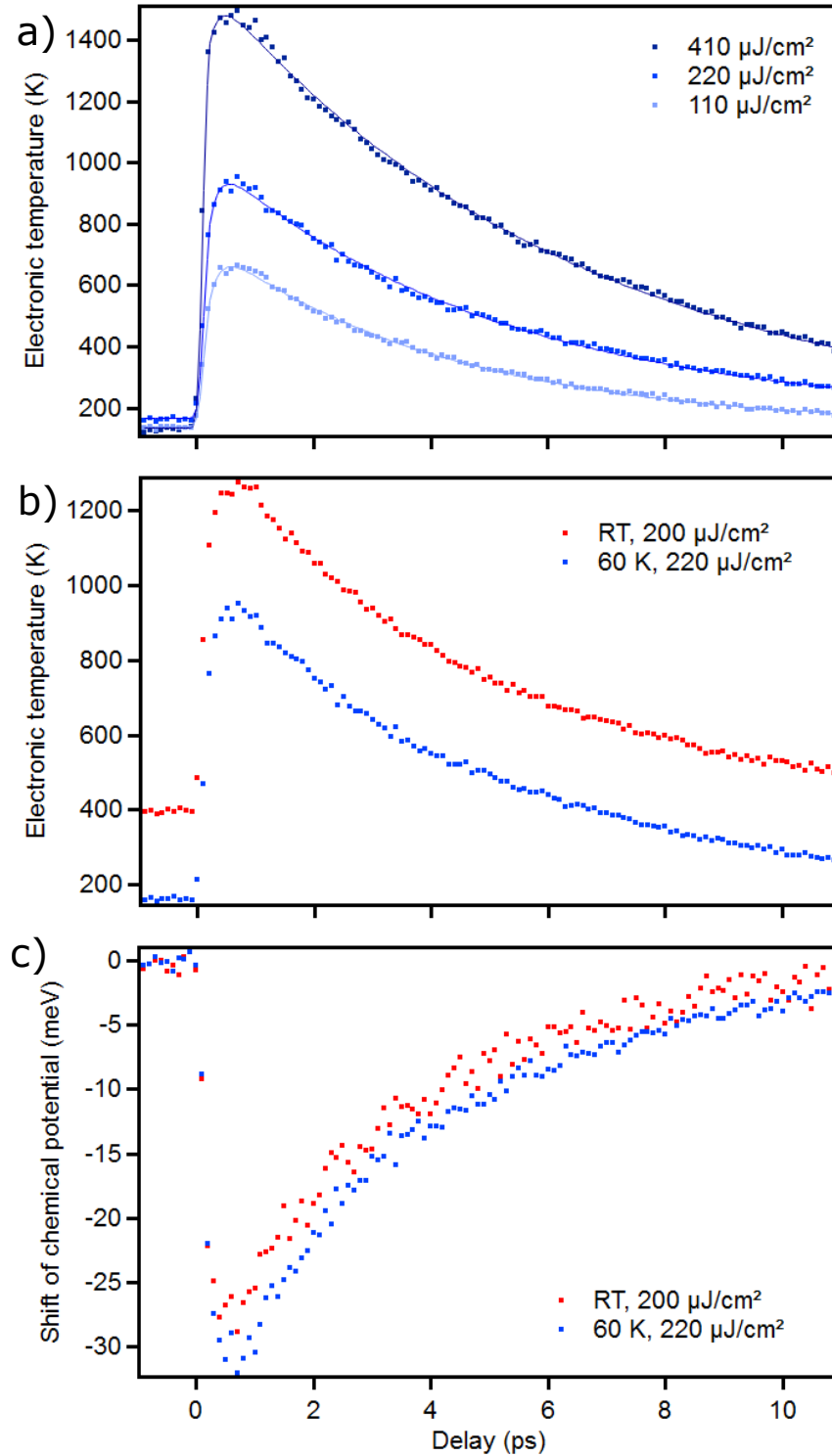
Figure 5.15: a) Electronic temperatures over pump-probe delay, extracted from the Fermi distribution in the fits of the DOS, as exemplarily shown in Fig 5.14. The three curves correspond to temperatures extracted from datasets recorded with three different pump fluences, on a sample that was kept at 60 K throughout all measurements (dots). The solid lines are fits that yield cooling time constants between 4 (light blue) and 6 ps (dark blue). b) Extracted electronic temperatures recorded on a sample at RT (red) and at 60 K (blue), with a fluence of $\approx 220\,\mu$J/cm^2 in both cases. c) Shift of the transient chemical potential of the electrons, simultaneously extracted from the same data as in (b), referenced to kinetic energy of the electrons.

tion constants τ_1, which would suggest that a good match should be achievable after a couple of hundred femtoseconds.

The deviations between the data and the fits are most probably due to the peculiarities of the dynamics below the Fermi level (*cf.* Sec. 5.2.2), which is distinctively different from the dynamics of the carriers excited above the Fermi level. In other words, the hole population does not follow a Fermi distribution, making it impossible to accurately fit both systems with a single Fermi function. Unfortunately, it was not possible to reliably fit the data only above the Fermi level, making it impossible to exclude the influence of hole dynamics from the fit.
Another process adding to the deviations is the excitation of electrons from the valence band (VB) to the CB. These accumulate above E_F, as the recombination across the band gap as well as surface recombination typically take place over several hundreds of picoseconds, as we know from comparable direct band gap semiconductors with small band gaps, like *e.g.* GeSn [184]. This contributes to the increased intensity above E_F that we observe, as compared to the fitted Fermi distributions. It has to be noted that the disagreement between fits and data increases with the applied pump fluence (not shown), which supports this assumption. Despite the explained deviations, we still get a qualitative agreement between data and fit and can therefore still gain some qualitative insights into the evolution of the electronic system by extracting the electronic temperature as well as the position of the chemical potential from the fits.

From Fig. 5.15, we can see that the evolution of the electronic temperature is very reminiscent of the predictions of the two-temperature model, *cf.* Fig 5.13. The only exception are the data points within the first picosecond after excitation, which show an evolution that could most fittingly be described as "too flat". However, as we have already discussed, these data points are the least reliable, as the electronic temperature is ill-defined, as long as the electronic distribution is not fully thermalized yet.
It is notable, that in all cases, the base electronic temperature is systematically overestimated. This is due to the high cross-correlation of this parameter, which influences the width of the Fermi-level, with the resolution of the experiment. We fixed the resolution to a value that yielded the proper electronic temperatures when fitting purely the DOS before the unpumped system. However, the all-at-once fit used to extract the electronic temperatures from the time resolved data still seems to systematically over-estimate the electronic temperature by $100 - 120\,\mathrm{K}$.

As we have already mentioned, the trends of fluence and temperature dependence are very much in line with electron-phonon scattering as the dominant relaxation process. Looking at the corresponding temperature evolutions, we can now discuss these trends more quantitatively in terms of the two-temperature model.

An increase of fluence leads to higher peak electronic temperatures and to longer cooling time scales (*cf.* Fig. 5.15a). The first effect can easily be quantized by looking at the

electronic specific heat [76]

$$C_e \approx \frac{\pi^2}{3} \mathrm{DOS}\,(E_\mathrm{F})\, k_\mathrm{B}^2\, T_e\ , \tag{5.4}$$

As one can see, the electronic heat capacity goes linearly with the electronic temperature T_e. If we now consider Eq. 5.2, we can assume, that the peak electronic temperature mainly depends on the initially deposited energy density E_abs described by the term $S(z,t)$. The absorbed power is proportional to the incident fluence F

$$E_\mathrm{abs} = \epsilon F \tag{5.5}$$

where ϵ contains the absorption coefficient, the illuminated area and the penetration depth of the pump pulse. Furthermore, we know from Eqs. 5.2 and 5.4 in terms of the absorbed energy density

$$\tilde{E}_{abs} = \int_{T_\mathrm{init}}^{T_\mathrm{max}} C_e \mathrm{d}T_e \propto \Delta T_{e,\mathrm{max}}^2 \tag{5.6}$$

and therefore

$$\Delta T_{e,\mathrm{max}}^2 \propto F\ , \tag{5.7}$$

which is not the case, as one can see from Fig. 5.15a). Instead, we observe a sub-quadratic scaling law. This can only be explained by initial fast dissipation of energy from the electronic system. A likely candidate is an initial fast thermalization with the subsystem of optical phonons close to the Γ point. As BiTeI posesses a polar crystal lattice, the so-called Fröhlich modell states that the interaction goes with $1/\mathbf{q}$, where $\mathbf{q}$ is the phonon momentum, and that only longitudinal phonons are excited [35].
However, the peak temperatures of the hot electron gas are in the same order of magnitude as achieved on metals for fluences that are one to two orders of magnitude larger [52, 109, 119, 153]. This is easily explained with the small electronic DOS of a degenerate semiconductor at the Fermi level, as compared to a metal, as we have already discussed in the context of depletion rates regarding Fig. 5.7. This makes the energy required to reach a certain electronic temperature a lot smaller, as it massively decreases the absolute heat capacity of the electronic system at the Fermi level, *cf.* Eq. 5.4, as $\mathrm{DOS}(E_\mathrm{F})$ is proportional to the carrier density n.

The initial sample temperature corresponds to the base temperature of the electronic system, *i.e.* the temperature before excitation. Therefore, the electronic temperature evolution recorded with the same fluence at a different sample temperature will be offset by the initial temperature (*cf.* Fig. 5.15b). However, as the sample temperature is close to the Debye temperature $\theta = 87\,\mathrm{K}$ [186] in the cooled case and much larger at room temperature, we can assume a model where all acoustic phonons are populated even at low temperatures and that the phonon specific heat is constant and independent of temperature [76]:

$$C_l \approx 3 k_\mathrm{B}\, r\, \frac{\mathrm{N}}{\mathrm{V}}\ , \tag{5.8}$$

where k_B is the Boltzmann constant, r is the number of particles per unit cell and N/V is the density of unit cells. Therefore, Eq. 5.3 only depends on the difference between lattice and electronic temperature *via* the term $H(T_e, T_l) = \gamma (T_e - T_l)$ making the dynamics nearly independent of the initial lattice temperature.

Furthermore, we can use Eq. 5.8 to estimate the final lattice temperature from the maximum electronic temperatures, or at least its order of magnitude. The relation between initial and final temperature as well as the deposited energy density $\tilde{E}_{\mathrm{dep}}$ is given by

$$\tilde{E}_{dep} = \int_{T_{\mathrm{init}}}^{T_{\mathrm{fin}}} C_l \mathrm{d}T_l \ . \tag{5.9}$$

As an upper limit for the deposited energy, we can assume the energy initially absorbed by the electrons, $\tilde{E}_{dep} \leq \tilde{E}_{abs}$. With Eqs. 5.4 and 5.6, we obtain:

$$\tilde{E}_{abs} = \frac{\pi^2}{3} \mathrm{DOS}\left(E_{\mathrm{F}}\right) k_{\mathrm{B}}^2 \Delta T_{e,\max}^2 \tag{5.10}$$

and therefore with Eqs. 5.8 and 5.9

$$\Delta T_l = \frac{\tilde{E}_{dep}}{C_l} \leq \frac{\pi^2 \mathrm{DOS}\left(E_{\mathrm{F}}\right) k_{\mathrm{B}}^2 \Delta T_{e,\max}^2}{9 k_{\mathrm{B}}\, r\, \mathrm{N/V}} \ . \tag{5.11}$$

If we now insert the bulk density of states

$$\mathrm{DOS}\left(E_{\mathrm{F}}\right) = \frac{(2m*)^{3/2}}{2\pi^2 \hbar^3} E_{\mathrm{F}}^{1/2} \approx 10^{39} \frac{1}{\mathrm{J\,cm}^3} \ , \tag{5.12}$$

where we have used $m* \approx 0.19 m_e$ [186], as well as $\Delta T_{e,\max} \leq 1350\,\mathrm{K}$ and a typical particle density of $r\,\mathrm{N/V} \approx 10^{-22} \mathrm{cm}^{-3}$ yields $\Delta T_l \approx 3\,\mathrm{K}$, even at the highest applied fluence.

We therefore can see from Fig. 5.15, that even after $11\,\mathrm{ps}$, the electronic system has not yet equilibrated with the phonon bath, as it retains temperatures in the order of $10^1 - 10^2\,\mathrm{K}$, depending on the fluence. This is very puzzling, as *e.g.* the fluence dependence suggests, that we have to assume, that the scattering with the optical phonons close to the Γ-point is very effective, as theory predicts for a polar lattice [35].

A possible explanation for this is a phonon bottleneck:

Even though scattering with acoustic phonons has been found to be very effective in BiTeI in the transport regime [37, 71, 186], it might be less effective for the optically excited hot electron gas that is created by the pump pulse.

In this case, long relaxation times of the excited optical phonons with the remaining phonon population might significantly slow down the dissipation of heat from the electronic system [137, 161]. In other words: The electronic system very quickly thermalizes with the subsystem of optical phonons with small q, on a timescale in the same order of magnitude as electron-electron scattering. Meanwhile, scattering with the remaining

phonon population is much less effective, not faster than on a picosecond timescale. The same is true for the decay of the excited phonon subsystem.

From Fig. 5.15c) we can furthermore see that the chemical potential shifts with the electronic temperature to smaller energies, as one would expect. Note that this is purely a shift of the chemical potential, the band positions remain constant (*cf.* also Appendix C). The chemical potential μ as a function of temperature (at least in the approximation of low temperatures) is given by [61]:

$$\mu(T) = E_{\mathrm{F}} - \frac{\pi^2}{6} \, (k_{\mathrm{B}} T_e)^2 \, \frac{\mathrm{DOS}'(E)}{\mathrm{DOS}(E)} \; , \tag{5.13}$$

and therefore

$$\Delta\mu = \frac{\pi^2}{12} \left[(k_{\mathrm{B}} T_{\mathrm{base}})^2 - (k_{\mathrm{B}} T_{\mathrm{max}})^2 \right] \frac{1}{E_{\mathrm{F}}} \; . \tag{5.14}$$

With base temperatures of $k_{\mathrm{B}} T_{\mathrm{base}} \approx 5 \, \mathrm{meV}$ and maximal temperatures in the order of $k_{\mathrm{B}} T_{\mathrm{max}} \approx 80 \, \mathrm{meV}$ (at $60 \, \mathrm{K}$ sample temperature and a fluence of $220 \, \mu\mathrm{J/cm^2}$), and a surface Fermi level of approximately $150 \, \mathrm{meV}$ above the band bottom, we would expect a shift of $33 \, \mathrm{meV}$, which matches the observed shift extremely well.
However, with such a low Fermi level, the approximation above is not reliable. A numerical integration of the Fermi function [96] yields a shift of approximately $60 \, \mathrm{meV}$, a factor of two larger. This discrepancy is not surprising, as the matching between fits and data is not perfect (*cf.* Fig. 5.14).

Another possible mechanism that we haven't discussed so far, that can seemingly dissipate energy from the observed hot electron gas, is the diffusion of excited carriers into the bulk of the sample, as included into the two-temperature model by the last term in Eq. 5.2. The thermal conductivity κ of the electronic system is closely related to the electrical conductivity σ *via* the Wiedemann-Franz law [76]. As long as the diffusion rates do not strongly depend on the energy, which they should not, this process is hard to discern from electron-phonon scattering, as it will simply reduce both the equilibration timescales and the final temperature. However, the peculiarities of the polar surface of BiTeI makes a diffusion of electrons into the bulk unlikely. This plays a much more prominent role for the hole dynamics, as we will see in the next section.

5.2.2 Hole Dynamics

In the previous section, we have seen that electron-phonon scattering governs the dynamics of the carriers above the Fermi level. In this section, we will discuss the dynamics of the carriers below E_F, which show a very different energy dependence, namely a linear increase towards E_F instead of a non-linear one, interrupted by a sharp drop right below E_F (*cf.* Fig. 5.9).

The obvious difference between the carriers above and below E_F is, that they are electrons and holes, respectively. However, most materials show symmetric behavior around
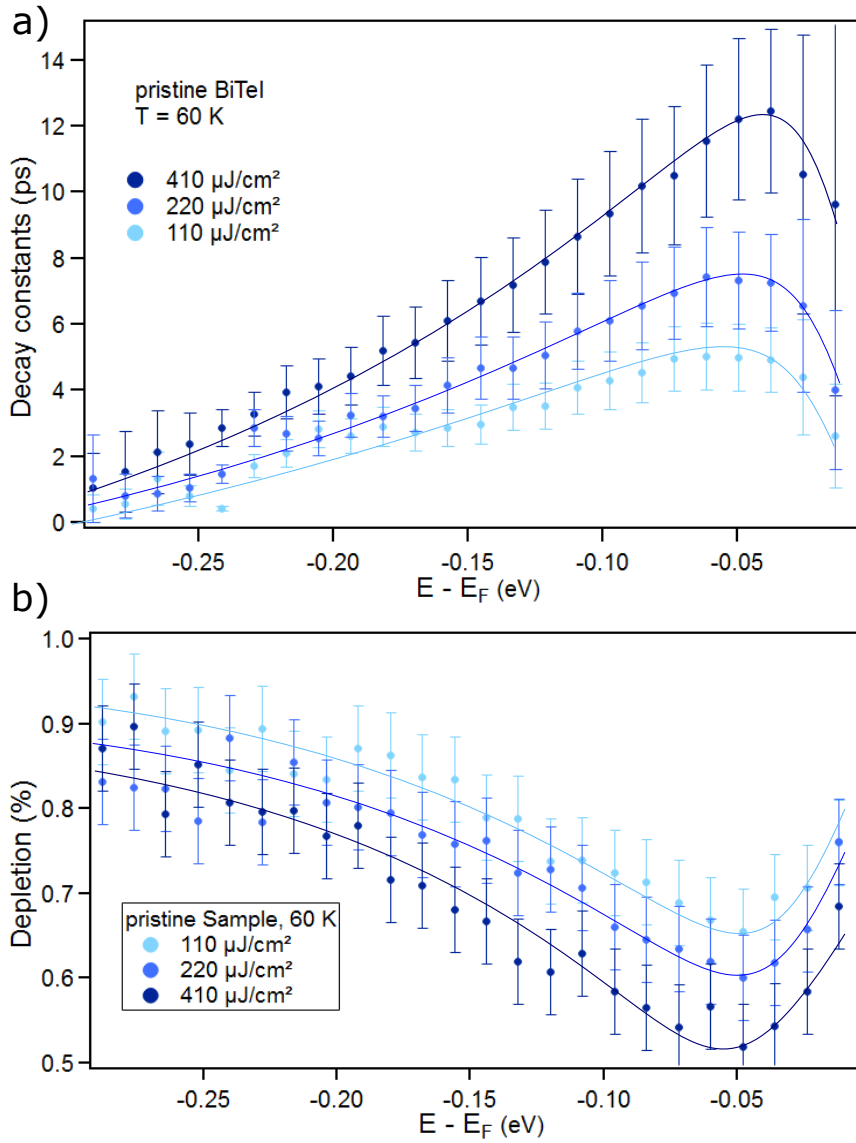
Figure 5.16: a) Decay constants τ_2 of the carriers below the Fermi level in pristine BiTeI. The decay constants were obtained as explained in Fig. 5.8 from three different datasets measured on the same sample, but with different pump fluences. The sample was kept at 60 K throughout all measurements. The error bars are estimated in the way explained in Fig. 5.9. b) The decrease of the PE intensity, *i.e.* the maximum depletion of the bands in percent plotted over energy for the three different fluences. Errors are estimated from the noise level of the raw data. The solid lines in both graphs serve as guide to the eye.

E_F. Therefore, we need to find out, why electrons and holes behave differently on BiTeI. From the DOS fits in Fig. 5.5, we know that the relative contribution of the surface states to the spectra is larger below E_F than above. At binding energies of more than 150 meV, the DOS is even derived purely from the RSS. However, it is hard to predict, how the change of dimensionality alone influences, *e.g.*, electron-phonon coupling as well as the screening of electron-electron interactions, especially since the coupling between surface and bulk states is unknown. To gain more insight, we will now look at the dependencies of the decay constant τ_2 below E_F in more detail.

Fig. 5.16a) shows, how the energy dependence of the decay constant evolves with increasing fluence. While the energy dependence of τ_2 itself below the Fermi level is highly different from the energy dependence above E_F, the fluence dependence is very much the same: With increasing fluence, τ_2 increases in an approximately linear fashion, while the increase is stronger towards the Fermi level. In Fig. 5.16b), we can see that the maximal depletion of the occupied bands, *i.e.* the strongest decrease of the PE intensity is both energy- and fluence-dependent, in line with our considerations of the previous section. Or, in other words, we indeed increase the number of excited carriers with the fluence to a maximum of up to 50% of the total signal. The energetic trend of maximal depletion, which is achieved right after the thermalization, fits with the shape of a Fermi function. The only exception to the latter is the region of very small binding energies, up to approximately 50 meV binding energy, which coincides with the region of the sharp τ_2 drop in Fig. 5.16a).
This general trend, however, shows that we deplete the energetic region below $E_\mathrm{B} = 150$ meV, *i.e.* the RSS in the band gap, much less than the CBM. This indicates, that the absorption cross section for the applied wave length is sufficiently small, for the pump pulse to penetrate deep into the sample, as it is the case on other semiconductors for the used photon energy of 1.5 eV [5, 6]. Even for an absorption coefficient of 10^5 cm^{-1} as in GaAs, only 1% of the absorbed fluence excites the surface.

In order to understand the kinks in both the decay constants and depletion rates, we need to remind ourselves of the peculiarities of the Te-terminated surface of BiTeI. As we have discussed in Sec. 5.1, BiTeI possesses polar surfaces with a partial positive charge on the Te-terminated surfaces, accompanied by a partial negative charge on the I-terminated surfaces. These partial surface charges lead to a respective band bending, in order to compensate the charges. While aging decreases the band bending of the I-terminated surface, the band bending of the Te-terminated surface is considered to be unaffected [34, 50]. Therefore in the energy range of the band bending of about 100 meV, a small static field remains, giving rise to a field current of electrons to the surface (*cf.* Fig. 5.17). Or, seen *vice versa*, the static field facilitates the diffusion of photoholes into the bulk. However, this channel is open only for photoholes in the bulk states, *i.e.* the CBM, not for the photoholes in the RSS. This would explain, why the effect only influences the dynamics close to the Fermi level.

We can try to estimate the time scale on which these drift currents take place, if we make some minor assumptions about the material. The drift velocity v_D of the carriers
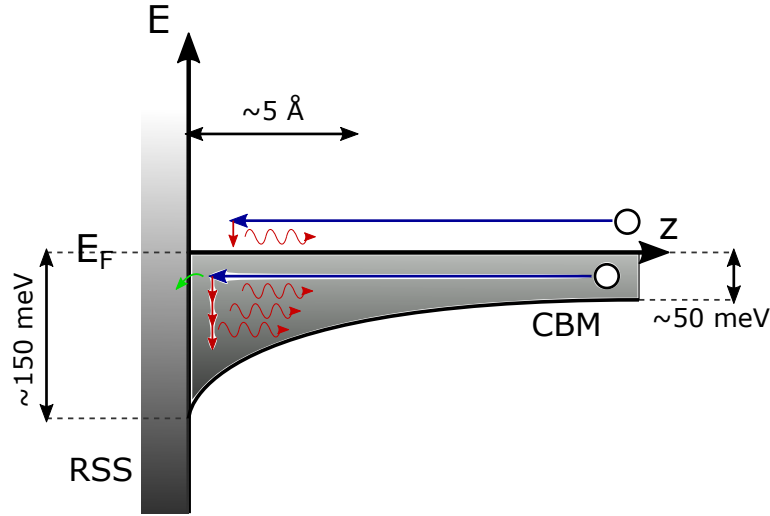
Figure 5.17: Energy scheme of the band bending on the Te-terminated surface of BiTeI. The downwards band bending induced by the partial positive surface charge facilitates the transport of electrons towards the surface (blue arrows), where they accumulate around E_F until they can relax by phonon emission (red arrows) or surface recombination (green arrow).

is given by their mobility μ multiplied with the electric field:

$$v_D = \mu E . \tag{5.15}$$

From measurements of the conductivity and Hall voltage, the mobility of carriers in BiTeI was determined to be in the order of $2 \times 10^{-2}\,\mathrm{m}^2/\mathrm{Vs}$ at RT and $5 \times 10^{-2}\,\mathrm{m}^2/\mathrm{Vs}$ at $77\,\mathrm{K}$ [37, 98]. These values are valid for movement of the electrons within the TL. As the conductivity along the stacking axis is half as large as within the planes [71], the mobility of carriers is probably equally halved. Furthermore, we can try to estimate the electric field caused by the band bending: From [47], we know that the difference in potential on the clean Te-terminated surface is approximately $0.23\,\mathrm{eV}$ over a depth of roughly $10\,\text{Å}$ (*cf.* Fig. 5.1). However, the bottom of the CBM is situated at approximately $0.15\,\mathrm{eV}$ binding energy. From typical carrier densities in the bulk [37, 98, 186] and the effective mass $m* = 0.19\,m_e$ [186], we can assume that the Fermi level in the bulk lies at $0.05\,\mathrm{eV}$, coinciding with the position of the kink. Therefore, the remaining potential difference is on the order of $0.1\,\mathrm{eV}$.

If we insert all these values, we gain drift velocities on the order of $v_D \approx 10^6\,\mathrm{m/s}$. This means, the holes would cover the $10\,\text{Å}$ of the band bending within a femtosecond, indicating ballistic transport. With the applied photon energies, we are possibly sensitive to the whole depth of the band bending (*cf.* Sec. 3.1.1).

Once arrived at the surface, the electrons can only decay via phonon emission, leading to the observed decay constants. The residual depletion right below the Fermi level of approximately 10% corresponds to the depletion of the RSS at higher binding energies. It therefore stems from the depletion of the RSS in combination with the limited surface recombination rate.
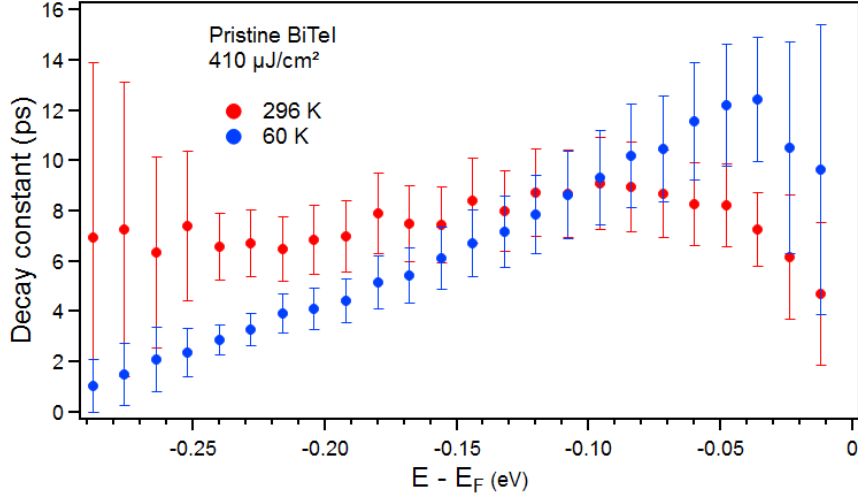
Figure 5.18: a) Decay constants τ_2 of the carriers below the Fermi level in pristine BiTeI. The decay constants were obtained from the fitting procedure explained in Fig 5.8 of two different datasets measured on the same sample, but at different temperatures. The pump fluence was $410\,\mu\text{J/cm}^2$ in both cases. The error bars are estimated in the way explained in Fig. 5.9.

The temperature dependence of τ_2 is extremely different above and below E_F (*cf.* Fig. 5.18a): Unlike the dynamics above E_F, which show no significant temperature dependence at any energy, the electron dynamics below E_F are highly temperature-dependent. The trend itself stays the same - a linear increase towards the Fermi level with a sharp drop at very low binding energies - but the slope is significantly flatter at RT, leading to an almost energy-independent τ_2 at binding energies above $50\,\text{meV}$. More precisely, at RT the relaxation at high binding energies (more than $0.1\,\text{eV}$, *cf.* also Fig. 5.18b) is slower, while the relaxation at low binding energies is faster than at a sample temperature of $60\,\text{K}$. This leads to a crossing point of the two trends, which lies at approximately $0.1\,\text{eV}$ binding energy. Even though for both temperatures, the slopes and offsets of τ_2 change with the fluence (*cf.* Fig. 5.16a) for the fluence dependence at a sample temperature of $60\,\text{K}$), the crossing point of the two temperature trends stays in the same region independent of fluence.

These peculiar dynamics indicate, that there is a decay channel which is only open at low temperatures. This decay channel has to redistribute electrons from the CBM or the upper branches of the RSS to the bottom of the RSS, in order to reduce the lifetimes of holes at high binding energies and prolong those at low binding energies. One possible candidate for such a channel is the surface plasmon proposed by Nechaev et. al. [47, 121, 122, 124]. Normally, the steep dispersion of surface plasmons makes it impossible for electrons to couple to them. But the peculiar dispersion relation of the RSS would allow a decay of electrons from the inner branch above the DP to the band bottom below the DP *via* plasmon emission, as this interband process would hardly require any momentum transfer (*cf.* Fig. 5.19). The crossing point of the two τ_2 trends
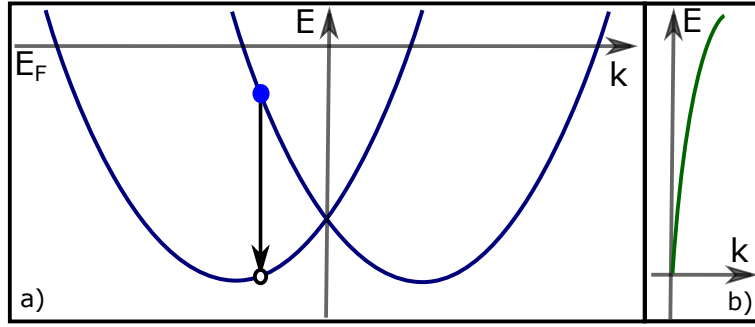
Figure 5.19: a) Schematic of the dispersion of the RSS. The arrow indicates the possible decay channel by plasmon emission: Electrons decaying from the inner branch of the RSS to the band bottom can lose energy to the plasmon with little to no momentum transfer. b) Surface plasmon dispersion, indicated approximately to scale.

would then coincide with the DP of the RSS, which is at least plausible from our data. Unfortunately, the surface states are not well enough separable from the bulk to make a more quantitiative statement.

A closing of the plasmon decay channel at RT, due to increased scattering with optical phonons ($1/\tau \propto 2n_{\mathrm{ph}} + 1$), would lead to a flattening of the energy dependence of the decay constants, explaining our observation.

As electron-phonon scattering would lead to an increase of the lifetimes towards the Fermi level, even at RT, mirroring the trend of the electrons, we can conclude that surface recombination is the major decay channel for the holes in the RSS.

The plasmon decay channel would, however, only be open for carriers in the inner branches of the surface state, in other words neither for the outer branch nor the CBM. This, in turn, would mean $k_{||}$-dependent dynamics, which goes against our observations (*cf.* Fig. 5.7). As we don't observe significant $k_{||}$ dependence of the dynamics, we have to assume that quasi-elastic defect scattering is redistributing the electrons so effectively, that it masks the different dynamics of the different states and branches. In other words, only the dependence of the dynamics on the energy (below and above the DP) remains, while the k-dependence is obscured by quasielastic scattering.

5.3 Effects of Dopants on the Electron Dynamics

It has been proposed, that adding manganese improves the growth of BiTeI without affecting the electronic structure [78]. We therefore investigated, whether it also leaves the carrier dynamics unaffected. To this end, we performed tr-ARPES measurements on BiTeI crystals doped with 2.5% Mn. In addition and as a comparison, we also investigated the influence of vanadium as a dopant by performing tr-ARPES measurements on BiTeI crystals doped with 3% V. Vanadium is a transition metal just as manganese,

but with three electrons in the 3d-shell instead of five. Both elements are known to exhibit ferromagnetic properties, albeit not dispersed within BiTeI at the investigated temperatures.

As we have seen in Sec. 5.1.2, indeed neither 2.5% manganese nor 3% vanadium doping seems to influence the electronic structure of BiTeI in a qualitative way. But both increase the resolvability of the RSS by decreasing the relative strength of the PE signal from the CBM as well as slightly increasing the apparent binding energy of the RSS.

In this section, I present our measurements and findings regarding the influence of the dopants on the electron and hole dynamics in BiTeI. As we have already hinted at in Sec. 5.2, Mn doping does not influence the dynamics in a qualitative way, while V doping has a larger impact. I will therefore discuss the results for the two dopants consecutively.

5.3.1 BiTeI:Mn

As we have already seen in Sec. 5.1.2, the RSS is best resolved on PE spectra recorded on BiTeI:Mn, in comparison to pristine BiTeI and BiTeI:V. We have already discussed that this difference can have different reasons than the seemingly obvious explanation of better sample quality in the doped cases. The main reason to doubt this interpretation is the apparent macroscopic quality of the samples: The doped samples looked significantly more flaky than the pristine sample, while the latter also was much easier to cleave. In addition, the maximal pump fluence applicable to BiTeI:Mn before creating a large background of secondary electrons and damaging the sample irreversibly was significantly lower, namely $\approx 200\,\mu\mathrm{J/cm^2}$ in the doped case versus $\approx 400\,\mu\mathrm{J/cm^2}$ in the pristine case. Such a large background signal of electrons emitted in multiphoton processes also indicates the presence of mesoscopic defects, *i.e.* a rough surface, as the electric field of the pump pulse will be enhanced by plasmons at edges protuding from the sample [1], *e.g.* crystallites of different orientation.
We will tackle the question about the influence of the dopants on the crystal quality from a different angle, namely by comparing the dynamics of hot electrons in both samples and thereby looking for signatures of electron-defect scattering.

In Sec. 5.2, we have already discussed that many general trends of the carrier dynamics after photoexcitation, such as the $k_{||}$ independence of the dynamics and the thermalization of the hot electron gas within a few hundred femtoseconds, are identical for pristine and Mn-doped BiTeI. Now we want to look at the decay constants in more detail.

The energy and fluence dependence of the carrier dynamics, which is depicted in Fig. 5.20a), shows the same general trends as the pristine sample: While the decay constants of the carriers above the Fermi level increase in a non-linear fashion towards E_F, the decay constants below increase in a linear fashion towards, but exhibit a steep drop right below, E_F, again at a binding energy of roughly 50 meV at all fluences.
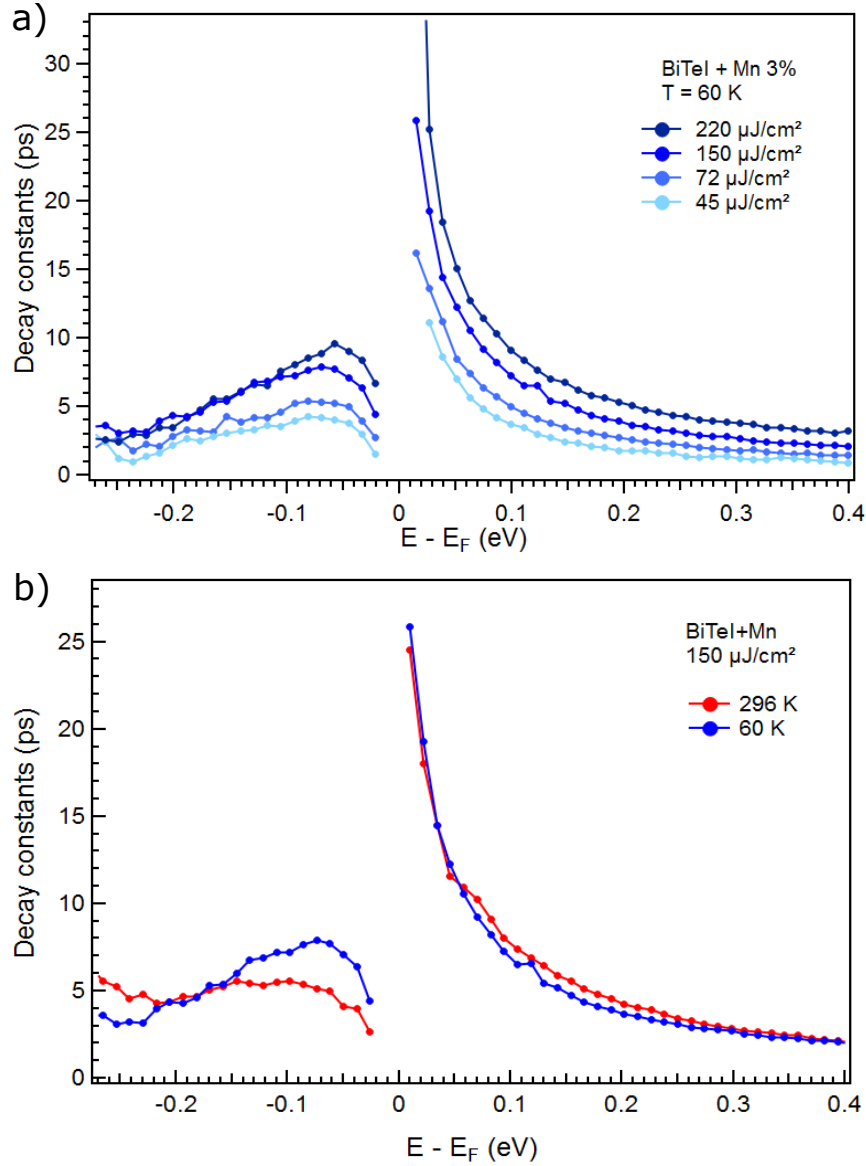
Figure 5.20: Decay constants τ_2 of the carriers in BiTeI:Mn. The decay constants were obtained from the fits explained in Fig 5.8. a) τ_2 at four different fluences. The sample was kept at 60 K throughout all measurements. b) τ_2 from two different datasets measured on the same sample, but at different temperatures. The pump fluence was $150 \, \mu J/cm^2$ in both cases. Errorbars are omitted for clarity, see Appendix C for errors.

Also the temperature dependence, exemplarily shown for a fluence of $150\,\mu J/cm^2$ in Fig. 5.20b), shows the same qualitative behaviour as for the pristine sample: Above E_F, the decay constants are in the same way independent of the sample temperature. Below E_F, the decay constants recorded on a sample at RT have a significantly smaller slope than those recorded at a sample temperature of $60\,K$. However, at both temperatures, the sharp drop at approximately $50\,meV$ binding energy remains. The only quantitative difference with respect to the undoped sample is the crossing point of the two trends, consistently lying at binding energies of approximately $0.17\,eV$, as compared to the pristine sample, where it is situated at approximately $0.1\,eV$.

As we have already established, the crossing point of the two trends might indicate the energetic position of the DP of the respective sample. The reason is the following: The temperature dependence stems from the plasmon decay channel depicted in Fig. 5.19, that is only open at low temperatures. At these, it increases the decay of electrons from the inner branch to the band bottom, effectively decreasing the hole lifetimes there. The hole lifetimes above the DP will be consequently prolonged.

The band bottom of the RSS on both samples shows a difference in binding energy of roughly $0.05\,eV$, with the RSS of the Mn-doped sample situated at higher binding energies (*cf.* Tab. 5.1). This is in line with the shift of the crossing point of the decay constants (Fig. 5.20b). This makes the surface plasmon indeed a likely candidate for a temperature-dependent decay channel. Scattering of the RSS electrons with optical phonons at $\mathbf{q} \approx 0$ can - at maximum - provide $19\,meV$ [186] per scattering event, and can therefore be excluded to be the major scattering channel between upper and lower branch.

Note, that the position of the CBM is not affected by Mn-doping. Therefore, the surface recombination rate should not be affected by the doping.

Fig. 5.21 shows decay constants obtained from the pristine and Mn-doped sample at comparable fluences for two different temperatures. We can see that both at $60\,K$ sample temperature (Fig. 5.21a) and at RT (Fig. 5.21b), the decay constants right above E_F are significantly larger for BiTeI:Mn. As we assume that the decay of the hot electrons is governed by electron-phonon scattering, this would mean a more effective coupling in the case of pristine BiTeI.

Alternatively, a possible explanation for the more pronounced divergence of decay times at the Fermi level on the doped sample is a larger accumulation of excess carriers that cannot recombine with holes. This is possible if the number of carriers excited above the Fermi level is larger in the case of the doped sample or the decay over the band gap is less effective. These carriers would accumulate at the Fermi level, significantly increasing the lifetimes there. From non-degenerate semiconductors, we know that relaxation over the band gap is significantly facilitated by defect states within the gap [175]. This would indicate that the Mn-doped sample has indeed the better crystal quality or at least surface quality on the microscopic level.

If we additionally observe a more effective trapping of the hot electrons at the surface in the case of the doped sample, *i.e.* a less effective diffusion into the bulk, or - due to the surface bend bending - a more effective diffusion of the holes, we would additionally
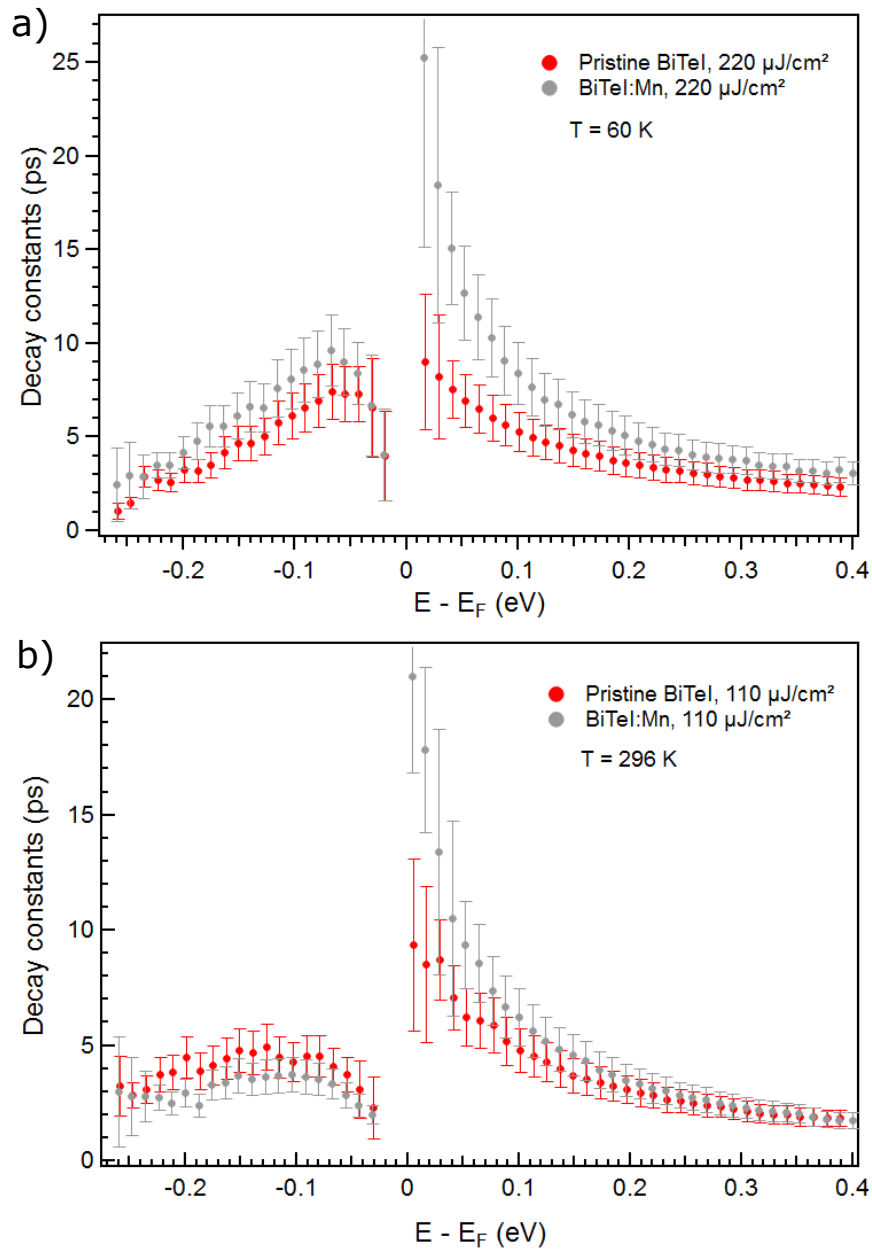
Figure 5.21: Decay constants τ_2 extracted from spectra measured on pristine BiTeI and BiTeI:Mn at RT (a) and 60 K sample temperature (b). The spectra were recorded at similar fluences to make them comparable. The error bars are estimated in the way explained in Fig. 5.9.

enhance the accumulation effect.

The difference in decay constants between the samples below E_F is less pronounced, especially when regarding the small differences in pump fluence. In the low temperature case, the lifetimes of BiTeI:Mn show an almost constant offset of roughly 1.5 picoseconds with respect to those of pristine BiTeI. However, the drop at 50 meV binding energy is sharper, leading to equal decay constants right below the Fermi level. On the RT sample, the hole decay constants are slightly increased on the pristine sample, but in general the closest to each other. In combination, those two features lead to the shift of the crossing point of the two trends, that we ascribe to the influence of the temperature dependent surface plasmon, as described above.

In summary, doping BiTeI with 3% manganese does not influence the dynamics qualitatively. The main differences are a small downward shift of the RSS and the resulting shift in the accessibility of the plasmon decay channel. Furthermore, it leads to increased decay times right above the Fermi level, possibly by a more effective trapping of electrons at the surface. Unfortunately, it remains ambiguous, whether these effects indicate a change of crystal quality.

5.3.2 BiTeI:V

Even though the vanadium-doped BiTeI sample can show a well resolvable RSS at 60 K (*cf.* Sec. 5.1.2), it was probably the sample with the lowest number of suitable spots, *i.e.* spots with resolvable surface states. Additionally, it showed the highest sensitivity towards the pump pulse, degrading at fluences higher than $75 \, \mu\text{J/cm}^2$.
As in the case of BiTeI:Mn, this hints at a comparably rough surface (*cf.* Sec. 5.3.1) or, alternatively, a lower stability of the crystal in general.

The second peculiarity of BiTeI:V are significantly altered dynamics, as compared to both pristine BiTeI and BiTeI:Mn. Fig. 5.22a) shows an exemplary delay spectrum, 350 meV above the Fermi level. If we compare these traces to the spectra shown in Fig. 5.8, we can already see, that the shapes of the curves deviate. This becomes much more evident when fitting the spectra, as the fits yield comparable decay constants τ_2, but significantly larger constants τ_1, as can be seen in Fig. 5.22b,c). The values of τ_1, as extracted by the fit, are heavily correlated not only with τ_2, but also with the corresponding amplitude A_1. The displayed values should therefore be understood as a general trend, not as a definitive quantitative result.

However, it is clear that with such large values, τ_1 can no longer be understood as an thermalization constant of a hot electron gas. Instead, we propose, that in the case of vanadium doping, scattering with the corresponding impurities can not only alter the momentum of the charge carriers (see also the discussion of Fig.5.7), but also heavily influence their energy. This might be possible, as long as the two subsystems are not equilibrated, if vanadium exhibits a significant partial DOS around the Fermi level, so that electrons can excite or deexcite the dopants during the scattering process. As
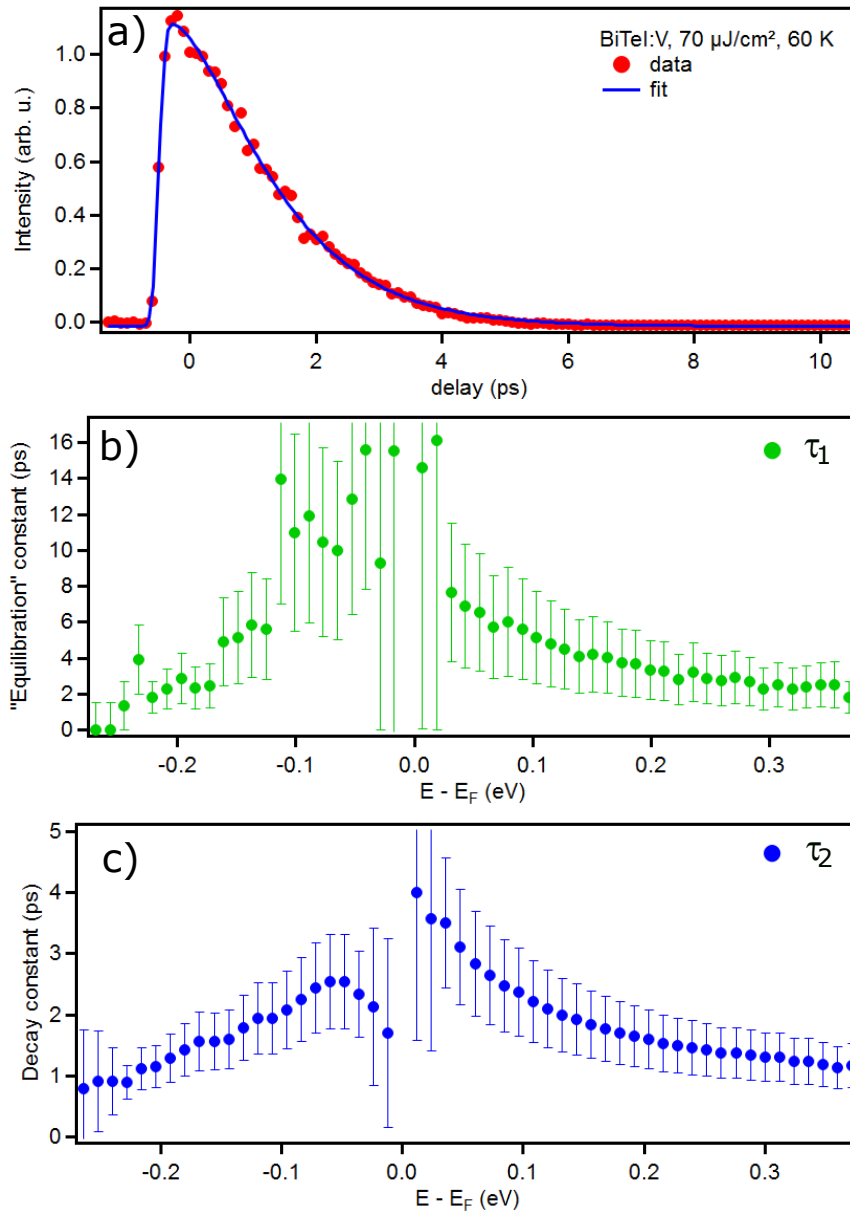
Figure 5.22: a) Exemplary delay spectrum recorded on BiTeI:V at $60\,\mathrm{K}$ sample temperature and a fluence of $70\,\mu\mathrm{J/cm^2}$ at $0.35\,\mathrm{eV}$ above E_F. b,c) Decay constants τ_1 and τ_2 extracted from the corresponding full spectrum, as explained in Fig 5.8. While the fits yield reliable results for τ_2, the values for τ_1 are heavily correlated with the corresponding amplitude A_1 and should therefore only considered as a qualitative result, not a quantitative one. The error bars are estimated in the way explained in Fig. 5.9. Here, they have to be estimated larger, with a base of 30% for τ_2 and an average 50% for τ_1.
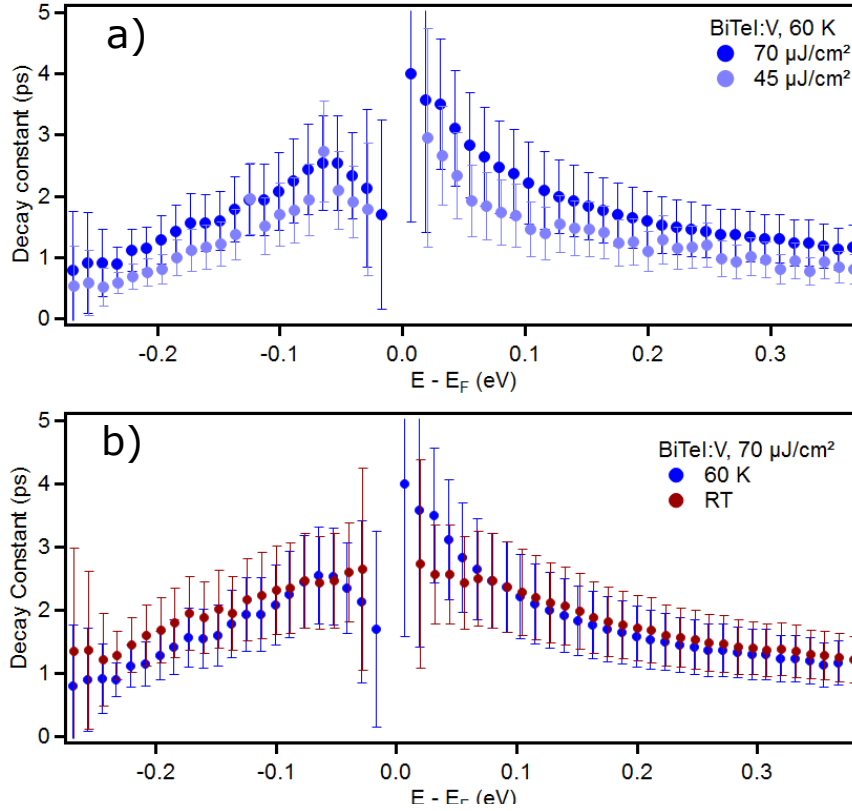
Figure 5.23: a) Fluence dependency of τ_2 on BiTeI:V at $60\,\text{K}$ sample temperature. b) Temperature dependency of τ_2 on BiTeI:V at a fluence of $70\,\mu\text{J/cm}^2$. The error bars are estimated in the way explained in Fig. 5.22.

vanadium seems to slightly influence the doping level of BiTeI, this is not unlikely. In order to confirm the presence of such a DOS, DFT calculations would be nescessary, which we are not able to do.

However, the defect density of states can not dissipate energy in total, only redistribute it. Therefore, τ_2 (*cf.* Fig. 5.22c) not only remains in the same order of magnitude as in the other two cases, in fact, even the general trends are very reminiscent of the formerly presented data, especially the undoped case: Above E_F, the electronic decay constants increase towards the Fermi level in a non-linear fashion, while the decay constants below show a linear increase towards E_F with a sharp drop right below it.

Also the fluence dependence of τ_2 shows the same trend as for the other two samples, as can be seen from Fig. 5.23a). This means, that we still see a general decrease of τ_2 with the fluence at all binding energies. This is a further indication, that the dopants influence the thermalization of the excited carriers, but not their relaxation.

However, the dynamics at RT on BiTeI:V is very similar to the dynamics at $60\,\text{K}$

(*cf.* Fig. 5.23b), in contrast to the other two samples. We therefore assume, that the plasmons on BiTeI:V are less temperature sensitive, possibly due to the roughness of the sample.

The missing kink in the decay constants below E_F at RT is more puzzling. In principle, it is possible, that the dopants decrease the effectivity of the dissipation of energy by drift currents. However, it is unclear, why this should only be the case at RT and not at 60 K.

In conclusion, vanadium dopants heavily influence the equilibration of the electrons in BiTeI. Furthermore, they seem to increase the sample roughness significantly, leading to a higher sensitivity to infrared radiation, but also stabilizing the surface plasmons.

5.4 Circular Dichroism on BiTeI

Mauchain *et al.* have reported the observation of CDAD patterns measured on BiTeI with circularly polarized pulses of 6.3 eV photon energy [111]. These patterns are three-fold symmetric and strongly resemble those we see for the lower topological surface state (TSS) in Ch. 4. However, for circularly polarized pump pulses with 1.5 eV, they see an excitation density reduced by approximately 15%, when comparing spectra recorded with right circularly polarized light (*rcp*) and left circularly polarized light (*lcp*), respectively. This they explain with helicity dependent super-diffusive transport, *i.e.* a spin-polarized excitation and subsequent spin-dependent transport. However, the excitation in the reported spectra is uniform, *i.e.* the branches of different spin are not discernible in their spectra.

In Fig. 5.24 we present our own results, recorded with circularly polarized pump and p-polarized probe pulses at the maximal temporal overlap, *i.e.* time zero. These are the same conditions utilized by Mauchain *et al.*, as far as we know, save for the sample temperature, which was 60 K during our measurements, in contrast to the reported 130 K. It is very evident, that we see no dichroism, *i.e.* no difference between spectra recorded with *rcp* and *lcp*.

As we have seen in Sec. 4.5, the CDAD patterns change already within the temporal overlap of the pulses if the underlying electron dynamics is fast enough. As Mauchain *et al.* report a dichroic signal as fast as 30 fs after time zero (recorded with a reported cross correlation of 80 fs), one would expect that signatures are already visible at time zero, especially as our cross correlation is longer (>120 fs). We therefore suspect that the dichroism observed by Mauchain *et al.* has a different origin than spin-dependent transport or that the spin-dependent transport is highly temperature sensitive and can be frozen out.

Another possible explanation might be a residual linear dichroism. As we have seen in the previous chapter on Bi_2Se_3 (*cf.* Ch. 4) and as explained in the section on the laser (*cf.* Sec. 3.2.1), achieving pure circular polarized light at the sample position is
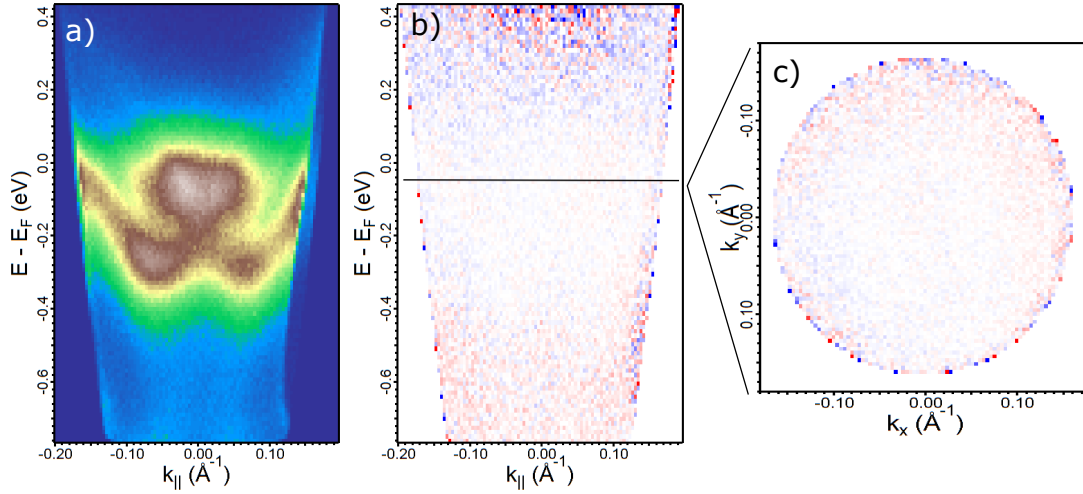
Figure 5.24: PE spectra recorded with *rcp* and *lcp* pump pulses of 1.5 eV photon energy and 6.2 eV p-polarized probe pulses at time zero on a BiTeI:Mn sample at 60 K. a) Sum of spectra recorded with *rcp* and *lcp* pump polarization respectively. b, c) Difference spectra, *i.e.* CDAD spectra for two different cuts through the 3D datasets.

typically not trivial and requires the precompensation of the influence of the incoupling mirrors and the window of the ultrahigh vacuum (UHV) chamber. If this is not done carefully enough, the light will have an elliptical polarization at the sample, with the linear component depending on the handedness of the initial circular polarization. Furthermore, many states show different absorption cross sections for *p*- and *s*-polarized light. Therefore, the dichroic signal observed by Mauchain *et al.*, that predominantly shows a difference in excitation density between *rcp* and *lcp* light, could stem from such elliptical components.

5.5 Conclusion

We investigated the electron and hole dynamics after photoexcitation in the polar semiconductor BiTeI. BiTeI possess Rashba-split surface and bulk bands due to its inversion-asymmetric crystal structure. Our static measurements confirm the existence of an electron-like RSS on the Te-terminated surface. The determined Rashba parameter is in line with previously reported values [34, 78]. We observe that the Fermi level lies within the split CBM, again in line with all previous reports. Additionally, we observe that the dispersions of the states are only resolvable after suppressing the photoemission signal from the I-terminated domains of the surface by aging the sample for a minimum of ten hours under pressures in the order of 2×10^{-9} mbar.

We find that manganese doping slightly increases the binding energy of the surface state. Vanadium doping seems to add slightly to the intrinsic n-doping of the material.
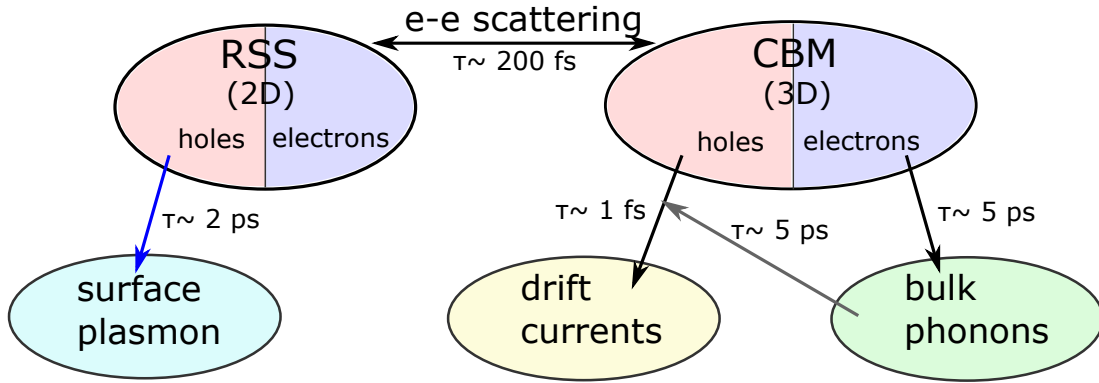
Figure 5.25: Schematic representation of the dominant decay channels in BiTeI. The electronic systems consists of four subsystems that equilibrate via electron-electron scattering: The respective photoelectrons and photoholes in the three-dimensional CBM and two-dimensional RSS. While bulk electrons and holes can couple to the bulk phonon bath, possibly dominantly to the optical phonons, the holes in the CBM are additionally heavily influenced by drift currents due to the surface band bending. The holes in the surface state relax *via* a plasmon channel, but only at low temperatures.

Furthermore, both dopants increasse the relative PE intensity obtained from the RSS with respect to the CBM and therefore lead to a better observability of the former. No further influence on the electronic structure was observed.

tr-ARPES measurements show, that the carrier dynamics after photoexcitation with $1.5\,\mathrm{eV}$ photon energy is very complex, due to the different involved subsystems, *i.e.* the two-dimensional RSS and the three-dimensional CBM. In principle, the contributions of the subsystems can only be indirectly determined *via* the study of the different dependencies of the energy resolved decay constants. We assume, that surface-to-bulk coupling by electron-electron scattering is very effective. The main decay channels have been summarized in Fig. 5.25.

Both above and below the Fermi level, we observe a fast thermalization of the photoexcited hot electron gas, on a timescale of $200\,\mathrm{fs}$. As we see no k-dependence of the dynamics neither above nor below the Fermi level, we assume that defect and phonon scattering redistribute momentum on even shorter timescales. The cooling of the hot electron gas, *i.e.* the recovery of the initial state, however, is different for the electron and hole subsystems.

The electron dynamics, *i.e.* the dynamics above E_{F}, is mainly governed by the bulk. Energy dissipation from the electronic system after excitation can be reasonably well described with electron-phonon scattering. Deviations of the observed intensities from a Fermi distribution are attributed to an increased number of carriers that are excited across the band gap from the VB as well as to the peculiar hole dynamics, see below. The maximum electronic temperature does not scale with the applied fluence as would be expected from a two-temperature model, indicating a very fast initial dissipation

of energy from the electronic system. This is expected from a compound with a polar crystal lattice, which should facilitate coupling between electrons and optical phonons with low q (Fröhlich interaction). After the initial fast dissipation, further dissipation of heat from the electronic system takes place on a timescale of roughly $4-6$ ps. This, in combination with the long thermalization time between electrons and the lattice - even after 11 ps the electron and phonon systems are not yet thermalized - is unexpected. We propose, that this feature hints at very long lifetimes of the initially excited optical phonons, *i.e.* very long equilibration times within the phonon subsystem, creating a phonon bottleneck for the dissipation of energy from the electronic system.

The hole dynamics, on the other hands, *i.e.* the dynamics below E_{F}, show a much larger influence of the surface properties. At 60 K sample temperature, the dynamics in the RSS are governed by the coupling of the electronic system to a surface plasmon, leading to a decrease of the decay times towards the band bottom and an increase towards the Fermi level. At RT, we observe that the decay is almost independent of binding energy and therefore probably dominated by surface recombination rather than electron-phonon coupling.
Note, that both processes, the coupling of the RSS to the surface plasmon and the surface recombination rate, become only relevant due to the long lifetimes created by the bottleneck in electron-phonon cooling.
Right below the Fermi level, both at 60 K and RT, we observe a sudden decrease of the decay times. Additionally, we observe much smaller depletion rates in the same energetic region than are to be expected from a Fermi distribution. The decrease of both the decay times and the depletion rates is due to ballistic transport of bulk carriers to the surface in the residual electrostatic field of the positively charged surface. The carriers from those currents accumulate around the Fermi level, where they can decay by surface recombination and electron-phonon scattering.

BiTeI:Mn shows dynamics that are very reminiscent of the pristine sample. The only notable differences are significantly higher decay times right above the Fermi level, indicating a larger percentage of carriers excited across the band gap and possibly even weaker electron-phonon coupling. Additionally, the change in binding energy of the RSS also influences the electron-plasmon coupling. The binding energy, where the dynamics at 60 K and RT coincide, which corresponds to the binding energy of the DP, is shifted to larger values.

Vanadium doping not only influences the n-doping of the sample, but also quenches the thermalization of the hot electron gas. We assume, that vanadium exhibits states right below and above the Fermi level. This would make electron-defect scattering not only effective at redistributing momentum, but also energy within the hot electron gas. DFT calculations are necessary to confirm or refute this assumption.

Finally, we could not reproduce previously reported CDAD patterns upon the excitation of the sample with circular polarized light [111]. We assume that residual linear components lead to a linear dichroism in the previously reported measurements.

Chapter 6

Summary and Conclusion

In recent years, a lot of novel approaches to the improvement of performance and efficiency of computers have emerged. One of these approaches are so-called spintronics, where the spin-degree of freedom of electrons is sought to be exploited. Within this field, the excitation of spin-polarized currents is a major challenge. One suggested solution is the excitation of spin-polarized (surface) states of strongly spin-orbit coupled materials, *e.g.* by circular polarized light. Generally, it is assumed that a coupling of the photon angular momentum to a parallel spin will lead to a preferrential excitation in a spin-polarized state.

In this work, the response of the electronic system during and after excitation with near-infrared (nIR) light in two semiconductors which are treated as promising candidates is investigated. On the one hand, we investigate the origin of helicity-dependent photocurrents on the topological insulator (TI) Bi_2Se_3 by means of two-photon photoemission (2PPE). On the other, we study the electron and hole relaxation dynamics in the Rashba-split surface and bulk bands of BiTeI by means of time- and angle-resolved photoemission spectroscopy (tr-ARPES).

The advantage of studying the response of the electronic system with these techniques over transport studies is the possibility to disentangle contributions from specific involved states, and establish dependencies both on the crystal momentum k and the binding energy E. Furthermore, the employed angle-resolving time-of-flight (ToF) spectrometer allows for the simultaneous recording of the two in-plane components of the photoelectron's momentum as well as the kinetic energy.

Chapter 4 discusses the circular dirchoism in the angular distribution (CDAD) patterns observed during the excitation of Bi_2Se_3 with circular polarized light of 1.7 and 1.9 eV photon energy. Hereby, the excitation with 1.7 eV corresponds to a resonant excitation between the occupied and unoccupied topological surface state (TSS), which are both situated at the $\overline{\Gamma}$ point of the surface Brillouin zone (BZ). The distribution of the photoexcited electrons in the unoccupied TSS was probed with s-polarized pulses of 4.7 eV photon energy, ensuring that the probing step has a minimal influence on the observed patterns.

We confirm that the formation of CDAD patterns predominantly depends on the coupling of the incident photons to the initial state. In other words, the intermediate state plays no significant role, as confirmed by off-resonant measurements, time-resolved data and model calculations performed by our collaboration partners.

However, the observed CDAD in the TSSs does not show the expected anti-symmetric

patterns that would correspond to the excitation mechanism typically proposed for the photocurrents observed in transport measurements. Instead, we observe threefold-symmetric patterns reminiscent of the bulk crystal symmetry. The only exception to this is the pattern at the conduction band minimum (CBM), which actually shows an anti-symmetric electron distribution. However, this pattern could not be reproduced by theory and its emergence remains unexplained. This asymmetry plus residual asymmetries in the TSSs, possibly stemming from experimental inaccuracies, are large enough to explain the origin of the photocurrents instead. These currrents are not *a priori* spin-polarized.

In Chapter 5, the electron and hole dynamics in the Rashba-split surface state (RSS) and CBM on the Te-terminated surface of BiTeI are presented and analyzed. BiTeI is an intrinsically n-doped degenerate semiconductor with a direct band gap. The crystal lattice lacks inversion symmetry, leading to Rashba-split bulk states. Furthermore, the polar surfaces of BiTeI host RSSs. In static measurements, we confirmed previously reported values for the Rashba-splitting of the electron-like RSS on the Te-terminated surface. Furthermore, we find that both manganese and vanadium doping of 3% and 2.5% respectively does not strongly influence the electronic structure, but improve the observability of the RSS in our spectra.

The electron dynamics on BiTeI was investigated by a pump-probe scheme, during which the electronic system was excited by laser pulses of 1.5 eV photon energy and probed with pulses of 6.2 eV, giving access to the population dynamics across the Fermi level. By investigating the dependence of the dynamics on the crystal momentum $\mathbf{k}_{||}$, binding energy E, sample base temperature T and incident fluence F, we can disentangle different decay channels open to the surface 2D electron gas and bulk 3D electron gas. We find, that across all subsystems, electron-electron scattering effectively leads to a thermalization of the hot electron gas on a timescale of $\tau_1 \approx 200$ fs. The only exception here is the V-doped sample, where we observe no such equilibration. This hints at additional states around the Fermi level stemming from the dopants, that effectively redistribute energy during collisions. Furthermore, we find no dependence of the dynamics on the crystal momentum $\mathbf{k}_{||}$ on any of the samples, indicating very effective momentum redistribution by quasielastic defect and phonon scattering.

The dynamics above the Fermi level are dominated by the bulk bands. The scaling law of the maximum electronic temperature with the incident fluence hints at a very fast dissipation of heat from the electronic system, most probably *via* the excitation of optical phonons with low momentum $\mathbf{q}$ by Fröhlich interaction. The dissipation time in the picosecond range at higher delays and even longer thermalization time with the lattice hints at a long lifetime of these optical phonons, effectively reducing the cooling of the hot 3D electron gas by electron-phonon coupling (phonon bottleneck).

Electrons excited over the band gap accumulate above the Fermi level before they can recombine with holes across the band gap, increasing the lifetimes at the Fermi level further. This process is most prominent on the Mn-doped sample. Diffusion of the hot carriers into the bulk seems to be hindered by the positive partial charge of the surface and the resulting band bending.

On the contrary, this band bending results in a drift current of electrons towards the surface. This decreases both the depletion rates and the recovery times at binding energies up to 50 meV, *i.e.* right below the Fermi level. This energy coincides with the suspected position of the CBM in the bulk. At higher binding energies, the dynamics is dominated by the RSS. At sample temperatures of 60 K we see the influence of a plasmon decay channel that closes at room temperature (RT). This is probably due to an increased scattering of electrons with optical phonons, significantly broadening and reducing the intensity of the plasmon. The only exception, is the V-doped sample, where the plasmon persists up to RT.

Finally, we tried to reproduce previously reported signatures of CDAD upon excitation with circular polarized pump pulses. These were interpreted to be caused by ballistic spin-dependent transport. We could not reproduce the findings and therefore dispute the claim. Instead, we propose that residual linear dichroism is responsible for the previously reported patterns.

From an applied point of view, we have to conclude that the excitation of spin-polarized currents on the two investigated materials by circular polarized light is not as straight-forward as one would hope. Instead, complex interaction mechanisms of the electronic system with the crystal lattice and surface properties govern the excitation and relaxation processes, which is fascinating from a fundamental scientific point of view.

Appendix A

BiTeI: Dynamics at room temperature

In Secs. 5.2 and 5.3.1, we have presented the fluence dependence of the electron and hole dynamics at 60 K sample temperature of pristine BiTeI and BiTeI:Mn respectively (cf. Figs. 5.11a), 5.16a) and 5.20a). Furthermore, we have shown the temperature dependence of the dynamics for one selected fluence each (cf. Figs. 5.12, 5.18, and 5.20b).

Here, we provide additional traces of the decay constant τ_2, obtained from spectra measured at room temperature with different fluences on both samples (c.f. Fig 5.8 for the process of obtaining τ_2). These traces show, that altering the fluence at room temperature will influence the spectra quantitatively, but not qualitatively (c.f. Fig. A.1): With increasing fluence, τ_2 will increase both above and below the Fermi level, both for pristine and Mn-dpoed BiTeI. Meanwhile, the functional dependency of τ_2 on the binding energy - diverging above E_F and linear with a kink below E_F - will not change. The only notable difference is the trace recorded on BiTeI:Mn with a fluence of $110 \, \mu J/cm^2$. Here, the decay times of the holes are lower than to be expected from the general trends. We have not found an explanation for this deviation, especially regarding the fact, that the electronic decay times, recorded at the same time, match the general trend.
The influence of the dopants, i.e. the differences between Fig. A.1a) and Fig. A.1b), is the same at room temperature and at 60 K, c.f. Sec. 5.3.1, especially Fig. 5.21.
Disregarding the outlier, we can conclude, that the decay constant traces at room temperature presented in the main part of this thesis are representative for all fluences.

In summary, the fluence dependence at room temperature mirrors that at 60 K for both samples. As a consequence, the reverse is also true: The temperature dependence discussed in Secs. 5.2 and 5.3.1 is indeed the same for all fluences.
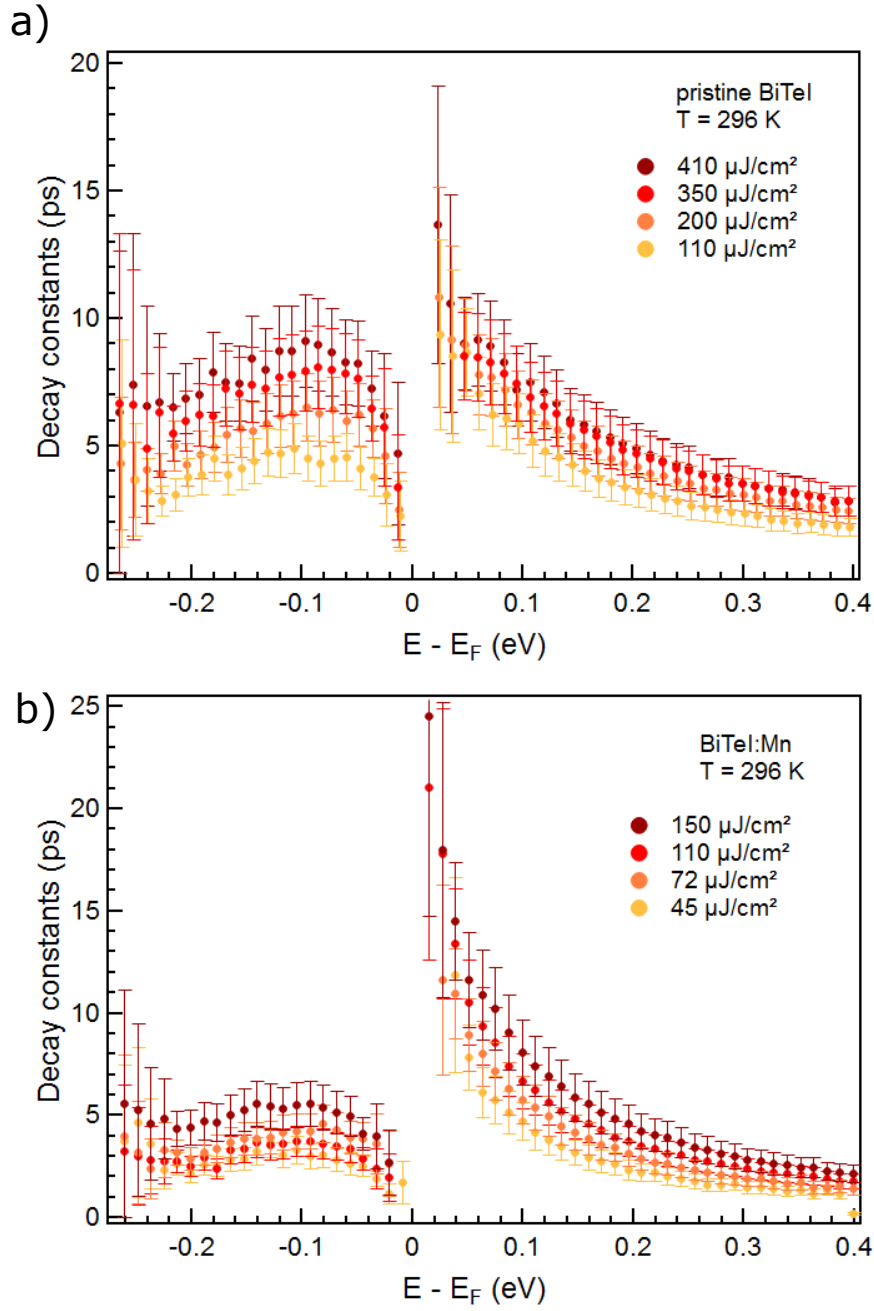
Figure A.1: Decay constants τ_2 of the excited carriers above and below the Fermi level in pristine BiTeI (a) and BiTeI:Mn (b). The decay constants were obtained as explained in Fig 5.8 from datasets measured with different pump fluences on the respective samples. The samples were kept at room temperature throughout all measurements. The errors are estimated from the robustness of the fits, as explained in Fig. 5.9.

Appendix B

Evolution of the Electronic Temperature on BiTeI:Mn

In Sec. 5.2.1, we have discussed the influence of electron-phonon coupling on the electron dynamics in pristine BiTeI. An important indicator for the importance of electron-phonon coupling was the temporal evolution of the electronic temperature after excitation. We have seen that on pristine BiTeI, the electronic temperature can be estimated from fitting the temporal evolution of the integrated photoelectron (PE) signal, although the deviating hole dynamics as well as the cross-correlation between electronic temperature and energy resolution make it hard to make quantitative statements.

Here, we show the corresponding results for BiTeI:Mn, cf. Fig. B.1. We can see, that we can achieve a better agreement of the fits with the measured density of states (DOS) around the Fermi level, even at delays as small as 1 ps. This is possibly due to the much smaller fluence applied during the measurements, which was a factor three smaller than in the spectra shown in Fig. 5.14.
This corroborates the finding of Sec. 5.2.1, that the electronic temperatures are well defined for low pump fluences, but produce worse models for higher pump fluences. Nevertheless, the maximum electronic temperature reached as well as the residual temperature increase after 11 ps is higher than the pristine sample would have reached with this pump fluence. However, as we have already argued, all quantitative comparisons have to be taken with a grain of salt, as the fits show significant deviations from the data, especially for the pristine sample and at high pump fluences.

The initial temperatures are not overestimated for BiTeI:Mn, in contrast to the case of pristine BiTeI (cf. Fig. 5.15), while the resolution was fixed to an even lower value, i.e. a better resolution than for the fitting of the datasets obtained on pristine samples.

The dynamics on BiTeI:Mn generally confirms the phonon bottleneck, as the electronic temperatures after 11 ps are still elevated with respect to the expected lattice temperature.
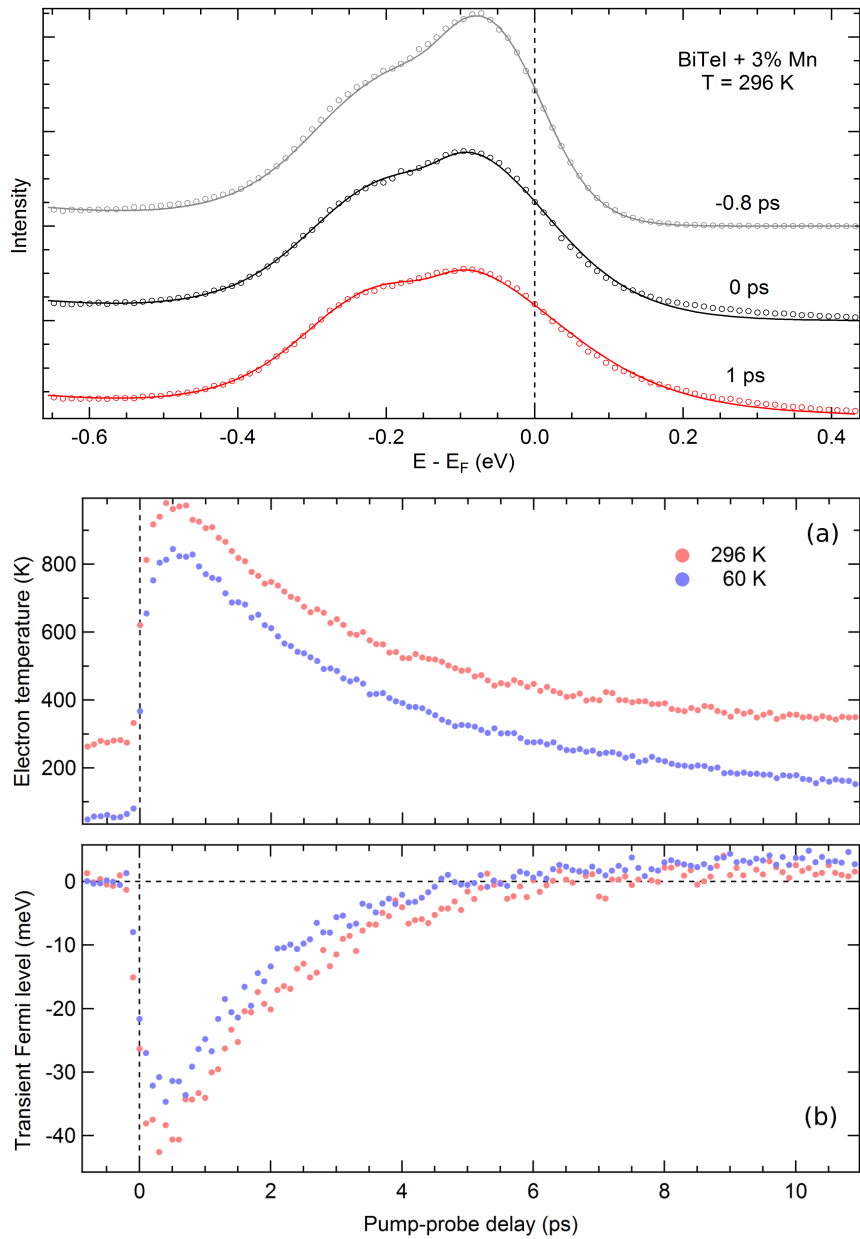
Figure B.1: a) The PE intensity recorded on BiTeI:Mn plotted over the kinetic energy at three characteristic delays (dots). The sample was kept at room temperature and the applied pump fluence was $70 \, \mu\mathrm{J/cm^2}$. The data was fitted as explained in Fig 5.5 (solid lines). We see a good agreement of the fits with the data before the excitation and from one picosecond after the excitation on. b) Electronic temperatures over pump-probe delay, extracted from the Fermi distribution in the fits of the DOS, as exemplarily shown in (a). c) Chemical potential, extracted from the data in the same way.

Appendix C

Supplementary Figures to Chapter 5
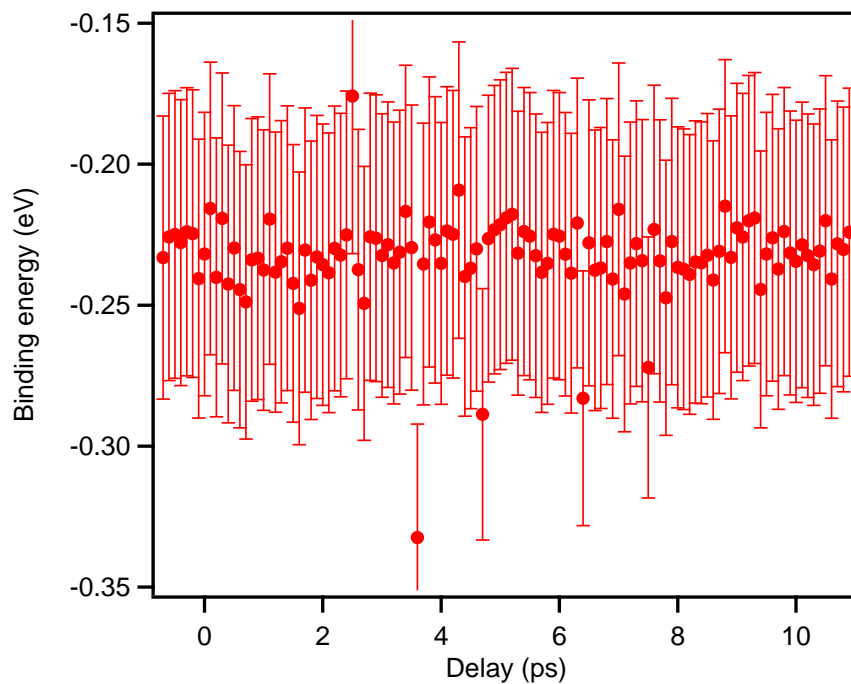
Figure C.1: Position of the band bottom of the RSS, exemplarily shown for BiTeI:Mn, plotted over pump-probe delay. The values were obtained by fitting a cut at $k_x = 0.05\,\text{Å}^{-1}$ through a delay scan obtained with a fluence of $220\,\mu\text{J/cm}^2$ at $60\,\text{K}$ sample temperature. It shows that the band does not move and therefore that there is no surface photovoltage generated during the pump-probe measurements, even at high fluences.
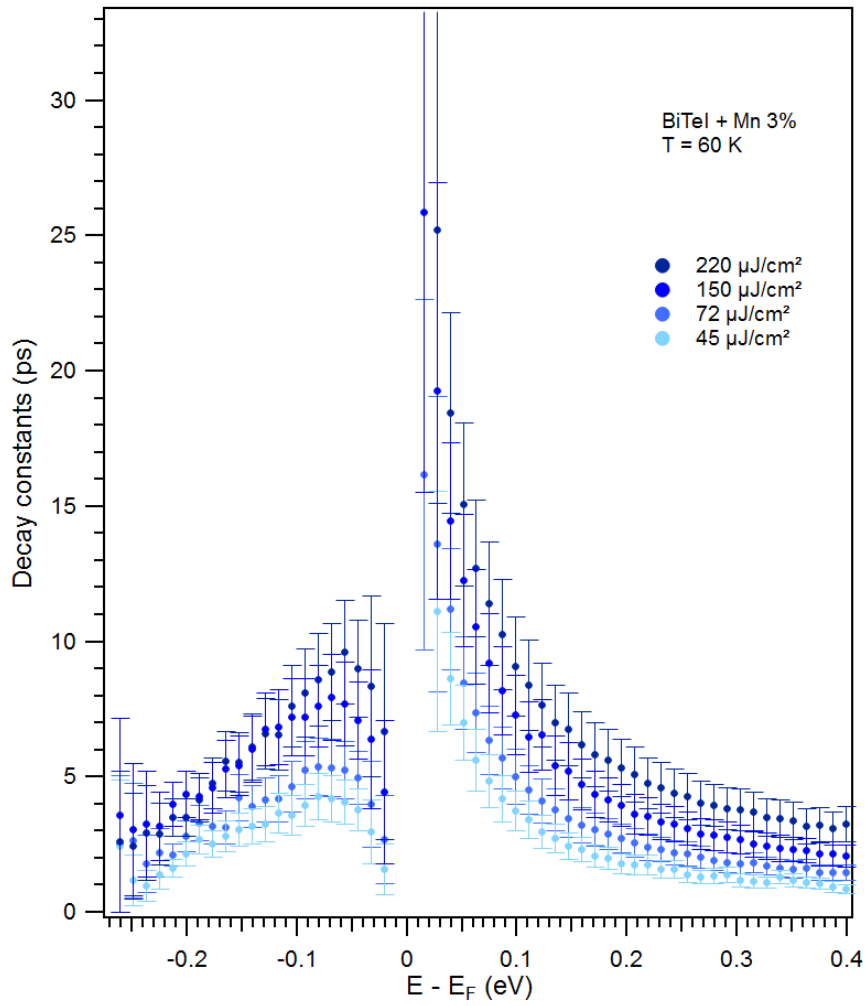
Figure C.2: Decay constants τ_2 of the carriers in BiTeI:Mn. The data is the same as displayed in Fig. 5.20a) but with error bars. The error bars are estimated in the way explained in Fig. 5.9.
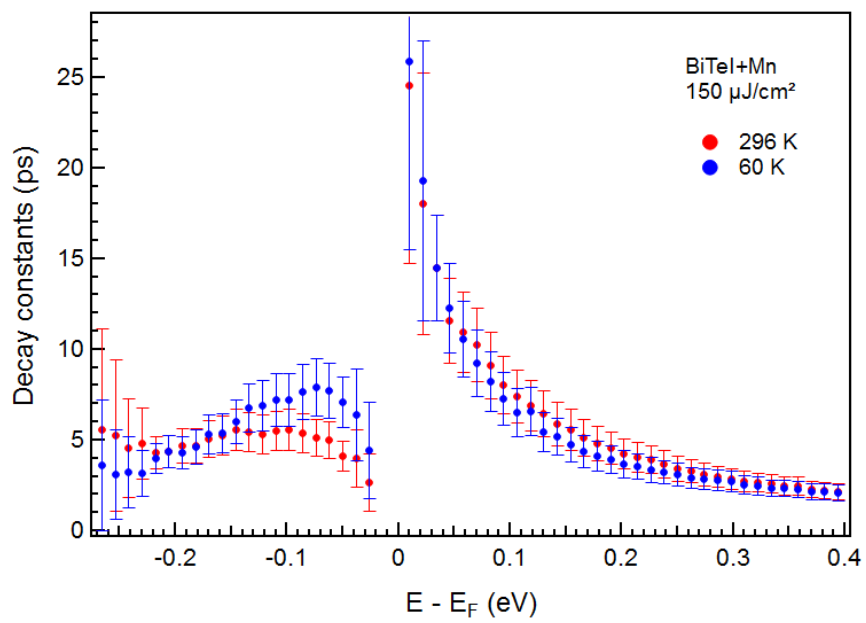
Figure C.3: Decay constants τ_2 of the carriers in BiTeI:Mn. The data is the same as displayed in Fig. 5.20b) but with error bars. The error bars are estimated in the way explained in Fig. 5.9.

Bibliography

[1]   M. Aeschlimann, C. A. Schmuttenmaer, H. E. Elsayed-Ali, R. J. D. Miller, J. Cao, Y. Gao, and D. A. Mantell. "Observation of surface enhanced multiphoton photoemission from metal surfaces in the short pulse limit". In: *J. Chem. Phys.* 102.21 (1995), pp. 8606–8613. DOI: 10.1063/1.468962 (cit. on p. 100).

[2]   I. Aguilera, C. Friedrich, G. Bihlmayer, and S. Blügel. "GW study of topological insulators Bi_2Se_3, Bi_2Te_3, and Sb_2Te_3: Beyond the perturbative one-shot approach". In: *Phys. Rev. B* 88.4 (2013), p. 045206. DOI: 10.1103/physrevb.88.045206 (cit. on p. 47).

[3]   I. Aguilera, C. Friedrich, and S. Blügel. "Spin-orbit coupling in quasiparticle studies of topological insulators". In: *Phys. Rev. B* 88.16 (2013), p. 165136. DOI: 10.1103/physrevb.88.165136 (cit. on p. 47).

[4]   S. Anisimov, B. Kapelovich, and T. Perelman. "Electron emission from metal surfaces exposed to ultrashort laser pulses". In: *Zh. Eksp. Teor. Fiz.* 66.2 (1974), pp. 776–781 (cit. on pp. 87, 88).

[5]   D. E. Aspnes, S. M. Kelso, R. A. Logan, and R. Bhat. "Optical properties of $Al_xGa_{1-x}As$". In: *J. Appl. Phys.* 60.2 (1986), pp. 754–767. DOI: 10.1063/1.337426 (cit. on p. 96).

[6]   D. E. Aspnes and A. A. Studna. "Dielectric functions and optical parameters of Si, Ge, GaP, GaAs, GaSb, InP, InAs, and InSb from 1.5 to 6.0 eV". In: *Phys. Rev. B* 27.2 (1983), pp. 985–1009. DOI: 10.1103/physrevb.27.985 (cit. on p. 96).

[7]   C. R. Ast, J. Henk, A. Ernst, L. Moreschini, M. C. Falub, D. Pacilé, P. Bruno, K. Kern, and M. Grioni. "Giant Spin Splitting through Surface Alloying". In: *Phys. Rev. Lett.* 98.18 (2007), p. 186807. DOI: 10.1103/physrevlett.98.186807 (cit. on p. 67).

[8]   M. Bahramy, P. King, A. de la Torre, J. Chang, M. Shi, L. Patthey, G. Balakrishnan, P. Hofmann, R. Arita, N. Nagaosa, and F. Baumberger. "Emergent quantum confinement at topological insulator surfaces". In: *Nat. Commun.* 3.1 (2012), p. 1159. DOI: 10.1038/ncomms2162 (cit. on p. 50).

[9]   M. N. Baibich, J. M. Broto, A. Fert, F. N. V. Dau, F. Petroff, P. Etienne, G. Creuzet, A. Friederich, and J. Chazelas. "Giant Magnetoresistance of (001)Fe/(001)Cr Magnetic Superlattices". In: *Phys. Rev. Lett.* 61.21 (1988), pp. 2472–2475. DOI: 10.1103/physrevlett.61.2472 (cit. on p. 1).

[10] M. Bastian. "Simulation of Electron Trajectories in a ToF Photoelectron Spectrometer and Application to Topological Surface States". MA thesis. FU Berlin, 2016 (cit. on pp. 30, 35, 39).

[11] H. M. Benia, C. Lin, K. Kern, and C. R. Ast. "Reactive Chemical Doping of the Bi$_2$Se$_3$ Topological Insulator". In: *Phys. Rev. Lett.* 107.17 (2011), p. 177602. DOI: 10.1103/PhysRevLett.107.177602 (cit. on pp. 39, 50).

[12] V. B. Berestetskii, E. M. Lifshitz, and L. P. Pitaevskii. *Relativistic Quantum Theory.* Ed. by J. B. Sykes and J. S. Bell. Pergamon Press, 1971 (cit. on pp. 9, 10).

[13] B. A. Bernevig and T. L. Hughes. *Topological Insulators and Topological Superconductcors.* Princeton University Press, 2013 (cit. on pp. 2, 14, 15).

[14] B. A. Bernevig, T. L. Hughes, and S.-C. Zhang. "Quantum Spin Hall Effect and Topological Phase Transition in HgTe Quantum Wells". In: *Science* 314.5806 (2006), pp. 1757–1761. DOI: 10.1126/science.1133734 (cit. on pp. 16, 18).

[15] B. A. Bernevig and S.-C. Zhang. "Quantum Spin Hall Effect". In: *Phys. Rev. Lett.* 96.10 (2006), p. 106802. DOI: 10.1103/physrevlett.96.106802 (cit. on p. 16).

[16] M. V. Berry. "Quantal Phase Factors Accompanying Adiabatic Changes". In: *Proc. Roy. Soc. A* 392.1802 (1984), pp. 45–57. DOI: 10.1098/rspa.1984.0023 (cit. on p. 16).

[17] M. Bianchi, R. C. Hatch, J. Mi, B. B. Iversen, and P. Hofmann. "Simultaneous Quantization of Bulk Conduction and Valence States through Adsorption of Nonmagnetic Impurities on Bi$_2$Se$_3$". In: *Phys. Rev. Lett.* 107.8 (2011), p. 086802. DOI: 10.1103/PhysRevLett.107.086802 (cit. on p. 39).

[18] G. Bihlmayer, Y. Koroteev, P. Echenique, E. Chulkov, and S. Blügel. "The Rashba-effect at metallic surfaces". In: *Surf. Sci.* 600.18 (2006), pp. 3888–3891. DOI: 10.1016/j.susc.2006.01.098 (cit. on p. 14).

[19] G. Bihlmayer, O. Rader, and R. Winkler. "Focus on the Rashba effect". In: *New J. Phys.* 17.5 (2015), p. 050202. DOI: 10.1088/1367-2630/17/5/050202 (cit. on pp. 2, 12).

[20] G. Binasch, P. Grünberg, F. Saurenbach, and W. Zinn. "Enhanced magnetoresistance in layered magnetic structures with antiferromagnetic interlayer exchange". In: *Phys. Rev. B* 39.7 (1989), pp. 4828–4830. DOI: 10.1103/physrevb.39.4828 (cit. on p. 1).

[21] F. Bloch. "Über die Quantenmechanik der Elektronen in Kristallgittern". In: *Z. Phys.* 52.7 (1929), p. 555. DOI: 10.1007/BF01339455 (cit. on pp. 10, 15).

[22] N. Borgwardt, J. Lux, I. Vergara, Z. Wang, A. A. Taskin, K. Segawa, P. H. M. van Loosdrecht, Y. Ando, A. Rosch, and M. Grüninger. "Self-organized charge puddles in a three-dimensional topological material". In: *Phys. Rev. B* 93.24 (2016), p. 245149. DOI: 10.1103/physrevb.93.245149 (cit. on p. 49).

[23] U. Bovensiepen. "Coherent and incoherent excitations of the Gd(0001) surface on ultrafast timescales". In: *J. Phys-Condens. Mat.* 19.8 (2007), p. 083201. DOI: 10.1088/0953-8984/19/8/083201 (cit. on pp. 87, 88).

[24] J. Braun. *private communication* (cit. on pp. 41, 42).

[25] L. Braun, G. Mussler, A. Hruban, M. Konczykowski, M. Wolf, T. Schumann, M. Münzenberg, L. Perfetti, and T. Kampfrath. "Ultrafast photocurrents at the surface of the three-dimensional topological insulator Bi_2Te_2Se". In: *Nat. Commun.* 7 (2016), p. 13259. DOI: 10.1038/ncomms13259 (cit. on pp. 3, 43, 49).

[26] N. P. Butch, K. Kirshenbaum, P. Syers, A. B. Sushkov, G. S. Jenkins, H. D. Drew, and J. Paglione. "Strong surface scattering in ultrahigh-mobility Bi_2Se_3 topological insulator crystals". In: *Phys. Rev. B* 81.24 (2010), p. 241301. DOI: 10.1103/PhysRevB.81.241301 (cit. on p. 45).

[27] C. J. Butler, H.-H. Yang, J.-Y. Hong, S.-H. Hsu, R. Sankar, C.-I. Lu, H.-Y. Lu, K.-H. O. Yang, H.-W. Shiu, C.-H. Chen, C.-C. Kaun, G.-J. Shu, F.-C. Chou, and M.-T. Lin. "Mapping polarization induced surface band bending on the Rashba semiconductor BiTeI". In: *Nat. Commun.* 5.1 (2014), p. 4066. DOI: 10.1038/ncomms5066 (cit. on pp. 68, 70).

[28] Y. Bychkov and E. Rashba. "Properties of a 2D electron gas with lifted spectral degeneracy". In: *JETP Lett.* 39 (1984), pp. 78–81 (cit. on pp. 1, 2, 13, 68).

[29] Y. A. Bychkov and E. I. Rashba. "Oscillatory effects and the magnetic susceptibility of carriers in inversion layers". In: *J. Phys. C Solid State* 17.33 (1984), pp. 6039–6045. DOI: 10.1088/0022-3719/17/33/015 (cit. on pp. 2, 13, 68).

[30] C. Cacho, A. Crepaldi, M. Battiato, J. Braun, F. Cilento, M. Zacchigna, M. C. Richter, O. Heckmann, E. Springate, Y. Liu, S. S. Dhesi, H. Berger, P. Bugnon, K. Held, M. Grioni, H. Ebert, K. Hricovini, J. Minár, and F. Parmigiani. "Momentum-Resolved Spin Dynamics of Bulk and Surface Excited States in the Topological Insulator Bi_2Se_3". In: *Phys. Rev. Lett.* 114.9 (2015), p. 097401. DOI: 10.1103/PhysRevLett.114.097401 (cit. on pp. 19, 50).

[31] Y. L. Chen, J. G. Analytis, J.-H. Chu, Z. K. Liu, S.-K. Mo, X. L. Qi, H. J. Zhang, D. H. Lu, X. Dai, Z. Fang, S. C. Zhang, I. R. Fisher, Z. Hussain, and Z.-X. Shen. "Experimental Realization of a Three-Dimensional Topological Insulator, Bi_2Te_3". In: *Science* 325 (2009), p. 178. DOI: 10.1126/science.1173034 (cit. on pp. 19, 45).

[32] R. Courtland. *Gordon Moore: The Man Whose Name Means Progress.* Interview in IEEE Spectrum. https://spectrum.ieee.org/computing/hardware/gordon-moore-the-man-whose-name-means-progress. 2015 (cit. on p. 1).

[33] A. Crepaldi, F. Cilento, B. Ressel, C. Cacho, J. C. Johannsen, M. Zacchigna, H. Berger, P. Bugnon, C. Grazioli, I. C. E. Turcu, E. Springate, K. Kern, M. Grioni, and F. Parmigiani. "Evidence of reduced surface electron-phonon scattering in the conduction band of Bi_2Se_3 by nonequilibrium ARPES". In: *Phys. Rev. B* 88.12 (2013), p. 121404. DOI: 10.1103/PhysRevB.88.121404 (cit. on p. 19).

[34]   A. Crepaldi, L. Moreschini, G. Autès, C. Tournier-Colletta, S. Moser, N. Virk,
        H. Berger, P. Bugnon, Y. J. Chang, K. Kern, A. Bostwick, E. Rotenberg, O. V.
        Yazyev, and M. Grioni. "Giant Ambipolar Rashba Effect in the Semiconductor
        BiTeI". In: *Phys. Rev. Lett.* 109.9 (2012), p. 096803. DOI: 10.1103/physrevlett.
        109.096803 (cit. on pp. 4, 68, 70–73, 77, 96, 108).

[35]   G. Czycholl. *Theoretische Festkörperphysik*. Dritte Auflage. Springer Berlin Hei-
        delberg, 2008 (cit. on pp. 92, 93).

[36]   S. Datta and B. Das. "Electronic analog of the electro-optic modulator". In: *Appl.
        Phys. Lett.* 56.7 (1990), pp. 665–667. DOI: 10.1063/1.102730 (cit. on pp. 1, 2,
        7, 67).

[37]   N. T. Dich, P. Lošťák, and J. Horák. "Preparation and basic physical properties
        of BiTeI single crystals". In: *Czech. J. Phys.* 28.11 (1978), pp. 1297–1303. DOI:
        10.1007/bf01599969 (cit. on pp. 68, 93, 97).

[38]   G. Dresselhaus. "Spin-Orbit Coupling Effects in Zinc Blende Structures". In:
        Phys. Rev. 100.2 (1955), pp. 580–586. DOI: 10.1103/physrev.100.580 (cit. on
        pp. 1, 12).

[39]   M. Dresselhaus, G. Dresselhaus, and A. Jorio. *Group Theory - Application to the
        Physics of Condensed Matter*. Springer, 2008 (cit. on p. 12).

[40]   H.-J. Drouhin. "Spin-dependent scattering in transition metals". In: *J. Appl.
        Phys.* 89.11 (2001), pp. 6805–6807. DOI: 10.1063/1.1358330 (cit. on p. 22).

[41]   Ebert, H. *et al. The Munich SPR-KKR package*, version 7.7, 2017,
        http://olymp.cup.uni-muenchen.de/ak/ebert/SPRKKR (cit. on p. 41).

[42]   H. Ebert, D. Ködderitzsch, and J. Minár. "Calculating condensed matter prop-
        erties using the KKR-Green's function method—recent developments and ap-
        plications". In: *Rep. Prog. Phys.* 74.9 (2011), p. 096501. DOI: 10.1088/0034-
        4885/74/9/096501 (cit. on p. 41).

[43]   P. Echenique, R. Berndt, E. Chulkov, T. Fauster, A. Goldmann, and U. Höfer.
        "Decay of electronic excitations at metal surfaces". In: *Surf. Sci. Rep.* 52.7-8
        (2004), pp. 219–317. DOI: http://dx.doi.org/10.1016/j.surfrep.2004.02.
        002 (cit. on p. 47).

[44]   A. Einstein. "Über einen die Erzeugung und Verwandlung des Lichtes betref-
        fenden heuristischen Gesichtspunkt". In: *Ann. Phys.* 322.6 (1905), pp. 132–148.
        DOI: 10.1002/andp.19053220607 (cit. on p. 21).

[45]   R. J. Elliott. "Spin-Orbit Coupling in Band Theory—Character Tables for Some
        "Double" Space Groups". In: *Phys. Rev.* 96.2 (1954), pp. 280–287. DOI: 10.1103/
        physrev.96.280 (cit. on p. 1).

[46]   G. Engels, J. Lange, T. Schäpers, and H. Lüth. "Experimental and theoretical
        approach to spin splitting in modulation-doped $In_xGa_{1-x}As/InP$ quantum wells
        for B→0". In: *Phys. Rev. B* 55.4 (1997), R1958–R1961. DOI: 10.1103/physrevb.
        55.r1958 (cit. on p. 14).

[47] S. V. Eremeev, I. A. Nechaev, and E. V. Chulkov. "Giant Rashba-type spin splitting at polar surfaces of BiTeI". In: *JETP Lett.* 96.7 (2012), pp. 437–444. DOI: 10.1134/S0021364012190071 (cit. on pp. 68–70, 73, 97, 98).

[48] S. V. Eremeev, I. A. Nechaev, Y. M. Koroteev, P. M. Echenique, and E. V. Chulkov. "Ideal Two-Dimensional Electron Systems with a Giant Rashba-Type Spin Splitting in Real Materials: Surfaces of Bismuth Tellurohalides". In: *Phys. Rev. Lett.* 108.24 (2012), p. 246802. DOI: 10.1103/physrevlett.108.246802 (cit. on pp. 2, 68).

[49] S. Fiedler, T. Bathon, S. V. Eremeev, O. E. Tereshchenko, K. A. Kokh, E. V. Chulkov, P. Sessi, H. Bentmann, M. Bode, and F. Reinert. "Termination-dependent surface properties in the giant-Rashba semiconductors BiTeX (X=Cl, Br, I)". In: *Phys. Rev. B* 92.23 (2015), p. 235430. DOI: 10.1103/physrevb.92.235430 (cit. on pp. 68, 70).

[50] S. Fiedler, L. El-Kareh, S. V. Eremeev, O. E. Tereshchenko, C. Seibel, P. Lutz, K. A. Kokh, E. V. Chulkov, T. V. Kuznetsova, V. I. Grebennikov, H. Bentmann, M. Bode, and F. Reinert. "Defect and structural imperfection effects on the electronic properties of BiTeI surfaces". In: *New J. Phys.* 16.7 (2014), p. 075013. DOI: 10.1088/1367-2630/16/7/075013 (cit. on pp. 4, 70–72, 96).

[51] J. K. Freericks, H. R. Krishnamurthy, M. A. Sentef, and T. P. Devereaux. "Gauge invariance in the theoretical description of time-resolved angle-resolved pump/probe photoemission spectroscopy". In: *Phys. Scripta* T165 (2015), p. 014012 (cit. on p. 53).

[52] B. Frietsch, R. Carley, M. Gleich, M. Teichmann, J. Bowlan, and M. Weinelt. "Fluence-dependent dynamics of the 5d6s exchange splitting in Gd metal after femtosecond laser excitation". In: *Jpn. J. Appl. Phys.* 55.7S3 (2016), p. 07MD02. DOI: 10.7567/jjap.55.07md02 (cit. on pp. 86, 87, 92).

[53] L. Fu. "Hexagonal Warping Effects in the Surface States of the Topological Insulator Bi_2Te_3". In: *Phys. Rev. Lett.* 103.26 (2009), p. 266801. DOI: 10.1103/PhysRevLett.103.266801 (cit. on p. 19).

[54] L. Fu and C. L. Kane. "Time reversal polarization and a Z_2 adiabatic spin pump". In: *Phys. Rev. B* 74.19 (2006), p. 195312. DOI: 10.1103/physrevb.74.195312 (cit. on p. 17).

[55] L. Fu and C. L. Kane. "Topological insulators with inversion symmetry". In: *Phys. Rev. B* 76.4 (2007), p. 045302. DOI: 10.1103/physrevb.76.045302 (cit. on pp. 15–18).

[56] L. Fu, C. L. Kane, and E. J. Mele. "Topological Insulators in Three Dimensions". In: *Phys. Rev. Lett.* 98.10 (2007), p. 106803. DOI: 10.1103/physrevlett.98.106803 (cit. on pp. 16, 18).

[57] R. Fujiwara, T. Shinshi, and E. Kazawa. "Micromagnetization patterning of sputtered NdFeB/Ta multilayered films utilizing laser assisted heating". In: *Sensors Actuat. A-Phys.* 220 (2014), pp. 298–304. DOI: `10.1016/j.sna.2014.10.011` (cit. on p. 1).

[58] T. Fukui, T. Fujiwara, and Y. Hatsugai. "Topological Meaning of Z_2 Numbers in Time Reversal Invariant Systems". In: *J. Phys. Soc. Jpn.* 77.12 (2008), p. 123705. DOI: `10.1143/jpsj.77.123705` (cit. on p. 17).

[59] T. Fukui and Y. Hatsugai. "Quantum Spin Hall Effect in Three Dimensional Materials: Lattice Computation of Z_2 Topological Invariants and Its Application to Bi and Sb". In: *J. Phys. Soc. Jpn.* 76.5 (2007), p. 053702. DOI: `10.1143/jpsj.76.053702` (cit. on p. 17).

[60] K. Giesen, F. Hage, F. J. Himpsel, H. J. Riess, and W. Steinmann. "Two-photon photoemission via image-potential states". In: *Phys. Rev. Lett.* 55.3 (1985), p. 300. DOI: `10.1103/PhysRevLett.55.300` (cit. on p. 26).

[61] C. Gros. *Thermodynamik & Statistische Mechanik - Theoretische Physik V, Chapter 13: Ideal Fermi gas.* 2017
https://itp.uni-frankfurt.de/~gros/Vorlesungen/TD/13_Ideal_Fermi_gas.pdf
(cit. on p. 94).

[62] F. D. M. Haldane. "Model for a Quantum Hall Effect without Landau Levels: Condensed-Matter Realization of the "Parity Anomaly"". In: *Phys. Rev. Lett.* 61.18 (1988), pp. 2015–2018. DOI: `10.1103/physrevlett.61.2015` (cit. on pp. 14–16).

[63] B. I. Halperin. "Quantized Hall conductance, current-carrying edge states, and the existence of extended states in a two-dimensional disordered potential". In: *Phys. Rev. B* 25.4 (1982), pp. 2185–2190. DOI: `10.1103/physrevb.25.2185` (cit. on p. 17).

[64] M. Z. Hasan and C. L. Kane. "*Colloquium* : Topological insulators". In: *Rev. Mod. Phys.* 82.4 (2010), p. 3045. DOI: `10.1103/RevModPhys.82.3045` (cit. on pp. 2, 7, 15, 18, 43, 44, 67).

[65] M. Z. Hasan and J. E. Moore. "Three-Dimensional Topological Insulators". In: *Annu. Rev. Conden. Ma. P.* 2.1 (2011), pp. 55–78. DOI: `10.1146/annurev-conmatphys-062910-140432` (cit. on p. 15).

[66] Y. Hatsugai. "Chern number and edge states in the integer quantum Hall effect". In: *Phys. Rev. Lett.* 71.22 (1993), pp. 3697–3700. DOI: `10.1103/physrevlett.71.3697` (cit. on p. 17).

[67] M. Hayashi, L. Thomas, R. Moriya, C. Rettner, and S. S. P. Parkin. "Current-Controlled Magnetic Domain-Wall Nanowire Shift Register". In: *Science* 320.5873 (2008), pp. 209–211. DOI: `10.1126/science.1154587` (cit. on p. 1).

[68] I. V. Hertel and C.-P. Schulz. *Atome, Moleküle und optische Physik 1 - Atomphysik und Grundlagen der Spektroskopie.* Springer, 2008 (cit. on p. 8).

[69] H. Hertz. "Über einen Einfluss des ultravioletten Lichtes auf die electrische Ent-ladung". In: *Ann. Phys.* 267.8 (1887), pp. 983–1000 (cit. on p. 21).

[70] G. Hilgers, M. Potthoff, N. Müller, U. Heinzmann, L. Haunert, J. Braun, and G. Borstel. "Necessity of self-energy corrections in LEED theory for Xe(111): Comparison between theoretical and experimental spin-polarized LEED data". In: *Phys. Rev. B* 52.20 (1995), pp. 14859–14867. DOI: 10.1103/PhysRevB.52.14859 (cit. on p. 42).

[71] J. Horák, L. Tichý, and P. Lošťák. "Electrical conductivity of BiTeI crystals". In: *Phys. Status Solidi A* 63.2 (1981), pp. 407–416. DOI: 10.1002/pssa.2210630205 (cit. on pp. 68, 84, 93, 97).

[72] P. Hosur. "Circular photogalvanic effect on topological insulator surfaces: Berry-curvature-dependent response". In: *Phys. Rev. B* 83.3 (2011), p. 035309. DOI: 10.1103/PhysRevB.83.035309 (cit. on p. 48).

[73] D. Hsieh, D. Qian, L. Wray, Y. Xia, Y. S. Hor, R. J. Cava, and M. Z. Hasan. "A topological Dirac insulator in a quantum spin Hall phase". In: *Nature* 452.7190 (2008), pp. 970–974 (cit. on pp. 16, 19).

[74] D. Hsieh, Y. Xia, D. Qian, L. Wray, J. H. Dil, F. Meier, J. Osterwalder, L. Patthey, J. G. Checkelsky, N. P. Ong, A. V. Fedorov, H. Lin, A. Bansil, D. Grauer, Y. S. Hor, R. J. Cava, and M. Z. Hasan. "A tunable topological insulator in the spin helical Dirac transport regime". In: *Nature* 460.7259 (2009), pp. 1101–1105 (cit. on pp. 3, 16, 19, 45).

[75] D. Hsieh, Y. Xia, L. Wray, D. Qian, A. Pal, J. H. Dil, J. Osterwalder, F. Meier, G. Bihlmayer, C. L. Kane, Y. S. Hor, R. J. Cava, and M. Z. Hasan. "Observation of Unconventional Quantum Spin Textures in Topological Insulators". In: *Science* 323.5916 (2009), pp. 919–922. DOI: 10.1126/science.1167733 (cit. on pp. 19, 45).

[76] H. Ibach and H. Lüth. *Festkörperphysik*. Siebte Edition. Springer - Verlag, 2009 (cit. on pp. 11, 92, 94).

[77] Y. Ishida, H. Kanto, A. Kikkawa, Y. Taguchi, Y. Ito, Y. Ota, K. Okazaki, W. Malaeb, M. Mulazzi, M. Okawa, S. Watanabe, C.-T. Chen, M. Kim, C. Bell, Y. Kozuka, H. Y. Hwang, Y. Tokura, and S. Shin. "Common Origin of the Circular-Dichroism Pattern in Angle-Resolved Photoemission Spectroscopy of $SrTiO_3$ and $Cu_xBi_2Se_3$". In: *Phys. Rev. Lett.* 107.7 (2011), p. 077601. DOI: 10.1103/PhysRevLett.107.077601 (cit. on p. 50).

[78] K. Ishizaka, M. S. Bahramy, H. Murakawa, M. Sakano, T. Shimojima, T. Sonobe, K. Koizumi, S. Shin, H. Miyahara, A. Kimura, K. Miyamoto, T. Okuda, H. Namatame, M. Taniguchi, R. Arita, N. Nagaosa, K. Kobayashi, Y. Murakami, R. Kumai, Y. Kaneko, Y. Onose, and Y. Tokura. "Giant Rashba-type spin splitting in bulk BiTeI". In: *Nat. Mater.* 10.7 (2011), pp. 521–526. DOI: 10.1038/nmat3051 (cit. on pp. 2, 3, 67, 68, 70, 72, 73, 77, 84, 99, 108).

[79] C. Jozwiak, C.-H. Park, K. Gotlieb, C. Hwang, D.-H. Lee, S. G. Louie, J. D. Denlinger, C. R. Rotundu, R. J. Birgeneau, Z. Hussain, and A. Lanzara. "Photoelectron spin-flipping and texture manipulation in a topological insulator". In: *Nat. Phys.* 9 (2013), p. 293. DOI: 10.1038/nphys2572 (cit. on pp. 19, 45, 50).

[80] A. Junck, G. Refael, and F. von Oppen. "Photocurrent response of topological insulator surface states". In: *Phys. Rev. B* 88.7 (2013), p. 075144. DOI: 10.1103/PhysRevB.88.075144 (cit. on pp. 3, 49).

[81] C. L. Kane and E. J. Mele. "Z_2 Topological Order and the Quantum Spin Hall Effect". In: *Phys. Rev. Lett.* 95.14 (2005), p. 146802. DOI: 10.1103/PhysRevLett.95.146802 (cit. on pp. 16, 17).

[82] C. L. Kane and E. J. Mele. "Quantum Spin Hall Effect in Graphene". In: *Phys. Rev. Lett.* 95.22 (2005), p. 226801. DOI: 10.1103/physrevlett.95.226801 (cit. on pp. 16, 18).

[83] C. Kastl, C. Karnetzky, H. Karl, and A. W. Holleitner. "Ultrafast helicity control of surface currents in topological insulators with near-unity fidelity". In: *Nat. Commun.* 6.1 (2015), p. 6617. DOI: 10.1038/ncomms7617 (cit. on pp. 3, 4, 43, 49, 59–61, 64).

[84] M. Kepenekian, R. Robles, C. Katan, D. Sapori, L. Pedesseau, and J. Even. "Rashba and Dresselhaus Effects in Hybrid Organic–Inorganic Perovskites: From Basics to Devices". In: *ACS Nano* 9.12 (2015), pp. 11557–11567. DOI: 10.1021/acsnano.5b04409 (cit. on p. 13).

[85] A. S. Ketterl. "Two-photon Photoemission on Topological Insulators". MA thesis. FU Berlin, 2014 (cit. on p. 22).

[86] P. D. C. King, R. C. Hatch, M. Bianchi, R. Ovsyannikov, C. Lupulescu, G. Landolt, B. Slomski, J. H. Dil, D. Guan, J. L. Mi, E. D. L. Rienks, J. Fink, A. Lindblad, S. Svensson, S. Bao, G. Balakrishnan, B. B. Iversen, J. Osterwalder, W. Eberhardt, F. Baumberger, and P. Hofmann. "Large Tunable Rashba Spin Splitting of a Two-Dimensional Electron Gas in Bi_2Se_3". In: *Phys. Rev. Lett.* 107.9 (2011), p. 096802. DOI: 10.1103/PhysRevLett.107.096802 (cit. on p. 50).

[87] P. S. Kirchmann. "Ultrafast Electron Dynamics in Low-Dimensional Materials". PhD thesis. FU Berlin, 2008 (cit. on p. 84).

[88] A. Kitaev. "Periodic table for topological insulators and superconductors". In: *AIP Conf. Proc.* Ed. by V. Lebedev and M. Feigelman. Vol. 1134. 2009, pp. 22–30 (cit. on p. 14).

[89] C. Kittel. *Introduction to Solid State Physics*. Ed. by S. Johnson. Eigth Edition. John Wiley & Sons, Inc, 2005 (cit. on p. 11).

[90] K. v. Klitzing, G. Dorda, and M. Pepper. "New Method for High-Accuracy Determination of the Fine-Structure Constant Based on Quantized Hall Resistance". In: *Phys. Rev. Lett.* 45.6 (1980), pp. 494–497. DOI: 10.1103/physrevlett.45.494 (cit. on p. 15).

[91]   K. v. Klitzing. "Developments in the quantum Hall effect". In: *Philos. T. Roy. Soc. A* 363.1834 (2005), pp. 2203–2219. DOI: 10.1098/rsta.2005.1640 (cit. on p. 15).

[92]   M. König, S. Wiedmann, C. Brüne, A. Roth, H. Buhmann, L. W. Molenkamp, X.-L. Qi, and S.-C. Zhang. "Quantum Spin Hall Insulator State in HgTe Quantum Wells". In: *Science* 318.5851 (2007), pp. 766–770. DOI: 10.1126/science.1148047 (cit. on p. 16).

[93]   J. Koomey. *Our latest on energy efficiency of computing over time, now out in Electronic Design.* Blog entry, https://www.koomey.com/post/153838038643. 2016 (cit. on p. 1).

[94]   J. Koomey, S. Berard, M. Sanchez, and H. Wong. "Implications of Historical Trends in the Electrical Efficiency of Computing". In: *IEEE Ann. Hist. Comput.* 33.3 (2011), pp. 46–54. DOI: 10.1109/mahc.2010.28 (cit. on p. 1).

[95]   J. Kopprasch. "Untersuchung der ultraschnellen Elektronendynamik an Germanium- und Kupferoberflächen mittels zeitaufgelöster Photoelektronenspektroskopie". PhD thesis. FU Berlin, 2013 (cit. on p. 33).

[96]   O. Koroleva, A. Mazhukin, V. Mazhukin, and P. Breslavskiy. "Approximation of Fermi-Dirac integrals of different orders used to determine the thermal properties of metals and semiconductors". In: *Mathematica Montisnigri* 35 (2016), pp. 37–53 (cit. on p. 94).

[97]   Y. M. Koroteev, G. Bihlmayer, J. E. Gayone, E. V. Chulkov, S. Blügel, P. M. Echenique, and P. Hofmann. "Strong Spin-Orbit Splitting on Bi Surfaces". In: *Phys. Rev. Lett.* 93.4 (2004), p. 046403. DOI: 10.1103/physrevlett.93.046403 (cit. on p. 67).

[98]   V. A. Kulbachinskii, V. G. Kytin, Z. V. Lavrukhina, A. N. Kuznetsov, and A. V. Shevelkov. "Galvanomagnetic and thermoelectric properties of BiTeBr and BiTeI single crystals and their electronic structure". In: *Semiconductors* 44.12 (2010), pp. 1548–1553. DOI: 10.1134/s1063782610120031 (cit. on pp. 67, 68, 84, 97).

[99]   T. Kunze. "Charakterisierung und Anwendung eines Flugzeitspektrometers". Diploma thesis. 2009 (cit. on pp. 31, 33).

[100] T. Kunze. "Impulsabhängige, ultraschnelle Elektronendynamik an gestuften Oberflächen und topologischen Isolatoren untersucht mit winkelauflösender Flugzeitspektroskopie". PhD thesis. 2014 (cit. on pp. 24, 30, 34, 39, 40, 52, 86).

[101] K. Kuroda, J. Reimann, J. Güdde, and U. Höfer. "Generation of Transient Photocurrents in the Topological Surface State of Sb_2Te_3 by Direct Optical Excitation with Midinfrared Pulses". In: *Phys. Rev. Lett.* 116.7 (2016), p. 076801. DOI: 10.1103/PhysRevLett.116.076801 (cit. on p. 55).

[102] K. Kuroda, J. Reimann, K. A. Kokh, O. E. Tereshchenko, A. Kimura, J. Güdde, and U. Höfer. "Ultrafast energy- and momentum-resolved surface Dirac photocurrents in the topological insulator Sb_2Te_3". In: *Phys. Rev. B* 95.8 (2017), p. 081103. DOI: 10.1103/PhysRevB.95.081103 (cit. on p. 55).

[103] D. Kutnyakhov, S. Chernov, K. Medjanik, R. Wallauer, C. Tusche, M. Ellguth, S. A. Nepijko, M. Krivenkov, J. Braun, S. Borek, J. Minár, H. Ebert, H. J. Elmers, and G. Schönhense. "Spin texture of time-reversal symmetry invariant surface states on W(110)". In: *Sci. Rep.-UK* 6.1 (2016), p. 29394. DOI: 10.1038/srep29394 (cit. on p. 3).

[104] G. Landolt, S. V. Eremeev, Y. M. Koroteev, B. Slomski, S. Muff, T. Neupert, M. Kobayashi, V. N. Strocov, T. Schmitt, Z. S. Aliev, M. B. Babanly, I. R. Amiraslanov, E. V. Chulkov, J. Osterwalder, and J. H. Dil. "Disentanglement of Surface and Bulk Rashba Spin Splittings in Noncentrosymmetric BiTeI". In: *Phys. Rev. Lett.* 109.11 (2012), p. 116403. DOI: 10.1103/physrevlett.109.116403 (cit. on p. 68).

[105] S. LaShell, B. A. McDougall, and E. Jensen. "Spin Splitting of an Au(111) Surface State Band Observed with Angle Resolved Photoelectron Spectroscopy". In: *Phys. Rev. Lett.* 77.16 (1996), pp. 3419–3422. DOI: 10.1103/physrevlett.77.3419 (cit. on pp. 2, 67, 68).

[106] R. B. Laughlin. "Quantized Hall conductivity in two dimensions". In: *Phys. Rev. B* 23.10 (1981), pp. 5632–5633. DOI: 10.1103/physrevb.23.5632 (cit. on p. 15).

[107] D. Lawrenz. "Two-photon photoemission of topological insulators, Sb_2Te_2S and $BiSbSTe_2$". MA thesis. 2013 (cit. on p. 52).

[108] J. S. Lee, G. A. H. Schober, M. S. Bahramy, H. Murakawa, Y. Onose, R. Arita, N. Nagaosa, and Y. Tokura. "Optical Response of Relativistic Electrons in the Polar BiTeI Semiconductor". In: *Phys. Rev. Lett.* 107.11 (2011), p. 117401. DOI: 10.1103/physrevlett.107.117401 (cit. on pp. 68, 72).

[109] M. Lisowski, P. Loukakos, U. Bovensiepen, J. Staehler, C. Gahl, and M. Wolf. "Ultra-fast dynamics of electron thermalization, cooling and transport effects in Ru(001)". In: *Appl. Phys. A-Mater.* 78.2 (2004), pp. 165–176. DOI: 10.1007/s00339-003-2301-7 (cit. on pp. 86, 87, 92).

[110] G. Malmström and J. Rundgren. "A program for calculation of the reflection and transmission of electrons through a surface potential barrier". In: *Comput. Phys. Commun.* 19.2 (1980), pp. 263–270. DOI: 10.1016/0010-4655(80)90053-3 (cit. on p. 41).

[111] J. Mauchain, Y. Ohtsubo, M. Hajlaoui, E. Papalazarou, M. Marsi, A. Taleb-Ibrahimi, J. Faure, K. A. Kokh, O. E. Tereshchenko, S. V. Eremeev, E. V. Chulkov, and L. Perfetti. "Circular Dichroism and Superdiffusive Transport at the Surface of BiTeI". In: *Phys. Rev. Lett.* 111.12 (2013), p. 126603. DOI: 10.1103/physrevlett.111.126603 (cit. on pp. 67, 77, 78, 80–82, 107, 110).

[112] J. W. McIver, D. Hsieh, H. Steinberg, P. Jarillo-Herrero, and N. Gedik. "Control over topological insulator photocurrents with light polarization". In: *Nat. Nanotechnol.* 7.2 (2011), pp. 96–100. DOI: 10.1038/nnano.2011.214 (cit. on pp. 3, 4, 43, 48, 50, 55, 58–60, 64).

[113] M. Michiardi, I. Aguilera, M. Bianchi, V. E. de Carvalho, L. O. Ladeira, N. G. Teixeira, E. A. Soares, C. Friedrich, S. Blügel, and P. Hofmann. "Bulk band structure of Bi_2Te_3". In: *Phys. Rev. B* 90.7 (2014), p. 075105. DOI: 10.1103/physrevb.90.075105 (cit. on p. 47).

[114] K. Miyamoto, A. Kimura, K. Kuroda, T. Okuda, K. Shimada, H. Namatame, M. Taniguchi, and M. Donath. "Spin-Polarized Dirac-Cone-Like Surface State with d Character at W(110)". In: *Phys. Rev. Lett.* 108.6 (2012), p. 066808. DOI: 10.1103/physrevlett.108.066808 (cit. on p. 3).

[115] K. Miyamoto, A. Kimura, T. Okuda, K. Shimada, H. Iwasawa, H. Hayashi, H. Namatame, M. Taniguchi, and M. Donath. "Massless or heavy due to two-fold symmetry: Surface-state electrons at W(110)". In: *Phys. Rev. B* 86.16 (2012), p. 161411. DOI: 10.1103/physrevb.86.161411 (cit. on p. 3).

[116] G. E. Moore. "Cramming more components onto integrated circuits". In: *Electronics* 8 (1965), p. 4 (cit. on p. 1).

[117] J. E. Moore and L. Balents. "Topological invariants of time-reversal-invariant band structures". In: *Phys. Rev. B* 75.12 (2007), p. 121306. DOI: 10.1103/PhysRevB.75.121306 (cit. on pp. 17, 18).

[118] J. E. Moore. "The next generation". In: *Nat. Phys.* 5 (2009), pp. 378–380 (cit. on pp. 19, 44).

[119] A. Nakamura, T. Shimojima, M. Nakano, Y. Iwasa, and K. Ishizaka. "Electron and lattice dynamics of transition metal thin films observed by ultrafast electron diffraction and transient optical measurements". In: *Struct. Dynam.-US* 3.6 (2016), p. 064501. DOI: 10.1063/1.4971210 (cit. on pp. 86, 92).

[120] National Academies of Sciences, Engineering, and Medicine. *Quantum Computing: Progress and Prospects*. Ed. by E. Grumbling and M. Horowitz. The National Academies Press, 2019. DOI: 10.17226/25196 (cit. on p. 1).

[121] I. A. Nechaev and E. V. Chulkov. "Width of the quasiparticle spectral function in a two-dimensional electron gas with spin-orbit interaction". In: *Phys. Solid State* 51.9 (2009), pp. 1772–1777. DOI: 10.1134/s1063783409090029 (cit. on pp. 79, 98).

[122] I. A. Nechaev, P. M. Echenique, and E. V. Chulkov. "Inelastic decay rate of quasiparticles in a two-dimensional spin-orbit coupled electron system". In: *Phys. Rev. B* 81.19 (2010), p. 195112. DOI: 10.1103/physrevb.81.195112 (cit. on p. 98).

[123] I. A. Nechaev, M. F. Jensen, E. D. L. Rienks, V. M. Silkin, P. M. Echenique, E. V. Chulkov, and P. Hofmann. "Hole dynamics in a two-dimensional spin-orbit coupled electron system: Theoretical and experimental study of the Au(111) surface state". In: *Phys. Rev. B* 80.11 (2009), p. 113402. DOI: 10.1103/physrevb.80.113402 (cit. on p. 79).

[124] I. A. Nechaev, V. M. Silkin, and E. V. Chulkov. "Features of quasiparticle decay in 2D electronic systems with spin–orbit interaction". In: *J. Exp. Theor. Phys.* 112.1 (2011), pp. 134–139. DOI: 10.1134/s1063776110051188 (cit. on p. 98).

[125] D. Niesner, T. Fauster, S. V. Eremeev, T. V. Menshchikova, Y. M. Koroteev, A. P. Protogenov, E. V. Chulkov, O. E. Tereshchenko, K. A. Kokh, O. Alekperov, A. Nadjafov, and N. Mamedov. "Unoccupied topological states on bismuth chalcogenides". In: *Phys. Rev. B* 86.20 (2012), p. 205403. DOI: 10.1103/PhysRevB.86.205403 (cit. on pp. 3, 43, 45, 50, 52).

[126] D. Niesner, S. Otto, T. Fauster, E. Chulkov, S. Eremeev, O. Tereshchenko, and K. Kokh. "Electron dynamics of unoccupied states in topological insulators". In: *J. Electron Spectrosc.* 195 (2014), pp. 258–262. DOI: 10.1016/j.elspec.2014.03.013 (cit. on pp. 3, 43, 45, 60, 61).

[127] D. Niesner, S. Otto, V. Hermann, T. Fauster, T. V. Menshchikova, S. V. Eremeev, Z. S. Aliev, I. R. Amiraslanov, M. B. Babanly, P. M. Echenique, and E. V. Chulkov. "Bulk and surface electron dynamics in a p-type topological insulator $SnSb_2Te_4$". In: *Phys. Rev. B* 89.8 (2014), p. 081404. DOI: 10.1103/PhysRevB.89.081404 (cit. on pp. 43, 60).

[128] J. Nitta, T. Akazaki, H. Takayanagi, and T. Enoki. "Gate Control of Spin-Orbit Interaction in an Inverted $In_{0.53}Ga_{0.47}As/In_{0.52}Al_{0.48}As$ Heterostructure". In: *Phys. Rev. Lett.* 78.7 (1997), pp. 1335–1338. DOI: 10.1103/physrevlett.78.1335 (cit. on p. 14).

[129] A. Nuber, J. Braun, F. Forster, J. Minár, F. Reinert, and H. Ebert. "Surface versus bulk contributions to the Rashba splitting in surface systems". In: *Phys. Rev. B* 83.16 (2011), p. 165401. DOI: 10.1103/PhysRevB.83.165401 (cit. on p. 41).

[130] N. Ogawa, M. S. Bahramy, Y. Kaneko, and Y. Tokura. "Photocontrol of Dirac electrons in a bulk Rashba semiconductor". In: *Phys. Rev. B* 90.12 (2014), p. 125122. DOI: 10.1103/physrevb.90.125122 (cit. on pp. 2, 67).

[131] N. Ogawa, M. S. Bahramy, H. Murakawa, Y. Kaneko, and Y. Tokura. "Magnetophotocurrent in BiTeI with Rashba spin-split bands". In: *Phys. Rev. B* 88.3 (2013), p. 035130. DOI: 10.1103/physrevb.88.035130 (cit. on p. 67).

[132] P. Olbrich, L. E. Golub, T. Herrmann, S. N. Danilov, H. Plank, V. V. Bel'kov, G. Mussler, C. Weyrich, C. M. Schneider, J. Kampmeier, D. Grützmacher, L. Plucinski, M. Eschbach, and S. D. Ganichev. "Room-Temperature High-Frequency Transport of Dirac Fermions in Epitaxially Grown Sb_2Te_3- and Bi_2Te_3-Based

Topological Insulators". In: *Phys. Rev. Lett.* 113.9 (2014), p. 096601. DOI: `10.1103/PhysRevLett.113.096601` (cit. on pp. 3, 43, 49).

[133] Y. Pan, Q.-Z. Wang, A. L. Yeats, T. Pillsbury, T. C. Flanagan, A. Richardella, H. Zhang, D. D. Awschalom, C.-X. Liu, and N. Samarth. "Helicity dependent photocurrent in electrically gated $(Bi_{1-x}Sb_x)_2Te_3$ thin films". In: *Nat. Commun.* 8 (2017), p. 1037. DOI: `10.1038/s41467-017-00711-4` (cit. on pp. 3, 4, 49, 59, 60).

[134] C.-H. Park and S. G. Louie. "Spin Polarization of Photoelectrons from Topological Insulators". In: *Phys. Rev. Lett.* 109 (9 2012), p. 097601. DOI: `10.1103/PhysRevLett.109.097601` (cit. on p. 50).

[135] S. R. Park, J. Han, C. Kim, Y. Y. Koh, C. Kim, H. Lee, H. J. Choi, J. H. Han, K. D. Lee, N. J. Hur, M. Arita, K. Shimada, H. Namatame, and M. Taniguchi. "Chiral Orbital-Angular Momentum in the Surface States of Bi_2Se_3". In: *Phys. Rev. Lett.* 108.4 (2012), p. 046805. DOI: `10.1103/PhysRevLett.108.046805` (cit. on pp. 19, 50, 52).

[136] J. B. Pendry. *Low Energy Electron Diffraction*. First Edition. Academic Press, 1974 (cit. on p. 42).

[137] L. Perfetti, P. A. Loukakos, M. Lisowski, U. Bovensiepen, H. Eisaki, and M. Wolf. "Ultrafast Electron Relaxation in Superconducting $Bi_2Sr_2CaCu_2O_{8+\delta}$ by Time-Resolved Photoelectron Spectroscopy". In: *Phys. Rev. Lett.* 99.19 (2007), p. 197001. DOI: `10.1103/physrevlett.99.197001` (cit. on p. 93).

[138] L. Petersen and P. Hedegård. "A simple tight-binding model of spin–orbit splitting of sp-derived surface states". In: *Surf. Sci.* 459.1-2 (2000), pp. 49–56. DOI: `10.1016/s0039-6028(00)00441-6` (cit. on pp. 14, 67).

[139] H. Plank, S. N. Danilov, V. V. Bel'kov, V. A. Shalygin, J. Kampmeier, M. Lanius, G. Mussler, D. Grützmacher, and S. D. Ganichev. "Opto-electronic characterization of three dimensional topological insulators". In: *J. Appl. Phys.* 120.16 (2016), p. 165301. DOI: `10.1063/1.4965962` (cit. on pp. 3, 49).

[140] H. Plank, L. E. Golub, S. Bauer, V. V. Bel'kov, T. Herrmann, P. Olbrich, M. Eschbach, L. Plucinski, C. M. Schneider, J. Kampmeier, M. Lanius, G. Mussler, D. Grützmacher, and S. D. Ganichev. "Photon drag effect in $(Bi_{1-x}Sb_x)_2Te_3$ three-dimensional topological insulators". In: *Phys. Rev. B* 93.12 (2016), p. 125434. DOI: `10.1103/PhysRevB.93.125434` (cit. on pp. 3, 49).

[141] H. Plank, J. Pernul, S. Gebert, S. N. Danilov, J. König-Otto, S. Winnerl, M. Lanius, J. Kampmeier, G. Mussler, I. Aguilera, D. Grützmacher, and S. D. Ganichev. "Infrared/terahertz spectra of the photogalvanic effect in (Bi,Sb)Te based three-dimensional topological insulators". In: *Phys. Rev. Mater.* 2.2 (2018), p. 024202. DOI: `10.1103/PhysRevMaterials.2.024202` (cit. on pp. 3, 49).

[142] M. Polverigiani. "Electron Dynamics in the Rashba material BiTeI". MA thesis. FU Berlin, 2017 (cit. on p. 67).

[143]   X.-L. Qi, T. L. Hughes, and S.-C. Zhang. "Topological field theory of time-reversal invariant insulators". In: *Phys. Rev. B* 78.19 (2008), p. 195424. DOI: 10.1103/physrevb.78.195424 (cit. on pp. 14, 17).

[144]   X.-L. Qi and S.-C. Zhang. "The quantum spin Hall effect and topological insulators". In: *Phys. Today* 63.1 (2010), pp. 33–38. DOI: 10.1063/1.3293411 (cit. on p. 15).

[145]   J. J. Quinn and R. A. Ferrell. "Electron Self-Energy Approach to Correlation in a Degenerate Electron Gas". In: *Phys. Rev.* 112.3 (1958), pp. 812–827. DOI: 10.1103/physrev.112.812 (cit. on p. 84).

[146]   I. Radu, K. Vahaplar, C. Stamm, T. Kachel, N. Pontius, H. A. Dürr, T. A. Ostler, J. Barker, R. F. L. Evans, R. W. Chantrell, A. Tsukamoto, A. Itoh, A. Kirilyuk, T. Rasing, and A. V. Kimel. "Transient ferromagnetic-like state mediating ultrafast reversal of antiferromagnetically coupled spins". In: *Nature* 472.7342 (2011), pp. 205–208. DOI: 10.1038/nature09901 (cit. on p. 1).

[147]   E. I. Rashba. "Combined Resonance in Semiconductors". In: *Sov. Phys. Usp.* 7.6 (1965), pp. 823–836. DOI: 10.1070/pu1965v007n06abeh003687 (cit. on p. 2).

[148]   E. I. Rashba and V. I. Sheka. *Landau Level Spectroscopy*. Ed. by G. Landwehr and E. I. Rashba. Elsevier, 1991. Chap. 4, pp. 131–206 (cit. on p. 2).

[149]   E. I. Rashba and V. I. Sheka. "Symmetry of Energy Bands in Crystals of Wurtzite Type II. Symmetry of Bands with Spin-Orbit Interaction Included". In: *Fiz. Tverd. Tela: Collected Papers* 2 (1959). English translation published as the supplementary material to the article by Bihlmayer et al 2015 New. J. Phys. 17 050202 [18], pp. 162–76 (cit. on p. 13).

[150]   E. Rashba. "Properties of semiconductors with an extremum loop. 1. Cyclotron and combinational resonance in a magnetic field perpendicular to the plane of the loop". In: *Sov. Phys. Solid State* 2 (1960), p. 1109 (cit. on pp. 2, 68).

[151]   J. Reimann, J. Güdde, K. Kuroda, E. V. Chulkov, and U. Höfer. "Spectroscopy and dynamics of unoccupied electronic states of the topological insulators Sb_2Te_3 and Sb_2Te_2S". In: *Phys. Rev. B* 90.8 (2014), p. 081106. DOI: 10.1103/PhysRevB.90.081106 (cit. on pp. 52, 60).

[152]   F. Reinert, G. Nicolay, S. Schmidt, D. Ehm, and S. Hüfner. "Direct measurements of the L-gap surface states on the (111) face of noble metals by photoelectron spectroscopy". In: *Phys. Rev. B* 63.11 (2001), p. 115415. DOI: 10.1103/physrevb.63.115415 (cit. on p. 67).

[153]   H.-S. Rhie, H. A. Dürr, and W. Eberhardt. "Femtosecond Electron and Spin Dynamics in Ni/W(110) Films". In: *Phys. Rev. Lett.* 90.24 (2003), p. 247201. DOI: 10.1103/physrevlett.90.247201 (cit. on pp. 86, 92).

[154]   C. W. Rischau, A. Ubaldini, E. Giannini, and C. J. van der Beek. "Charge puddles in a completely compensated topological insulator". In: *New J. Phys.* 18.7 (2016), p. 073024. DOI: 10.1088/1367-2630/18/7/073024 (cit. on p. 49).

[155] R. Roy. "Z_2 classification of quantum spin Hall systems: An approach using time-reversal invariance". In: *Phys. Rev. B* 79.19 (2009), p. 195321. DOI: `10.1103/physrevb.79.195321` (cit. on p. 17).

[156] J. H. Ryoo and C.-H. Park. "Spin-conserving and reversing photoemission from the surface states of Bi_2Se_3 and Au (111)". In: *Phys. Rev. B* 93.8 (2016), p. 085419. DOI: `10.1103/PhysRevB.93.085419` (cit. on pp. 19, 50).

[157] M. Sakano, J. Miyawaki, A. Chainani, Y. Takata, T. Sonobe, T. Shimojima, M. Oura, S. Shin, M. S. Bahramy, R. Arita, N. Nagaosa, H. Murakawa, Y. Kaneko, Y. Tokura, and K. Ishizaka. "Three-dimensional bulk band dispersion in polar BiTeI with giant Rashba-type spin splitting". In: *Phys. Rev. B* 86.8 (2012), p. 085204. DOI: `10.1103/physrevb.86.085204` (cit. on p. 68).

[158] J. Sánchez-Barriga, E. Golias, A. Varykhalov, J. Braun, L. V. Yashina, R. Schumann, J. Minár, H. Ebert, O. Kornilov, and O. Rader. "Ultrafast spin-polarization control of Dirac fermions in topological insulators". In: *Phys. Rev. B* 93.15 (2016), p. 155426. DOI: `10.1103/PhysRevB.93.155426` (cit. on pp. 50, 64).

[159] J. Sánchez-Barriga, A. Varykhalov, J. Braun, S.-Y. Xu, N. Alidoust, O. Kornilov, J. Minár, K. Hummer, G. Springholz, G. Bauer, R. Schumann, L. V. Yashina, H. Ebert, M. Z. Hasan, and O. Rader. "Photoemission of Bi_2Se_3 with Circularly Polarized Light: Probe of Spin Polarization or Means for Spin Manipulation?" In: *Phys. Rev. X* 4.1 (2014), p. 011046. DOI: `10.1103/PhysRevX.4.011046` (cit. on pp. 19, 45, 50, 52).

[160] J. Sánchez-Barriga, G. Bihlmayer, D. Wortmann, D. Marchenko, O. Rader, and A. Varykhalov. "Effect of structural modulation and thickness of a graphene overlayer on the binding energy of the Rashba-type surface state of Ir(111)". In: *New J. Phys.* 15.11 (2013), p. 115009. DOI: `10.1088/1367-2630/15/11/115009` (cit. on p. 14).

[161] M. Scheuch, T. Kampfrath, M. Wolf, K. von Volkmann, C. Frischkorn, and L. Perfetti. "Temperature dependence of ultrafast phonon dynamics in graphite". In: *Appl. Phys. Lett.* 99.21 (2011), p. 211908. DOI: `10.1063/1.3663867` (cit. on p. 93).

[162] A. P. Schnyder, S. Ryu, A. Furusaki, and A. W. W. Ludwig. "Classification of topological insulators and superconductors in three spatial dimensions". In: *Phys. Rev. B* 78.19 (2008), p. 195125. DOI: `10.1103/physrevb.78.195125` (cit. on p. 14).

[163] M. R. Scholz. "Spin Polarization, Circular Dichroism, and Robustness of Topological Surface States: A Photoemission Study". PhD thesis. 2012 (cit. on p. 15).

[164] M. R. Scholz, J. Sánchez-Barriga, D. Marchenko, A. Varykhalov, A. Volykhov, L. V. Yashina, and O. Rader. "Tolerance of Topological Surface States towards Magnetic Moments: Fe on Bi_2Se_3". In: *Phys. Rev. Lett.* 108.25 (2012), p. 256810. DOI: `10.1103/physrevlett.108.256810` (cit. on p. 45).

[165]   M. Schultz, F. Heinrichs, U. Merkt, T. Colin, T. Skauli, and S. Løvold. "Rashba spin splitting in a gated HgTe quantum well". In: *Semicond. Sci. Tech.* 11.8 (1996), pp. 1168–1172. DOI: `10.1088/0268-1242/11/8/009` (cit. on p. 14).

[166]   A. M. Shikin, A. A. Rybkina, A. S. Korshunov, Y. B. Kudasov, N. V. Frolova, A. G. Rybkin, D. Marchenko, J. Sánchez-Barriga, A. Varykhalov, and O. Rader. "Induced Rashba splitting of electronic states in monolayers of Au, Cu on a W(110) substrate". In: *New J. Phys.* 15.9 (2013), p. 095005. DOI: `10.1088/1367-2630/15/9/095005` (cit. on p. 14).

[167]   J. A. Sobota, S.-L. Yang, A. F. Kemper, J. J. Lee, F. T. Schmitt, W. Li, R. G. Moore, J. G. Analytis, I. R. Fisher, P. S. Kirchmann, T. P. Devereaux, and Z.-X. Shen. "Direct Optical Coupling to an Unoccupied Dirac Surface State in the Topological Insulator Bi_2Se_3". In: *Phys. Rev. Lett.* 111.13 (2013), p. 136802. DOI: `10.1103/PhysRevLett.111.136802` (cit. on pp. 19, 45, 47).

[168]   J. Sobota, S.-L. Yang, D. Leuenberger, A. Kemper, J. Analytis, I. Fisher, P. Kirchmann, T. Devereaux, and Z.-X. Shen. "Ultrafast Electron Dynamics in the Topological Insulator Bi_2Se_3 Studied by Time-Resolved Photoemission Spectroscopy". In: *J. Electron Spectrosc.* 195 (2014), pp. 249–257. DOI: `10.1016/j.elspec.2014.01.005` (cit. on p. 19).

[169]   H. Soifer, A. Gauthier, A. Kemper, C. Rotundu, S.-L. Yang, H. Xiong, D. Lu, M. Hashimoto, P. Kirchmann, J. Sobota, and Z.-X. Shen. "Band-Resolved Imaging of Photocurrent in a Topological Insulator". In: *Phys. Rev. Lett.* 122.16 (2019), p. 167401. DOI: `10.1103/physrevlett.122.167401` (cit. on p. 55).

[170]   S. Souma, K. Kosaka, T. Sato, M. Komatsu, A. Takayama, T. Takahashi, M. Kriener, K. Segawa, and Y. Ando. "Direct Measurement of the Out-of-Plane Spin Texture in the Dirac-Cone Surface State of a Topological Insulator". In: *Phys. Rev. Lett.* 106.21 (2011), p. 216803. DOI: `10.1103/PhysRevLett.106.216803` (cit. on p. 50).

[171]   D. Stein, K. v. Klitzing, and G. Weimann. "Electron Spin Resonance on GaAs-$Al_xGa_{1-x}As$ Heterostructures". In: *Phys. Rev. Lett.* 51.2 (1983), pp. 130–133. DOI: `10.1103/physrevlett.51.130` (cit. on pp. 2, 13).

[172]   H. L. Stormer, Z. Schlesinger, A. Chang, D. C. Tsui, A. C. Gossard, and W. Wiegmann. "Energy Structure and Quantized Hall Effect of Two-Dimensional Holes". In: *Phys. Rev. Lett.* 51.2 (1983), pp. 126–129. DOI: `10.1103/physrevlett.51.126` (cit. on pp. 2, 13).

[173]   M. Studer, G. Salis, K. Ensslin, D. C. Driscoll, and A. C. Gossard. "Gate-Controlled Spin-Orbit Interaction in a Parabolic GaAs/AlGaAs Quantum Well". In: *Phys. Rev. Lett.* 103.2 (2009), p. 027201. DOI: `10.1103/physrevlett.103.027201` (cit. on pp. 7, 67).

[174]   *Surface Concept Delayline Detectors Catalogue 2011*. Surface Concept GmbH, Mainz. 2011 (cit. on pp. 31, 32).

[175] S. M. Sze. *Physics of Semiconductor Devices*. Ed. by M. Hill. Second Edition. John John Wiley & Sons, Inc, 1981 (cit. on p. 102).

[176] D. J. Thouless, M. Kohmoto, M. P. Nightingale, and M. den Nijs. "Quantized Hall Conductance in a Two-Dimensional Periodic Potential". In: *Phys. Rev. Lett.* 49.6 (1982), p. 405. DOI: 10.1103/PhysRevLett.49.405 (cit. on pp. 14, 15).

[177] T. Valla, Z.-H. Pan, D. Gardner, Y. S. Lee, and S. Chu. "Photoemission Spectroscopy of Magnetic and Nonmagnetic Impurities on the Surface of the Bi_2Se_3 Topological Insulator". In: *Phys. Rev. Lett.* 108.11 (2012), p. 117601. DOI: 10.1103/PhysRevLett.108.117601 (cit. on p. 19).

[178] S. H. Vosko, L. Wilk, and M. Nusair. "Accurate spin-dependent electron liquid correlation energies for local spin density calculations: a critical analysis". In: *Can. J. Phys.* 58.8 (1980), pp. 1200–1211. DOI: 10.1139/p80-159 (cit. on p. 41).

[179] W. Wallauer. "Bildpotenzialzustände von sauberen und adsorbatbedeckten Metalloberflächen". PhD thesis. 1995 (cit. on p. 24).

[180] Y. H. Wang, D. Hsieh, D. Pilon, L. Fu, D. R. Gardner, Y. S. Lee, and N. Gedik. "Observation of a Warped Helical Spin Texture in Bi_2Se_3 from Circular Dichroism Angle-Resolved Photoemission Spectroscopy". In: *Phys. Rev. Lett.* 107.20 (2011), p. 207602. DOI: 10.1103/PhysRevLett.107.207602 (cit. on pp. 19, 50).

[181] Y. Wang and N. Gedik. "Circular dichroism in angle-resolved photoemission spectroscopy of topological insulators". In: *Phys. Status Solidi* 7 (2013), p. 64. DOI: 10.1002/pssr.201206458 (cit. on p. 50).

[182] Z. Wang, X.-L. Qi, and S.-C. Zhang. "Equivalent topological invariants of topological insulators". In: *New J. Phys.* 12.6 (2010), p. 065007. DOI: 10.1088/1367-2630/12/6/065007 (cit. on p. 17).

[183] H. Whitney. "Moscow 1935: Topology Moving Toward America". In: *Hassler Whitney Collected Papers*. Birkhäuser Boston, 1992, pp. 1–21. DOI: 10.1007/978-1-4612-2972-8_1 (cit. on p. 15).

[184] S. Wirths, R. Geiger, N. von den Driesch, G. Mussler, T. Stoica, S. Mantl, Z. Ikonic, M. Luysberg, S. Chiussi, J. M. Hartmann, H. Sigg, J. Faist, D. Buca, and D. Grützmacher. "Lasing in direct-bandgap GeSn alloy grown on Si". In: *Nat. Photonics* 9.2 (2015), pp. 88–92. DOI: 10.1038/nphoton.2014.321 (cit. on p. 91).

[185] S. N. P. Wissing, A. B. Schmidt, H. Mirhosseini, J. Henk, C. R. Ast, and M. Donath. "Ambiguity of Experimental Spin Information from States with Mixed Orbital Symmetries". In: *Phys. Rev. Lett.* 113.11 (2014), p. 116402. DOI: 10.1103/PhysRevLett.113.116402 (cit. on p. 50).

[186] L. Wu, J. Yang, M. Chi, S. Wang, P. Wei, W. Zhang, L. Chen, and J. Yang. "Enhanced Thermoelectric Performance in Cu-Intercalated BiTeI by Compensation Weakening Induced Mobility Improvement". In: *Sci. Rep.-UK* 5.1 (2015), p. 14319. DOI: 10.1038/srep14319 (cit. on pp. 92, 93, 97, 102).

[187] Y. Xia, D. Qian, D. Hsieh, L. Wray, A. Pal, H. Lin, A. Bansil, D. Grauer, Y. S. Hor, R. J. Cava, and M. Z. Hasan. "Observation of a large-gap topological-insulator class with a single Dirac cone on the surface". In: *Nat. Phys.* 5.6 (2009), pp. 398–402. DOI: 10.1038/nphys1274 (cit. on p. 45).

[188] Z. Xie, S. He, C. Chen, Y. Feng, H. Yi, A. Liang, L. Zhao, D. Mou, J. He, Y. Peng, X. Liu, Y. Liu, G. Liu, X. Dong, L. Yu, J. Zhang, S. Zhang, Z. Wang, F. Zhang, F. Yang, Q. Peng, X. Wang, C. Chen, Z. Xu, and X. J. Zhou. "Orbital-selective spin texture and its manipulation in a topological insulator". In: *Nat. Commun.* 5 (2014), p. 3382. DOI: 10.1038/ncomms4382 (cit. on pp. 19, 50).

[189] H. Zhang, C.-X. Liu, and S.-C. Zhang. "Spin-Orbital Texture in Topological Insulators". In: *Phys. Rev. Lett.* 111.6 (2013), p. 066801. DOI: 10.1103/PhysRevLett.111.066801 (cit. on pp. 19, 50).

[190] Z.-H. Zhu, C. N. Veenstra, G. Levy, A. Ubaldini, P. Syers, N. P. Butch, J. Paglione, M. W. Haverkort, I. S. Elfimov, and A. Damascelli. "Layer-By-Layer Entangled Spin-Orbital Texture of the Topological Surface State in Bi_2Se_3". In: *Phys. Rev. Lett.* 110.21 (2013), p. 216401. DOI: 10.1103/physrevlett.110.216401 (cit. on p. 52).

[191] W. Zulehner. *Numerische Mathematik.* Springer Basel, 2011 (cit. on pp. 40, 41).

Supervised Theses

[a]   Martin Bastian, 2016
Simulation of Electron Trajectories in a ToF Photoelectron Spectrometer and Application to Topological Surface States

[b]   Marco Polverigiani, 2017
Electron Dynamics in the Rashba material BiTeI

Parts of these theses, that were supervised by the author, contributed to chapters 3 and 5 in this thesis.

List of Publications

[I]   A. S. Ketterl, S. Otto, M. Bastian, B. Andres, C. Gahl, J. Minár, H. Ebert,
J. Braun, O. E. Tereshchenko, K. A. Kokh, Th. Fauster, and M. Weinelt
Origin of spin-polarized photocurrents in the topological surface states of Bi_2Se_3
Phys. Rev. B **98**.15, 155406 (2018)
DOI: 10.1103/PhysRevB.98.155406

[II]   A. S. Ketterl, V. Voroshnnin, M. Polverigiani, B. Andres, C. Gahl,
O. E. Tereshchenko, K. A. Kokh, A. Shikin, and M. Weinelt
Asymmetry of Electron and Hole Dynamics on BiTeI (in preparation)

[III]   A. S. Ketterl, T. Kunze, D. Lawrenz, C. Gahl, and M. Weinelt
Electron Dynamics on Sb_2Te_2S, Measurements and Simulations (in preparation)

Danksagung

First of all, I want to thank my supervisor Martin Weinelt for offering me the opportunity to work on this thesis, for scientific discussion and insight. In addition, I want to thank Beatrice Andres for supervising the BiTeI project and Thomas Kunze for teaching me the fundamentals of 2PPE during my master thesis and introducing me to the experimental study of topological insulators.

I further want to thank my collaborators Sebastian Otto and Vladimir Voroshnin, who not only provided the samples for the measurements on Bi_2Se_3 and BiTeI respectively, but also a lot of help, both in the lab and outside of it. I have to thank Sebastian especially for providing me with vital discussions, evaluation procedures and moral support. Without your help, the Bi_2Se_3 would - at the very least - have taken much longer. Getting any reasonable spectra out of the elusive BiTeI on the other hand, would have been impossible without the experience shared by Vladimir. Additionally, I want to thank you for our discussions over coffee and brownies, they helped a lot, too. I also have to thank Hubert Ebert, Jan Minár and Jürgen Braun for providing the calculations presented in the chapter on Bi_2Se_3. Without the calculations and the helpful discussions, it would have been much harder to understand our experimental data.

Within my own group, I have to thank all my colleagues for supporting me without being formally assigned to my projects. I especially want to thank Kristof Zielke and Daniel Przyrembel for never hesitating to help me, especially with fixing and modifying my UHV chamber, Wibke Bronsch for discussions and support regarding all parts of the setup, and Cornelius Gahl for advice and support with the laser system and spectrometer. But also to the rest of you, thank you for all your support, your kind words and your advice!

Special thanks go to Martin Bastian and Marco Polverigiani for their contributions to this thesis as master students. I highly appreciate your work and I enjoyed working with both of you. I hope, you'll keep me in favorable memory.

I want to thank Kristof, who shared an office with me throughout all the years, once more for his company. I was really lucky to have you as my office mate.

And I want to thank the students and heads of my grad-school, the IMPRS, for their support in many a regard.

One person that is more than just a colleague to me is Kamil Bobowski. I have to thank you not only for the occasional scientific support, but mainly for everything else you did for me. Thank you for being my support, for your patience whenever I prioritized my work, leaving me without energy for our relationship, for putting up with my foul moods when I was stressed, for your encouraging words, for being a reason to actually make use of my holidays. And for sharing so many hobbies while also being fine whenever I decide to spend the little free time I have with other people or activities. Thank you for being as you are.

A very big thank you goes to my parents and my family, for always having my back. You made it possible that I could fully focus on my work without having to worry about anything else. I cannot thank you enough for that.

And finally thank you to my friends, my roleplayers, my dancers and my training partners, especially Andy (also for corrections), Anika, Batch, Chrissi and Steffi, Daniela and James, Eiko, Falk E. with family, Falk K., Fismo, Irena, Erik, Dudi and Flo, Isa, Jan and Claudi, Johanna, Jörg and Anja, JP, Jule and Kenni, Julius, Kathi, Kathi, Katrin, Konrad, Kristin, Larissa, Lina, Luci and Nils, Markus and Celina, Martin, Nils, Olof, Peter, Robin and Sophie, Sas, Sven, Teja. Thanks for getting my mind off my work every once in a while, for listening and encouraging me, for making these years bearable and for your patience.

And a special thank you to all of you who never lost faith in me, for believing in me, for helping me regain my self-esteem and rediscover myself, after I had lost both.

Lebenslauf

Anna Sophia Ketterl

Der Lebenslauf ist in der Online-Version aus Gründen des Datenschutzes nicht enthalten.

Selbstständigkeitserklärung

Hiermit erkläre ich, Anna Sophia Ketterl, diese Dissertation selbstständig und nur unter Verwendung der angegebenen Hilfen und Hilfsmittel angefertigt zu haben. Die Arbeit wurde weder in einem früheren Promotionsverfahren angenommen noch als ungenügend beurteilt. Ich erkläre die Kenntnisnahme der dem Verfahren zugrunde liegenden Promotionsordnung des Fachbereichs Physik der Freien Universität Berlin veröffentlicht in den FU-Mitteilungen 34/2013 vom 02.09.2013.

Berlin, den 16. August 2019

Anna Sophia Ketterl

Acronyms

lcp	left circularly polarized light
rcp	right circularly polarized light
hcp	hexagonally close packed
2PPE	two-photon photoemission
ARPES	angle-resolved photoemission spectroscopy
BBO	β-barium borate
BS	band structure
BZ	Brillouin zone
CB	conduction band
CBM	conduction band minimum
CDAD	circular dirchoism in the angular distribution
DC	Dirac cone
DFT	density functional theory
DLD	Delayline Detector
DOS	density of states
DP	Dirac point
FH	fourth harmonic
FHG	fourth harmonic generation
IQHE	integer Quantum Hall Effect
LEED	low-energy electron diffraction
MCP	multi-channel plate
MOSFET	metal-oxide-semiconductor field-effect transistor
nIR	near-infrared
OPA	optical parametric amplifier
PE	photoelectron
PES	photoemission spectroscopy

QL	quintuple layer
QSH	Quantum Spin Hall
RegA	regenerative amplifier
RSS	Rashba-split surface state
RT	room temperature
SH	second harmonic
SHG	second-harmonic generation
SOC	spin-orbit coupling
SOI	spin-orbit interaction
SOS	spin-orbit splitting
spin-FET	spin field-effect transistor
TH	third harmonic
THG	third-harmonic generation
TI	topological insulator
Ti:Sa	titanium sapphire
TL	trilayer
ToF	time-of-flight
tr-ARPES	time- and angle-resolved photoemission spectroscopy
TRIM	time-reversal invariant momenta
TSS	topological surface state
UHV	ultrahigh vacuum
VB	valence band
VBM	valence band maximum
WAM	Wide-angle mode